IMAGE-BASED HYBRID SCAFFOLD DESIGN FOR MULTIPLE TISSUE REGENERATION APPLICATION IN PERIODONTAL ENGINEERING

By

Chan Ho Park

A dissertation submitted in partial fulfillment
of the requirements for the degree of
Doctor of Philosophy
(Biomedical Engineering)
in The University of Michigan
2010

Doctoral Committee:

Professor William V. Giannobile, Chair
Professor Scott J. Hollister
Professor Peter X. Ma
Professor Shuichi Takayama

DEDICATION

To My Beloved Family:

Chong Oon Park and Kyung Sun Kim (Parents)

Chan Hyuk Park, So Young Park, Hye-Jung Han, and Ji-Yeon Park

For Their Boundless Love, Support, and Trust

ACKNOWLEDGEMENTS

From the bottom of my heart, I would love to express my gratitude to my research advisor, Professor William V. Giannobile, for the precious mentorship and support during the period of my graduate study. He is the greatest advisor, life-mentor, and father-in-lab having passion and energy in science and engineering as well as understanding everything with his warm encouragement.

I would also like to thank to my dissertation committee: Professor Scott J. Hollister, who provided valuable and thoughtful guidance to accomplish studies as a research co-advisor; Professor Peter X. Ma and Professor Shuichi Takayama have both provided precious scientific comments to improve my research and thesis and shape this research into what is has become today.

I very heartfelt appreciate my U.S. family. Due to their various support, encouragement, and fantastic team-work I could successfully complete my doctoral work with excellent academic achievements. James V. Sugai, the mother-in-lab and one of the most important

people in my entire life, has advised and supported everything for the graduate life as well as the experiments. Dr. Qiming Jin has made me inspired with enthusiasm in the scientific researches as a scientist and realized how to enjoy the science and life challenges. Dr. Mario Taba Jr. gratefully gave a lot of knowledge and background to understand periodontics and craniofacial biology in pre-clinical and clinical, which are greatly helpful to develop the periodontal engineering and pursue doctoral works. Dr. Joni A. Cirelli preciously advised me about animal studies and molecular biology in periodontal researches to design my interdisciplinary and translational Ph.D. study with great research motivation. Dr. Zhao Lin and Dr. Po-Chun Chang, the greatest brothers-in-lab and science colleagues, shared biological sciences, engineering knowledge, and our experiences to develop the wider scientific spectra. Moreover, from my lovely sister-in-lab, Dr. Julie T. Marchesan, I have not only learned immunological biology background and various clinical challenges in periodontics but also known the most attractive cultures of Brazil, where become my most favorites. Dr. Hector F. Rios gratefully assisted many animal surgeries and instructed *in-vivo* experimental techniques for very challengeable microsurgeries. I appreciate Professor Yang-Jo Seol in Seoul National University, who encouraged and motivated me with scientific inspiration to accomplish challengeable and innovative works. I would also acknowledge my undergraduate students; Seokchun (Scott) Lim, Megan E. Bland, Erica Yi, post-/present-lab members; Nancy Chen, Zachary Abramson, Drew DiGiore, Rachael Jun, Lindsay Rayburn, TJ Daws, Lea Franco, Ashley Chung, Kathryn Kempeinen, Min Oh, Andrei Taut, Mallory Mitchell, Alexandra Plonka, and Lauryn Pitts (Giannobile Lab), visiting scholars; Drs. Ana Carolina Morandini, Valeria Navarro (from Brazil), Reinhard Gruber, Andreas Wiesbauer, Lukas Fürhauser

(from Austria), Gaia Rosa Pellegrini, Salvatore Batia, Andrea Ottonello, Roberto Farina (from Italy), and Graduate Periodontics Program; Drs. Thiago Santos, Giorgio Pagni, Angie Lee, Hsun-Liang (Albert) Chan. In particular, I appreciate that Dr. Darnell Kaigler and Dr. Rodrigo Neiva provided precious opportunities; the first clinical development and trial of the micro-computed tomography (micro-CT) methodology for the dental implantology. This clinical application has eventually become the precise and accurate evaluation methodology for alveolar bone regeneration for the dental implant stability.

I really feel thankful to the department of Biomedical Engineering (BME) for the greatest interdisciplinary education and financial support to successfully complete my Ph.D. program. Moreover, I appreciate Orthopaedic Research Laboratories (ORL) members, Dr. Steven A. Goldstein, Jaclynn M. Kreider and Dr. Jeffrey Megnack to facilitate and support professional background about the micro-CT and other medical imaging technologies. I would also like to thank Dr. Sunil Kapila and Dr. Mathew D. Dunn in Orthodontics and Pediatric Dentistry (OPD) for the orthodontic tooth movement application using micro-CT methodology, Dr. Tae-Geon Kwon in Kyungpook National University and all post-doctoral and research fellows; Drs. Nam Eok Joo, Jinkoo Kim, Serkin Park, Young (Young) Hun Jung, Sungsu Kim, Susan Tarle, Sarah Volk, Jennifer Fox in Periodontics and Oral Medicine (POM), Dr. Young Gun Ko in Bioologic and Materials Sciences (BMS), and Dr. Kyung-San Min in Cariology, Restorative Science and Endodontics (CRSE) in School of Dentistry. Moreover, Scaffold Tissue Engineering Group provided significant help for scaffold manufacture; Eiji Saito, Heesuk Kang,

Alisha Diggs, Huina Zhang, Jessica Kempainen, Annie Mitsak, Frank Winterroth, Shelley Brown, Yifei (Felix) Liu.

Here, I very importantly appreciate my undergraduate study advisors, Professor Sungsoo Kim, professor Kigook Song, and professor Sang-Hyon Paek in the Department of Chemical Engineering, Kyung Hee University. From undergraduate study, they have gratefully inculcated a sense of responsibility, ethics, and pleasure for scientific research even though we have physically long distance. I also have special thank to Professor Jinsang Kim at the University of Michigan. He has always exemplified to me as a true scholar with considerate and warm heart.

In my entire graduate life, I want to thank ***K-BME*** (Korean Student Association in BME) members; Hogene Kim, Samsung Huh, Daewoo Park, Jiwon Lee, Byoung Choul Kim, Eunjoo Hwang, Gu Eon Kang and ***K-BME-Alumni*** members; Drs. Jongbum Seo, Youngseon Choi, Huynjin Park, Kyungsup Shin, Donghwan (Richie) Kim, Gwangseong Kim, Taegyun Moon, Woonghee Lee, Hwan Kyu Lee, Dongwoo Lim, Ga Young (Claire) Jeong, Hwan Joo Park, Juyoung Park, Minsoung Rhee, Joon Seok (Paul) Chung, and Whijae Roh. I specially appreciate my classmates; Drs. Yunseok Heo, Jungwoo Lee, and Yoon-Chung Kim to support and make my graduate career much more fun. I greatly thank to Dr. Jinho Kim (my old roommate) and Hobin Kim.

Lastly and the most importantly, I would very much love to thank to my family, especially my parents; Dr. Chong Oon Park and Kyung Sun Kim with their boundless love and support to complete my Ph.D. work and my most lovely siblings; Chan Hyuk Park and Dr. So Young Park. My special thanks are given to my sister-in-law, Hye-Jung Han and a pretty niece, Ji-Yeon Park. If it had not been for their boundless love, support, encouragement, and strong trust over the years, I could not be here and complete my work with the great achievement. I really express my heartfelt gratitude for everything from my family.

TABLE OF CONTENTS

LIST OF FIGURES

LIST OF TABLES

ABSTRACT

Periodontal disease is a common chronic inflammatory disease, which if left untreated, can cause periodontal tissue breakdown. The periodontal complex is a micron-scaled, tooth-supporting structure with a complicated topology, which makes it difficult to predict and quantify periodontal tissue destruction. Unlike conventional assessment methods, 3-D micro-computed tomography provides very accurate, precise high resolution images of the periodontal topology.

Using natural spatiotemporal landmarks to create a region-of-interest from the roof-of-furcation to the root-apex, volumetric image analysis of the bone-tooth interface was performed. The results demonstrated excellent examiner reproducibility and reliability (ICC>0.99 and CV<1.5%) for both linear and volumetric bone parameters. In an orthodontic tooth movement study, micro-CT quantified the activity of osteoprotegerin stimulation to prevent bone resorption and tooth mobility. Human alveolar bone core biopsies were analyzed to obtain mineral tissue density profiles in order to predict dental implant stability. Because of this high reproducibility and reliability, other wide-reaching applications have potential for predicting periodontal therapy outcomes, orthodontic tooth movement, as well as evaluation of clinical dental implant stability.

A major challenge in periodontal tissue engineering is the control of periodontal tissue neogenesis; micron-scaled and complicated multi-interface regeneration with a functional architecture. To promote this compartmentalized, multiple tissue regeneration with perpendicularly-oriented periodontal ligament fiber, a multi-layered hybrid scaffold was designed and manufactured using the rapid prototyping technique. To produce a periodontium-like environment, the polymeric hybrid scaffold was assembled with a periodontal cell/tissue guidable micro-architecture; a highly porous bone region, a vertically-oriented PDL architecture, and a human tooth dentin slice. This complex was subcutaneously transplanted with untreated human PDL cells and BMP-7 transduced human gingival fibroblast cells using the ectopic model system. In spite of non-biomechanical loading conditions, this approach resulted in periodontal-structural similarity. There was a perpendicular/oblique orientation of the fibrous connective PDL cells/tissues to the dentin surface, and mineralized tissue formation without any mineralized tissue formation in the PDL interface of the hybrid scaffold at both the 3 and 6 weeks.

This dissertation study provides potential for functional restoration of tissue interface neogenesis applications and shows promise for both pre-clinical and clinical applications for translational regenerative medicine.

CHAPTER ONE

INTRODUCTION

1.1 Background of Periodontal Tissues and Disease Progression

The periodontium is composed of four different tissues: alveolar bone, cementum, periodontal ligament (PDL), and gingiva (Fig. 1.1A). Cementum is the calcified tissue covering the tooth root surfaces from the cementoenamel junction (CEJ) to the tooth root apex. It is an important component because it is the site where the PDL is attached to the tooth root. PDL is a fibrous, viscoelastic, vascularized soft tissue with a specific orientation, perpendicularly anchored between alveolar bone and cementum [1]. By providing a well-organized fibrous network to the periodontium, the PDL has a nutritive function for various cell types to survive and maintain the vitality of the periodontium. The gingiva covers and protects the tooth and alveolar bone through attachment of the connective tissues.

Periodontitis is a common, highly prevalent inflammatory infectious disease affecting periodontal tissues in adult humans [2]. This disease is initiated by bacteria and bacterial products such as lipopolysaccharides (LPS), which can stimulate cytokines to then signal precursor cells to differentiate and activate osteoclasts [3]. Disease progression will lead

to destruction of the periodontal complex, followed by hard tissue resorption and subsequent tooth loss.

1.2 Current Approaches in Tissue Engineering and Regenerative Medicine

Tissue engineering and regenerative medicine are emerging areas within medical dental, engineering, and other research disciplines. Current studies seek to regenerate hard or soft tissues lost as a consequence of disease by using developed biocompatible and osteoconductive polymeric biomaterials, containing bioactive signaling molecules [4, 5]. However, periodontal tissue regeneration is limited and unpredictable for regeneration of biologically complex structures [5-7]. In order to improve tissue restoration rate and quality, bone morphogenetic proteins (BMPs), growth factors such as platelet-derived growth factor (PDGF), vascular endothelial growth factor (VEGF), and fibroblast growth factor (FGF), or other biomolecules, have been used for the stimulation of tissue formation. These growth factors have been used in order to optimize bioavailability and bioactivity within tissue regeneration applications. PDGF has been extensively researched in periodontics in order to improve healing of periodontal defects [8, 9]. PDGF can lead to migration, proliferation, and differentiation of various cell types within the periodontium. Our lab has demonstrated PDGF can enhance alveolar bone formation as well as promote periodontal soft tissue wound healing and tissue regeneration [10, 11]. We have also shown PDGF delivery stimulates cells isolated from the periodontium (fibroblasts, PDL, cementoblasts) and induces osteoblast mitogenesis and proliferation *in-vitro* and *in-vivo* [12, 13].

As the paradigm shifts in orthopedic or dental research from tissue replacement to tissue regeneration, scaffold designing and manufacturing has rapidly developed in order to provide appropriate biological microenvironments in desired disease or defect sites. It is still difficult to deliver signaling proteins or recombinant growth factor genes targeting specific regions of disease using systemic administration. Systemic administration strategies for genes, proteins, drugs, or other factors have other limitations for delivery: 1) the availability to affect other organs, 2) requirement of high concentrations and amounts of factors, and 3) uncontrolled and unpredictable bioactivities of factors at distant wound sites. To overcome these limitations, localized and sustained delivery of growth factors is one approach using biodegradable scaffolds. For example, ceramic, hydroxyapatite (HA), material has osteoconductive characteristics to stimulate osteoblast cells for mineralized tissue formation [14-16]. Polymeric materials such as PGA, PLA, or their copolymers have also been used for hard and soft tissue regeneration in orthopedic wound healing processes with interconnective structures [17, 18]; For complex, heterogenous tissue formation, hybridized microarchitectures with polymer/polymer or polymer/ceramic materials are being developed and applied to periodontal tissue or hard/soft tissue repair [9, 19-23]. Polyglycolide/poly-L-lactide (PGA/PLLA) composite scaffolds have been suggested for use to develop embryonic teeth. A heterogenic polymeric scaffold was used to generate enamel, dentin, and pulp tissues over a period of 25 weeks [24]. PGA and polyglycolide-co-lactide (PLGA) scaffolds led to regeneration of hybrid tooth-alveolar bone in the omenta of adult rats in order to repair periodontal tissues lost due to disease [25]. Drug-loaded biodegradable scaffold approaches used to heal wounds and regenerate tissues showed potential to control release rates of gene therapy vectors and provide a

suitable 3-dimensional microenvironment for the growth and differentiation of cells [26-29]. These approaches can release growth factors or drugs at desired sites following designed scaffold degradation rates. Various local delivery systems using microenvironments of scaffolds in combination with growth factors have been utilized for tissue formation [30-33].

These scaffold implant studies in periodontal disease defects have demonstrated well-developed tissue regeneration. However, unpredictable tissue overgrowth and ankylosis has been a limitation for current periodontal regeneration studies. It is advantageous to apply sophisticated and streamlined architectures in order to implant or transplant complex geometrical scaffolds into irregular periodontal defects. In periodontal tissue engineering, accuracy can be provided by computer-based designed scaffolds with digitized imaging techniques of micro-CT.

1.3. Micro-Computed Tomography Applications in Tissue Engineering

Micro-computed tomography (micro-CT) imaging techniques allows for 3-D determination of precise anatomical periodontal defects and periodontal disease progression by analyzing bone volumetric parameters: bone volume, bone volume fraction (BVF), bone mineral content, and bone mineral density (BMD). Basically, micro-CT uses radiography to detect elements such as calcium and phosphate within mineralized tissue with high intensities rather than other organic or non-mineralized materials. Micro-CT is a new technology which avoids destruction of specimens and is highly reproducible [34]. Three-dimensional images are generated and analyzed to

accurately model the size of particular cavities or periodontal defects [35]. An image-based scaffold design with photopolymerizing synthetic materials has been developed by Hollister, et al. Based on micro-CT or micro-magnetic resonance imaging (micro-MRI) information, three-dimensional structures can be reconstructed. With computer-aided design (CAD), complicated, solid geometric models can be designed and produced by 3-D printing [36] or selective laser sintering (SLS) techniques, such as ink-jet printing and photopolymerization manufacturing, respectively, or a soft-lithographic technique which has been used for fabrication of PLGA scaffolds [37-40]. Solid Free Form (SFF) fabrication [41] and computer-based design techniques are advantageous and useful because they provide anatomical accuracy and appropriate three-dimensional geometry of the craniofacial complex [37, 42-44]. From computer-aided scaffold fabrication, mechanical properties also can be characterized and structures can be designed with internal and external architectural pores [32, 40, 45-47]. Recently, simple computer-designed scaffolds have limitations *in-vivo* because the pore sizes used are larger than cells and they cannot provide enough cell-adhesion affinity [31, 37]. Therefore, one method for manufacturing smaller pores is indirect SFF fabrication. Because each tissue has been grown within its microenvironment, hybrid or composite scaffold design by computer has been suggested [16, 48].

1.4. Statements of Purpose and Dissertation Overview

As in Figures 1.1B and 1.2B, ankylosis on the root surface resulted in design and implantation of single, homogeneous scaffolds. Scaffolds are customized to match accurate periodontal defect shapes with computer software and each scaffold is

incorporated as one hybrid scaffold. Each different scaffold can play a role as a critical tissue barrier, such as for PDL or alveolar bone, and provide microenvironments to regenerate each periodontal tissue. The physical interface between dissimilar materials of the hybrid scaffold will help prevent osteoblast or fibroblast cell migration toward either a polymeric scaffold or ceramic scaffold, respectively. The interface from this multi-layered design with different materials provides physical barriers to block undesired tissue growth and penetration. Different biomaterials are selected for the interface between polymeric and composite scaffolds, and play a key role in preventing undesired tissue penetration. Moreover, polymer channels for PDL restoration in a PGA/PLA scaffold help to align the fibrous cells and regenerated fibrous tissue. That is, this tissue will be generated with a specific orientation following the channel-type scaffold. Therefore, computer-designed hybrid scaffolds can precisely fit anatomical defect sites and micro-CT imaging techniques provide an important role in guiding the formation of new alveolar bone and fibrous ligament tissues into the desired shapes in periodontal tissue regeneration.

Currently, restoration or regeneration of tissue lost from disease progression are focused on regeneration of a single tissue using systemic or local delivery of various growth factors or bioactive molecules with synthetic material scaffolds as a carrier. Based on the background information, the proposed hybrid scaffold design, incorporated with micro-CT imaging techniques, will improve and promote multiple tissue formation, in one localized delivery system. This hybrid scaffold will be designed using micro-CT digitized

images according to surgical defect sites or anatomical configuration of the periodontal apparatus.

1.5 FIGURES

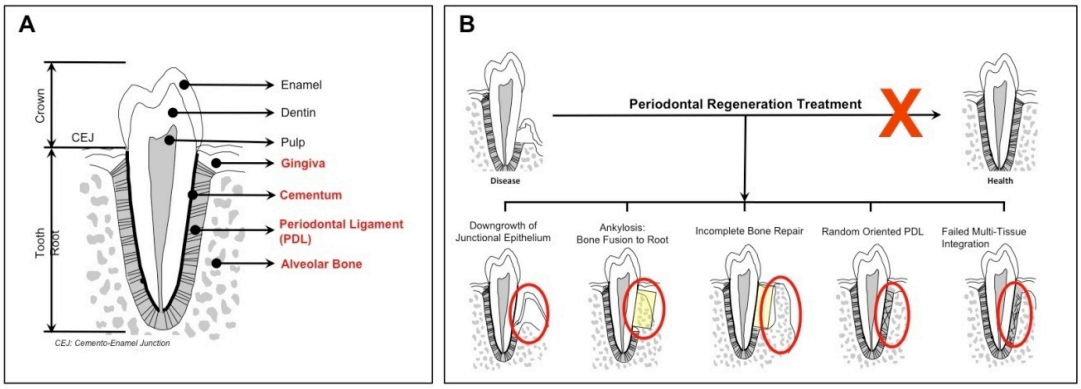

Figure 1.1 Schematic illustration of periodontal tissue and limitations of periodontal therapies. (A) The terminologies of tooth and tooth-supporting structures with the red-colorized text signifying periodontal tissues. **(B)** Typical limitations of current periodontal treatment. Red circles indicate examples of the failures of periodontal regeneration treatments.

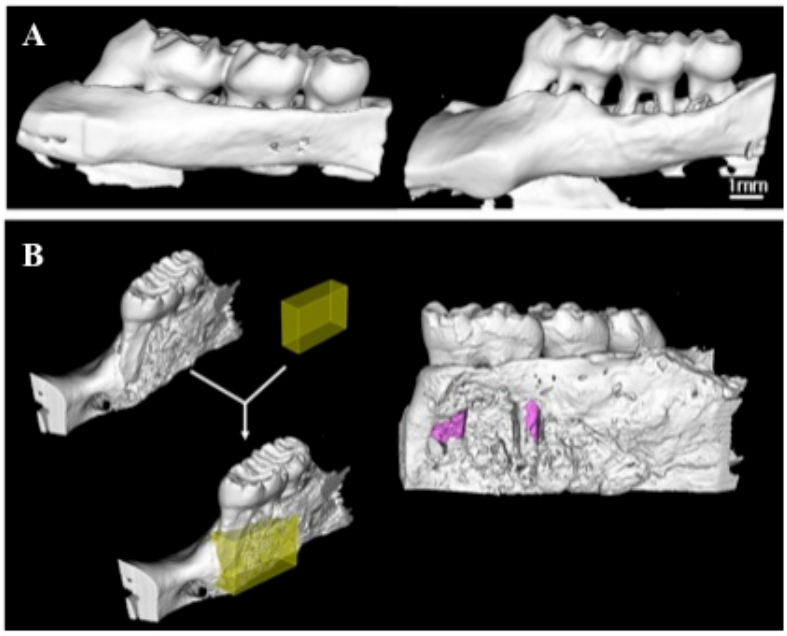

Figure 1.2. (A) Experimental periodontitis model in rats using micro-computed tomographic (micro-CT) images visualized by reconstructing into 3-dimensional images. Non-diseased or healthy rat maxilla (left image). The specimen shows the bone crest level is flat and even in height. In the periodontal diseased rat maxilla after 8 weeks (right image), the alveolar bone crest level is measurably decreased and roots are visibly exposed. With this specimen, the periodontitis progression can be diagnosed around all molar teeth. **(B) Visualization of conventional scaffold implantation and ankylosis in a regeneration study in rats.** Periodontal surgical defects were created around the 1st molar on the buccal side of mandible. Single polymeric scaffold (yellow block) with growth factor genes will be designed and implanted to the defect area for 5 weeks (left panel). The result of reconstructive therapy is represented as alveolar bone regeneration on the root surfaces. The highlighted area (purple-colorized area) shows ankylosis on mesial and distal root surfaces (right panel).

1.6 REFERENCES

1. Sanctuary CS, Wiskott HW, Justiz J, Botsis J, Belser UC. In vitro time-dependent response of periodontal ligament to mechanical loading. J Appl Physiol 2005 Dec;99(6):2369-2378.

2. Keles GG, Acikgoz G, Ayas B, Sakallioglu E, Firatli E. Determination of systemically & locally induced periodontal defects in rats. Indian J Med Res 2005 Mar;121(3):176-184.

3. Taba M, Jr., Kinney J, Kim AS, Giannobile WV. Diagnostic biomarkers for oral and periodontal diseases. Dent Clin North Am 2005 Jul;49(3):551-571, vi.

4. Somerman MJ, Ouyang HJ, Berry JE, Saygin NE, Strayhorn CL, D'Errico JA, et al. Evolution of periodontal regeneration: from the roots' point of view. J Periodontal Res 1999 Oct;34(7):420-424.

5. Wang HL, Greenwell H, Fiorellini J, Giannobile W, Offenbacher S, Salkin L, et al. Periodontal regeneration. J Periodontol 2005 Sep;76(9):1601-1622.

6. Koo KT, Polimeni G, Albandar JM, Wikesjo UM. Periodontal repair in dogs: analysis of histometric assessments in the supraalveolar periodontal defect model. J Periodontol 2004 Dec;75(12):1688-1693.

7. Koo KT, Polimeni G, Qahash M, Kim CK, Wikesjo UM. Periodontal repair in dogs: guided tissue regeneration enhances bone formation in sites implanted with a coral-derived calcium carbonate biomaterial. J Clin Periodontol 2005 Jan;32(1):104-110.

8. Anusaksathien O, Giannobile WV. Growth factor delivery to re-engineer periodontal tissues. Curr Pharm Biotechnol 2002 Jun;3(2):129-139.

9. Sarment DP, Cooke JW, Miller SE, Jin Q, McGuire MK, Kao RT, et al. Effect of rhPDGF-BB on bone turnover during periodontal repair. J Clin Periodontol 2006 Feb;33(2):135-140.

10. Giannobile WV. Periodontal tissue engineering by growth factors. Bone 1996 Jul;19(1 Suppl):23S-37S.

11. Jin Q, Anusaksathien O, Webb SA, Printz MA, Giannobile WV. Engineering of tooth-supporting structures by delivery of PDGF gene therapy vectors. Mol Ther 2004 Apr;9(4):519-526.

12. Giannobile WV, Lee CS, Tomala MP, Tejeda KM, Zhu Z. Platelet-derived growth factor (PDGF) gene delivery for application in periodontal tissue engineering. J Periodontol 2001 Jun;72(6):815-823.

13. Zhu Z, Lee CS, Tejeda KM, Giannobile WV. Gene transfer and expression of platelet-derived growth factors modulate periodontal cellular activity. J Dent Res 2001 Mar;80(3):892-897.

14. Mankani MH, Kuznetsov SA, Avila NA, Kingman A, Robey PG. Bone formation in transplants of human bone marrow stromal cells and hydroxyapatite-tricalcium phosphate: prediction with quantitative CT in mice. Radiology 2004 Feb;230(2):369-376.

15. Seitz H, Rieder W, Irsen S, Leukers B, Tille C. Three-dimensional printing of porous ceramic scaffolds for bone tissue engineering. J Biomed Mater Res B Appl Biomater 2005 Aug;74(2):782-788.

16. Taboas JM, Maddox RD, Krebsbach PH, Hollister SJ. Indirect solid free form fabrication of local and global porous, biomimetic and composite 3D polymer-ceramic scaffolds. Biomaterials 2003 Jan;24(1):181-194.

17. Liu X, Ma PX. Polymeric scaffolds for bone tissue engineering. Ann Biomed Eng 2004 Mar;32(3):477-486.

18. Ma PX, Choi JW. Biodegradable polymer scaffolds with well-defined interconnected spherical pore network. Tissue Eng 2001 Feb;7(1):23-33.

19. Papantoniou V, Ptohis N, Tsiouris S. Diffuse tracer uptake in scintimammography: not as nonspecific or benign as originally believed? J Nucl Med 2006 Mar;47(3):554-555; author reply 555.

20. Schek RM, Wilke EN, Hollister SJ, Krebsbach PH. Combined use of designed scaffolds and adenoviral gene therapy for skeletal tissue engineering. Biomaterials 2006 Mar;27(7):1160-1166.

21. Wei G, Jin Q, Giannobile WV, Ma PX. Nano-fibrous scaffold for controlled delivery of recombinant human PDGF-BB. J Control Release 2006 May 1;112(1):103-110.

22. Wei G, Ma PX. Structure and properties of nano-hydroxyapatite/polymer composite scaffolds for bone tissue engineering. Biomaterials 2004 Aug;25(19):4749-4757.

23. Wei G, Ma PX. Macroporous and nanofibrous polymer scaffolds and polymer/bone-like apatite composite scaffolds generated by sugar spheres. J Biomed Mater Res A 2006 Aug;78(2):306-315.

24. Young CS, Kim SW, Qin C, Baba O, Butler WT, Taylor RR, et al. Developmental analysis and computer modelling of bioengineered teeth. Arch Oral Biol 2005 Feb;50(2):259-265.

25. Young CS, Abukawa H, Asrican R, Ravens M, Troulis MJ, Kaban LB, et al. Tissue-engineered hybrid tooth and bone. Tissue Eng 2005 Sep-Oct;11(9-10):1599-1610.

26. Cooke JW, Sarment DP, Whitesman LA, Miller SE, Jin Q, Lynch SE, et al. Effect of rhPDGF-BB delivery on mediators of periodontal wound repair. Tissue Eng 2006 Jun;12(6):1441-1450.

27. Franceschi RT. Biological approaches to bone regeneration by gene therapy. J Dent Res 2005 Dec;84(12):1093-1103.

28. Kaigler D, Cirelli JA, Giannobile WV. Growth factor delivery for oral and periodontal tissue engineering. Expert Opin Drug Deliv 2006 Sep;3(5):647-662.

29. Doukas J, Chandler LA, Gonzalez AM, Gu D, Hoganson DK, Ma C, et al. Matrix immobilization enhances the tissue repair activity of growth factor gene therapy vectors. Hum Gene Ther 2001 May 1;12(7):783-798.

30. Bateman J, Intini G, Margarone J, Goodloe S, Bush P, Lynch SE, et al. Platelet-derived growth factor enhancement of two alloplastic bone matrices. J Periodontol 2005 Nov;76(11):1833-1841.

31. Lin CY, Schek RM, Mistry AS, Shi X, Mikos AG, Krebsbach PH, et al. Functional bone engineering using ex vivo gene therapy and topology-optimized, biodegradable polymer composite scaffolds. Tissue Eng 2005 Sep-Oct;11(9-10):1589-1598.

32. Sun W, Starly B, Nam J, Darling A. Bio-CAD modeling and its applications in computer-aided tissue engineering. Computer-Aided Design 2005;37:1097-1114.

33. Capito RM, Spector M. Scaffold-based articular cartilage repair. IEEE Eng Med Biol Mag 2003 Sep-Oct;22(5):42-50.

34. Sherick DG, Buchman SR, Goulet RW, Goldstein SA. A new technique for the quantitative analysis of cranial suture biology. Cleft Palate Craniofac J 2000 Jan;37(1):5-11.

35. Park C, Abramson Z, Taba Jr. M, Jin Q, Chang J, Kreider J, et al. Three-dimensional micro-computed tomographic imaging of alveolar bone in experimental bone loss and repair. J Periodontol 2007;77:in press).

36. Chen VJ, Smith LA, Ma PX. Bone regeneration on computer-designed nano-fibrous scaffolds. Biomaterials 2006 Jul;27(21):3973-3979.

37. Hollister SJ. Porous scaffold design for tissue engineering. Nat Mater 2005 Jul;4(7):518-524.

38. Manjubala I, Woesz A, Pilz C, Rumpler M, Fratzl-Zelman N, Roschger P, et al. Biomimetic mineral-organic composite scaffolds with controlled internal architecture. J Mater Sci Mater Med 2005 Dec;16(12):1111-1119.

39. Vozzi G, Flaim C, Ahluwalia A, Bhatia S. Fabrication of PLGA scaffolds using soft lithography and microsyringe deposition. Biomaterials 2003 Jun;24(14):2533-2540.

40. Williams JM, Adewunmi A, Schek RM, Flanagan CL, Krebsbach PH, Feinberg SE, et al. Bone tissue engineering using polycaprolactone scaffolds fabricated via selective laser sintering. Biomaterials 2005 Aug;26(23):4817-4827.

41. Schek RM, Taboas JM, Segvich SJ, Hollister SJ, Krebsbach PH. Engineered osteochondral grafts using biphasic composite solid free-form fabricated scaffolds. Tissue Eng 2004 Sep-Oct;10(9-10):1376-1385.

42. Hollister SJ, Levy RA, Chu TM, Halloran JW, Feinberg SE. An image-based approach for designing and manufacturing craniofacial scaffolds. Int J Oral Maxillofac Surg 2000 Feb;29(1):67-71.

43. Levy RA, Chu TM, Halloran JW, Feinberg SE, Hollister S. CT-generated porous hydroxyapatite orbital floor prosthesis as a prototype bioimplant. AJNR Am J Neuroradiol 1997 Sep;18(8):1522-1525.

44. Mao JJ, Giannobile WV, Helms JA, Hollister SJ, Krebsbach PH, Longaker MT, et al. Craniofacial tissue engineering by stem cells. J Dent Res 2006 Nov;85(11):966-979.

45. Hung CT, Lima EG, Mauck RL, Takai E, LeRoux MA, Lu HH, et al. Anatomically shaped osteochondral constructs for articular cartilage repair. J Biomech 2003 Dec;36(12):1853-1864.

46. Hutmacher DW, Sittinger M, Risbud MV. Scaffold-based tissue engineering: rationale for computer-aided design and solid free-form fabrication systems. Trends Biotechnol 2004 Jul;22(7):354-362.

47. Wettergreen MA, Bucklen BS, Sun W, Liebschner MA. Computer-aided tissue engineering of a human vertebral body. Ann Biomed Eng 2005 Oct;33(10):1333-1343.

48. Sherwood JK, Riley SL, Palazzolo R, Brown SC, Monkhouse DC , Coates N et al. A three-dimensional osteochondral composite scaffold for articular cartilage repair. Biomaterials 2002 Dec;23(24):4739-4751.

CHAPTER TWO

MICRO-COMPUTED TOMOGRAPHIC (MICRO-CT) METHODOLOGY DEVELOPMENT FOR PERIODONTAL DISEASE PROGRESSION

Park CH, Abramson ZR, Taba Jr. M, Jin Q, Chang J, Kreider JM, Goldstein SA, Giannobile WV.

Journal of Periodontology, **2007** 78(2): 273-281

2.1. ABSTRACT

BACKGROUND: Micro-computed tomography (micro-CT) offers significant potential for identifying mineralized structures. However, three-dimensional (3-D) micro-CT of alveolar bone has not been readily adapted for quantification. Moreover, conventional methods are not as sensitive for analyzing bone loss or bone gain following periodontal disease or reconstructive therapy. The objective of this investigation was to develop a micro-CT methodology for quantifying tooth-supporting alveolar bone in 3-D following preclinical situations of periodontitis or reconstructive therapy.

METHODS: An experimental *in vivo* bone loss and prevention model was developed to validate the micro-CT imaging technique. Twenty mature Sprague-Dawley rats were

divided into two groups: bone loss (Porphyromonas gingivalis lipopolysaccharide-mediated bone resorption) and regenerative therapy. Micro-CT software-digitized specimens were three-dimensionally reconstructed for linear and volumetric parameter assessment of alveolar bone (linear bone height, bone volume, bone volume fraction, bone mineral content, and bone mineral density). Intra- and inter-examiner reproducibility and reliability were compared for methodology validation.

RESULTS: The results demonstrated high examiner reproducibility for linear and volumetric parameters with high intraclass correlation coefficient (ICC) and coefficient of variation (CV). The ICC showed that the methodology was highly reliable and reproducible (ICC >0.99; 95% confidence interval, 0.937 to 1.000; CV <1.5%), suggesting that 3-D measurements can provide better alveolar bone analysis than conventional 2-D methods.

CONCLUSIONS: The developed method allows for highly accurate and reproducible static measurements of tooth-supporting alveolar bone following preclinical situations of bone loss or regeneration. Future investigations should focus on using *in vivo* micro-CT imaging for real-time assessments of alveolar bone changes.

2.2. INTRODUCTION

Because of the non-uniformity and porous structure of alveolar bone and its close proximity to dental structures, it is difficult to quantify. Current approaches that attempt to quantify alveolar bone include histomorphometry, two-dimensional (2-D) radiography, and more recently, micro-computed tomography (micro-CT) [1, 2]. Although histomorphometry provides high resolution and direct representation of alveolar bone levels, there are obvious limitations, such as tissue sample destruction and challenges reconstructing a three dimensional (3-D) image [3]. Radiographic methods overcome many of these challenges by providing non-destructive 2-D imaging capabilities using sequential or serial images of alveolar bone and teeth while monitoring disease progression. However, the inconsistency in maintaining nearly identical alignment of successive radiographic images complicates this process [4].

Micro-CT or medical CT is a non-invasive technique that can be used in 3-D to image specimens on a micron-resolution level and allows for computer-aided reorientation following image scanning, thus assuring nearly identical alignment [1]. Micro-CT use for preclinical applications provides higher spatial resolution images than medical or dental CT for clinical assessments [5]. Using this technique, micro-CT scans will show slight deviations in periodontal defects or cases of alveolar bone loss on a 3-D level [5, 6]. In contrast, a study examining the reliability and accuracy of 2-D dental radiographs demonstrated differences of up to 25% between calculations quantifying alveolar bone from 2-D radiographs and 3-D CT scans [7].

Conventional radiographic approaches assessing alveolar bone structure are limited by the fact that 3-D microarchitecture cannot be inferred from isolated 2-D images [8]. However, micro-CT produces 3-D images of bone, allowing for detailed analysis of 3-D bone architecture and anisotropy. A study using micro-CT allowed examination of the mechanical behavior of bone in the attainment and maintenance of dental implant osseointegration. Assessment of the cancellous bone structure of maxillae and mandibulae from human cadavers revealed useful information about prognosis following implant reconstruction [9].

Despite these advantages associated with micro-CT imaging, certain challenges have been raised regarding reproducible osseous quantification of bone loss from periodontal disease or regeneration following post-regenerative therapy. Alveolar bone poses unique quantification problems because of the difficulty distinguishing it from surrounding dental hard tissues as a result of similarities in their x-ray attenuation [10]. Typically, computer-assisted image analysis facilitates this process when the tissue of interest differs in density from the surrounding structures. For example, during quantification of trabecular bone, which significantly differs in density from non-bony constituents in the marrow space, an analysis algorithm can be devised to accurately separate bone from non-bone elements within the region of interest (ROI). In contrast, the anatomy and morphology of tooth-associated periodontal defects make density thresholding quite challenging. In periodontal tooth–bone defects, there is little difference in density between the tooth-supporting alveolar bone and the tooth roots, which are composed of

hard tissue dentin and cementum separated by a thin fibrous tissue area (~150 to 200 μm) of intervening periodontal ligament.

For this investigation, a reproducible method was developed for quantifying and assessing alveolar bone using high-resolution micro-CT employing an interactive image analysis technique to evaluate selected 3-D ROIs for tooth-supporting alveolar bone defects. This new methodology is readily and easily adaptable for preclinical assessments of linear and volumetric alveolar bone parameters following disease, trauma, or regeneration.

2.3. MATERIALS AND METHODS

Experimental specimens

All animal procedures were performed under guidelines approved by the University of Michigan, Unit of Laboratory Animal Medicine (ULAM) for the use of animals in scientific research.

Experimental Bone Loss: Periodontal Disease Model

Experimental alveolar bone loss was induced utilizing *Porphyromonas gingivalis* lipopolysaccharide (*P. gingivalis* LPS). In brief, 12 adult male Sprague-Dawley rats (approx. weight 250 g each; Harlan World Headquarters, Indianapolis, IN USA) had experimental periodontitis induced by delivery of *P. gingivalis* W83 endotoxin (10 µL of a 1.0 mg/mL preparation) by injection into the interdental gingivae between the maxillary first (M1), second (M2), and third molars (M3), and the mesial aspect of M1 under isoflurane general anesthesia. These administrations were repeated three times per week over an 8-week period. The injections were performed utilizing custom-designed 0.375 in x 33 ga, 30º bevel needles attached to 50µL Hamilton syringes (Hamilton Company, Reno, NV USA). The animals were divided into 3 groups: 1) pre-treatment baseline (n=4), 2) no disease post-protocol at 8 weeks (n=4), and 3) LPS-mediated bone loss group (n=4). At baseline for group 1 and at 8 weeks for groups 2 and 3 the animals were sacrificed. Maxillary block biopsies were harvested, fixed in 10% formalin for 2 days, and stored in 70% ethanol for micro-CT scanning.

Experimental Bone Regeneration: Periodontal Fenestration Defect Model

An alveolar bone fenestration defect model was used to measure bone repair following surgical creation of bone defects at the mesial root of the mandibular first molar as previously described by Jin *et al*. In brief a total of eight ~250 g athymic rats (Hsd:RH-rnu/rnu) (n= 4 per group), were anesthesized using ketamine (Ketaset®, Fort Dodge Animal Health, Fort Dodge, IA USA) and xylazine (AnaSet®, Lloyd Laboratories, Shenandoah, IA USA). Alveolar bone defect osteotomies were created by initially preparing an extraoral 2-cm superficial skin incision at the lower border of the mandible. The superficial fascia and underlying masseter muscle were separated with sharp dissection and the ligamentary attachment of the masseter muscle to bone was severed at its inferior base, and both the masseter and periosteum were elevated from the bone to expose the buccal plate of the mandible. The oral mucosa on the superior wall of the surgically created osteotomy was identified, and its attachment to the intraoral keratinized gingival margin was maintained during defect preparation. The bone overlying the mandibular first molar was removed with a high-speed handpiece under saline irrigation while visualizing with a surgical microscope (Model: SMZ 1000, Nikon, Melvile, NY USA). The distal root of the first molar tooth (d-M1) was carefully denuded of periodontal ligament, overlying cementum, and superficial dentin. The defects measured approximately 0.3w x 0.2h x 0.15d cm in dimension. Polylactic glycolic acid (PLGA) scaffolds seeded with 2.5 x 10^5 non-transduced cells (scaffold-alone control) were placed in the defects or PLGA scaffolds 2.5 x 10^5 with genetically-modified stem cells as previously described. The internal wounds were approximated with resorbable 5-0 chromic gut sutures and the external skin incisions closed with surgical staples. The

animals were administered supplemental antibiotics (ampicillin 268 mg/ml of drinking water) provided daily for 14 days. At five weeks, the animals were euthanized and mandibular block biopsies were harvested, fixed in 10% formalin for 2 days, stored in 70% ethanol for scanning by micro-CT.

Micro-computed tomography instrumentation and image capture

All maxillary and mandibular block biopsies were subjected to micro-CT image analysis as described below. The cone-beam micro-CT scanner utilized in this study was developed by General Electric Enhanced Vision Systems Ltd. (EVS). Fig. 2.1 illustrates the main components of the scanner for alveolar bone applications: an x-ray source, a specimen stage, an image detector and camera, an image processing system, and a micro-computer cluster for visualization and analysis. The x-ray generator was operated at an accelerated potential of 80kV with a beam current of 80μA. The x-ray source combines with a 2-D detector operating with a shutter speed of 1100 ms, which produces images with a voxel size of 18 x 18 x 18μm^3. We used an internal reference in micro-CT units (i.e. bone mineral density, mg/cc) for each scan.

The 3-D volume viewer and analyzer eXplore MicroView® v. 2.0. (Analysis Plus™, GE Healthcare, London ON Canada). MicroView® is the software tool for the visualization and quantification of 2-D and 3-D data on a personal computer output. Post-processing images were colorized using Adobe Photoshop CS2 v. 9.0 (Adobe Systems Inc., San Jose, CA USA).

Linear and Volumetric Alveolar Bone Measurements

Linear measurements

Linear measurements (mm) were from the cemento-enamel junction (CEJ) to the alveolar bone crest (ABC) in the interdental region between either the first and second molar teeth (M1-M2), or between the second and third molar teeth (M2-M3) respectively. All images were reoriented such that both the CEJ and the root apex (RA) appeared within the micro-CT slice to be analyzed. Root length measurements (in mm) from CEJ to the RA were also taken from each root in order to assess the percentage of vertical bone remaining (Fig. 2.2b). In order to assess the amount of regenerated bone tissue in the reconstructive therapy group, the exposed root length of the d-M1 was measured (in mm). The linear fractions as noted below in equation 3 represent the linear amount of regenerated bone tissue covering the surgically created dehiscence lesion.

Volumetric micro-CT measurements

Volumetric measurements were carried out following selection of each 3-D ROI. Two examiners (CHP and ZA) were guided by morphological landmarks when drawing ROIs in order to ensure repeatability. While artificial landmarks could have been placed prior to the scanning of the specimens, it was more reproducible and more accurate to use given morphological features (e.g., outer root prominences and root furcations). In the case of periodontal defects resulting from experimental periodontitis, the majority of bone loss was noted around the roots of the teeth, below the roofs of the furcations (ROF),

and above the root apices. Our method took advantage of this feature by using both the ROFs and the RAs as references identifying the borders of the ROIs (Fig. 2.2a).

The most mesial root of M1 (m-M1) and the most d-M3 served as endpoint landmark borders since they were the most consistent among specimens. Thus, reorientation of specimens from examiner to examiner relied upon the capturing of these landmarks, which essentially maximized the ROI of the alveolar bone housing of the alveolus. This critical reorientation of 3-D reconstructed images provided reproducible and reliable criteria to quantify and assess alveolar bone. In contrast, based on the examination of maxillae using the orientation stated above, the relative heights of the ROFs varied greatly. Thus, for all cases it was not feasible to start with one specific furcation each time. Consequently, contours were drawn immediately upon scrolling through the top of a furcation landmark (Fig. 2.2a).

Utilizing the landmarks RA, ROF, and RL, region contours were drawn at regular intervals (Fig. 2.2a and equations 1-3). The objective in drawing these contours was to maximize the quantification of bone, minimize the inclusion of tooth roots, and use as many reproducible landmarks as possible. All contours were drawn beginning immediately below the ROFs in the coronal plane moving in the apical direction. Using an advanced ROI tool, 2-D contours were drawn at regular intervals (every 8 data planes), depending on the variability between planes; greater variability between planes required contours to be drawn at smaller intervals (1-2 planes). Contours were drawn until

reaching the apices of m-M1 and d-M3. Next, a 3-D ROI was generated by the software based on the resultant 2-D contours (Fig. 2.2a and 2.2c). Finally, volumetric alveolar bone parameters of bone volume (BV), bone volume fraction (BVF), bone mineral content (BMC), and bone mineral density (BMD) in the volume of selected ROI were determined (Fig. 2.2c) using equations 4 and 5.

Equations used in 3-D image-measurement

$$Percent\ remaining\ bone(\%) = \frac{(Root\ length) - (CEJ - ABC)}{Root\ length} \times 100 \qquad \text{Equation 1}$$

$CEJ - ABC$: Distance from CEJ to ABC

$$Root\ Length = \frac{M1 + M2}{2}\ and\ \frac{M2 + M3}{2} \qquad \text{Equation 2}$$

Mi: Distance of the i^{th} molar root from CEJ to RA

$$\text{Linear Fraction} = \frac{\text{Length of exposed d} - \text{M1 root}}{\text{Total length of d} - \text{M1 root}} \qquad \text{Equation 3}$$

Total length of d-M1 root: Distance of the d-M1 root from CEJ to RA

$$\text{Bone Volume Fraction} = \frac{\text{Remaining bone volume in Volume of Interest}}{\text{Volume of Interest}} \qquad \text{Equation 4}$$

$$\text{Bone Mineral Content} = (\text{Bone Mineral Density}) \times (\text{Volume of Interest}) \quad \text{Equation 5}$$

Examiner Reliability and Statistical Analysis

Validation measures were conducted for both linear and volumetric micro-CT measurements. For the linear validation, eight different samples were analyzed by two independent examiners (CHP and ZA). After a period of 24 hours, linear distance measurements were repeated by both examiners in order to assess inter- and intra-examiner variability. Analogously, for the volumetric validation, one image was taken and six planes were selected for analysis: two planes near the crowns, two near the apices, and two in the mid-portion of the roots. The examiners independently prepared contours in the selected planes in order to assess volumetric parameters; BV, BVF, BMC, and BMD according to the formulae 4-5. Again, all volumetric measurements were repeated after 24 hours by both examiners to assess inter- and intra-examiner variability. In addition, one image was chosen and completely analyzed by both examiners, twice each, to determine agreements.

Mean values were generated for each of the groups evaluated. Coded specimens were analyzed using one-way analysis of variance (ANOVA) and Bonferroni's multiple comparison test to measure statistical differences among groups. The reliability and reproducibility was derived from the intra-class correlation coefficient (ICC). The range of values in ICC is from 0 to 1. When ICCs are closer to 1, reliability and reproducibility

are stronger and above 0.75 of ICC values show good reliability. The values were calculated with single measurements from a two-way random model and absolute agreement type. The reproducibility of measurement is represented with coefficient of variation [CV % = (Standard Deviation / its mean value) x 100] as well. The reproducibility and repeatability of duplicate micro-CT scanning also was calculated statistically by CV in which one sample was scanned once a day for 3 days. All volumetric results from the scans and the MicroView® software and calibration measurements were statistically evaluated using SPSS v.12 (SPSS Inc., Chicago, IL USA).

2.4. RESULTS

The methodologies for image capture, orientation, landmark identification, and measuring of linear and volumetric bone change, were noted to be reproducible and these methods are highlighted in Fig. 2.2 (method) and Fig. 2.3 (resultant changes in disease or repair). Moreover, 2-D and 3-D topographical alterations in bone levels in a bone loss situation (disease) or the bone gain situation (regeneration therapy) are shown in Fig. 2.4.

Linear micro-CT measurements

In the alveolar bone loss specimens, linear measurements within the interdental regions M1-M2 and M2-M3 demonstrated significant differences between the healthy and *P. gingivalis* LPS-induced periodontitis specimens. We measured CEJ-ABC distances among baseline and follow-up as shown in Fig. 2.3. As Figure 3a reveals, there was no significant difference between the baseline and vehicle only groups ($p>0.05$). However, when diseased periodontia were compared with healthy specimens at follow-up, statistically significant differences were found ($p<0.05$). In the reconstructive therapy specimens, the residual tooth root exposure was significantly reduced by genetically-modified cell therapy when compared to the control group (Fig. 2.3d; $p<0.05$). Colorized images depict bone gain over the previously debrided tooth root surface following reconstructive therapy (Figs. 2.4h-k; $p< 0.01$).

Volumetric Micro-CT Measurements

Using this methodology, we could obtain volumetric measurement results for multiple bone loss indices including BV, BVF, BMC, and BMC. For bone loss specimens, no statistically significant differences in volumetric bone parameters were found between the baseline and follow-up healthy (control) group ($p>0.05$). However, LPS-induced experimental periodontitis led to robust and statistically significant bone loss (BMD and BVF) when compared to the control group (Fig. 2.3b and 3c; $p<0.05$). As a result, among both experimental groups (disease and repair) we could quantitatively determine the amount of bone changes in both 2-D and 3-D (Figs. 2.3 and 4).

Reliability

The ICC for continuous agreement analysis was found to be highly reproducible. In summary, both examiners presented a very high inter-examiner and intra-examiner agreement, highlighting the reliability and reproducibility of this method (Table 2.1). Highly sensitive, reliable and reproducible measures were shown for the intraclass correlation coefficient (ICC>0.99; $0.937 \leq 95\%\ \text{C.I.} \leq 1.000$) leading to a standardized measurement method. CV demonstrated precise error for reproducibility with volumetric measurements. CV was less 1.5% in inter- and intra-examiner calibrations demonstrating excellent reproducibility and reliability of measurement. Moreover, micro-CT scanning was also highly reproducible and repeatable with very low precision errors. BVF and BMD had 0.837% and 2.0618% precision errors, respectively. Using our methods in these experimental preclinical situations revealed ability to quantify disease progression

in the situation of *P. gingivalis* LPS-mediated periodontitis or alveolar bone repair using regenerative cell therapy (Table 2.1.).

2.5. DISCUSSION

Traditionally, 2-D radiographic images and histomorphometry have provided linear data to enable investigators to make quantitative measurements associated with alveolar bone affected by periodontitis or following regenerative therapy [16, 17]. Although new technologies are available for 3-D assessment of bone volume, in general, approaches still measure 2-D images linearly after projection from 3-D real structures [18, 19]. These methods have limitations, such as the accuracy or the precision of measurements [20, 21]. Micro-CT techniques have the potential to overcome these limitations and provide a more accurate quantification method for 3-D assessment of bone [22, 23]. The volumetric technique described here demonstrated accurate and precise measurements of bone in cases of no disease, disease, and postreconstructive therapy (Fig. 2.4). Furthermore, intra- and interexaminer reliability data demonstrate no significant differences between examiners, suggesting that the method is reproducible. In fact, the inclusion of a third examiner also provided high agreement of reproducibility; CV <3% (data not shown). Our reorientation criteria and methodology provided reliability and consistency for quantifiable assessments for volumetric parameters (BV, BVF, BMC, and BMD), despite variability within micro- CT scan images.

Although histologic techniques provide spatial data from calcified and decalcified tissues, micro-CT enables visualization of detailed 3-D microarchitecture without artifactual alterations in anatomical tissue structure due to tissue processing, embedding, and sectioning. The correspondence between histologic and micro-CT data was explored by comparing digitized images from histologic sections to matching micro-CT 2-D planes;

both methods are qualitatively similar (6 to 8 μm thick and 18 μm thick; Figs. 2.4c and 4d) [5, 24]. Although cells cannot be observed in present micro-CT images, discrete changes in alveolar bone morphology and trabeculation can be assessed three-dimensionally (Fig. 2.4) [3, 25, 26]. High resolution 3-D micro-CT images provide a distinct advantage for observing hard tissues without tissue-processing treatments, which can result in the distortion of osseous structures [27, 28].

Wilensky *et al.* [10] showed that micro-CT imaging could overcome several problems of previous 2-D approaches and verified the quantification of bone loss following periodontitis. Central to our method was the use of enhanced image analysis which provided the technological ability to overcome many of the previous challenges in the quantification of alveolar bone [17, 19].

2.6. FIGURES

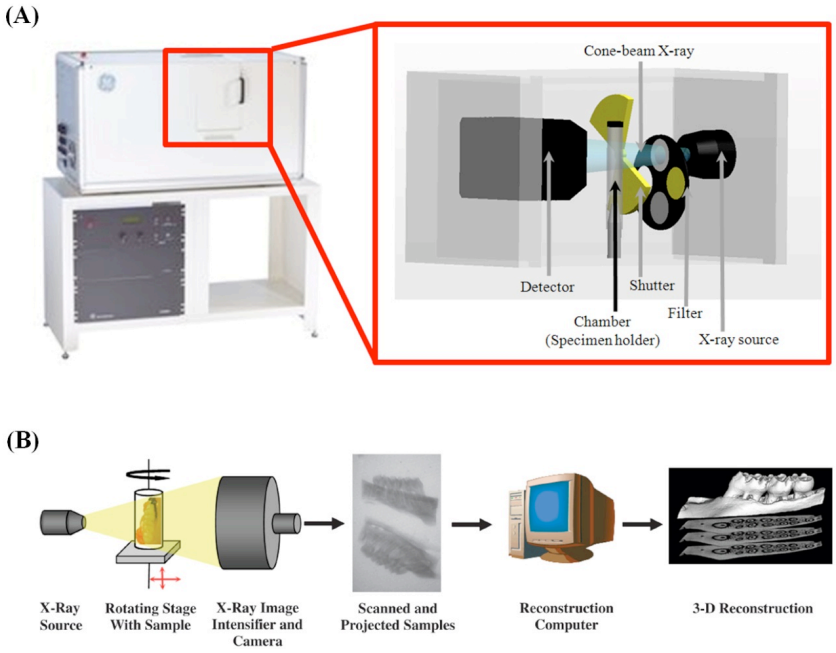

Figure 2.1 Schematic illustration of micro-computed tomography (micro-CT) and its scanning procedure. (A) Micro-CT composes a cone-beam x-ray source, filter with the shutter system, sample-holding chamber, and CCD camera and x-ray detector. **(B)** Cone-beam micro-CT for assessment of alveolar bone. Specimens are exposed to polychromatic x-rays on a rotating stage. X-rays that penetrate the mandible or maxilla pass through an image intensifier and are captured by a camera, producing 2-D slices of 18μm thickness. Finally, cross-sectional images are reconstructed into a 3-D structure by a host computer.

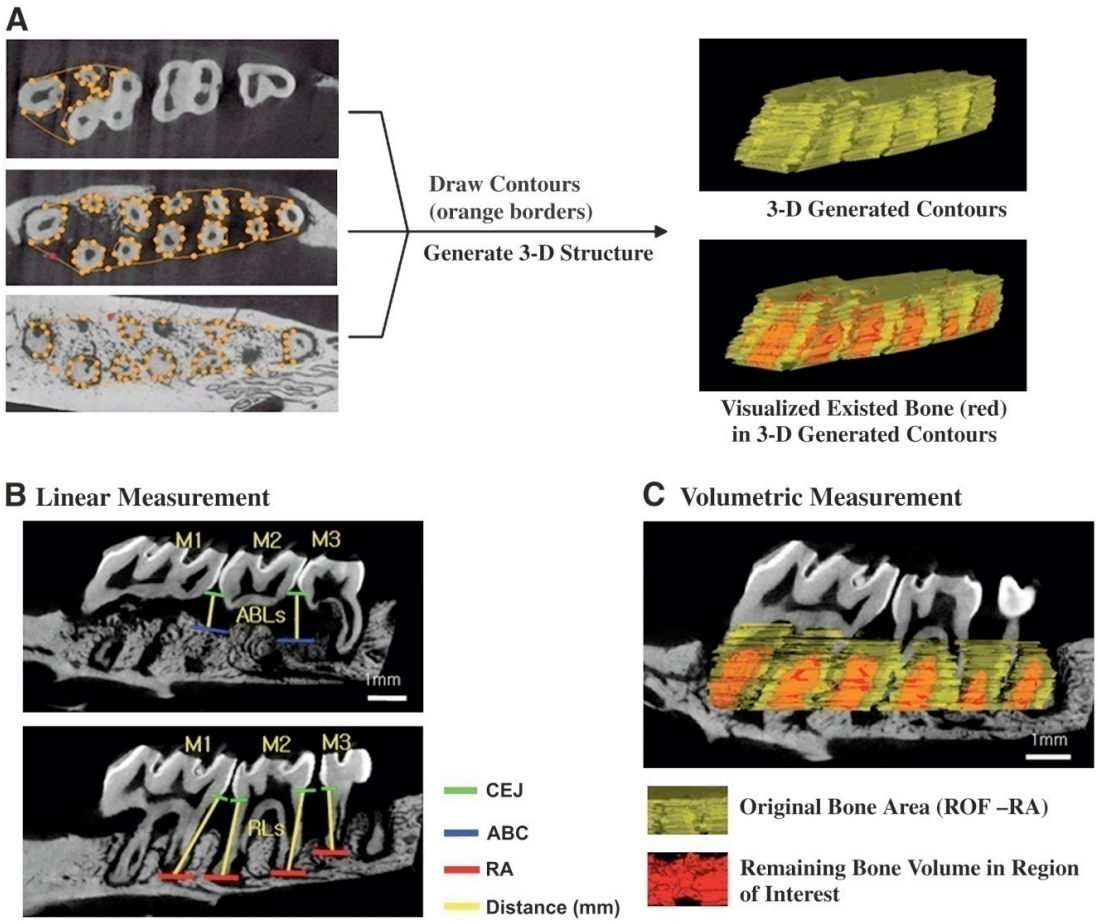

Figure 2.2 Method for creating 3-D ROIs used in analysis of alveolar bone. (A) 2-D contours are drawn at regular intervals from the ROFs to the RAs. Once all contours are drawn, a 3-D ROI is generated for reconstruction. **(B)** Linear measurements are made for alveolar bone loss (ABL) within the interdental space from the CEJ to ABC and RLs from the CEJ to RA (in millimeters). **(C)** Volumetric measurement using 3-D generated ROIs. Software assesses the quantity of bone and analyzes volumetric parameters within the volume of interest that are from 3-D generated contours.

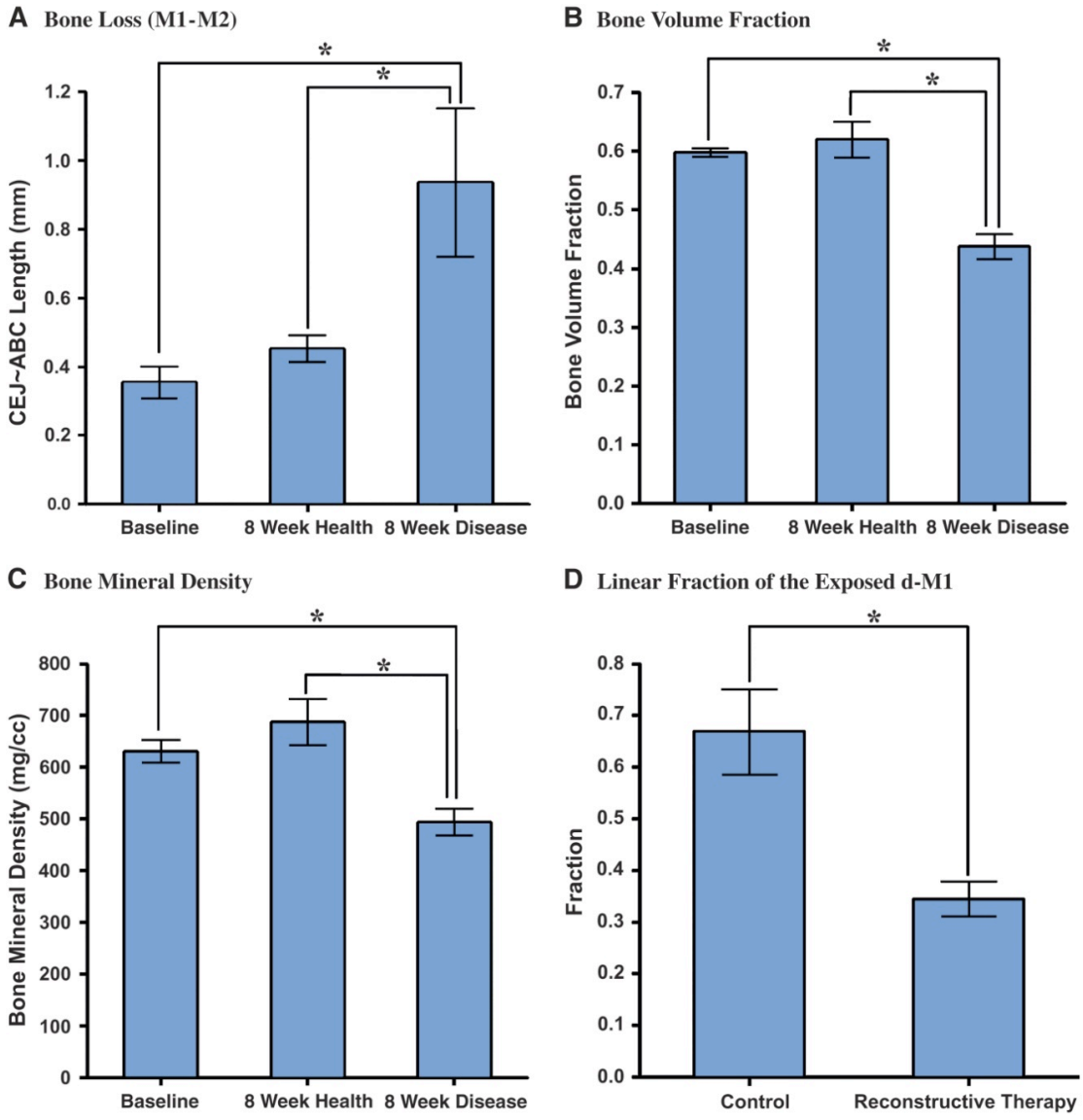

Figure 2.3 Linear measurements of interdental CEJ-ABC and volumetric measurement of ROF-RA. The analyses of linear measurements and volumetric measurements at baseline and among healthy and diseased groups. (A) Linear bone loss distances represented as CEJ-ABC length. Bone loss in the P.gingivalis LPS –induced periodontitis group with significant differences were observed between diseased and other tops in BVF (B) BMC (not shown), and BMD (C). (D) After reconstructive cell therapy, exposed defects at the distal root areas of M1 were measured linearly as a

proportion of the total RL. There was significant difference between non-transduced and transduced cell therapy groups. *$p<0.05$.

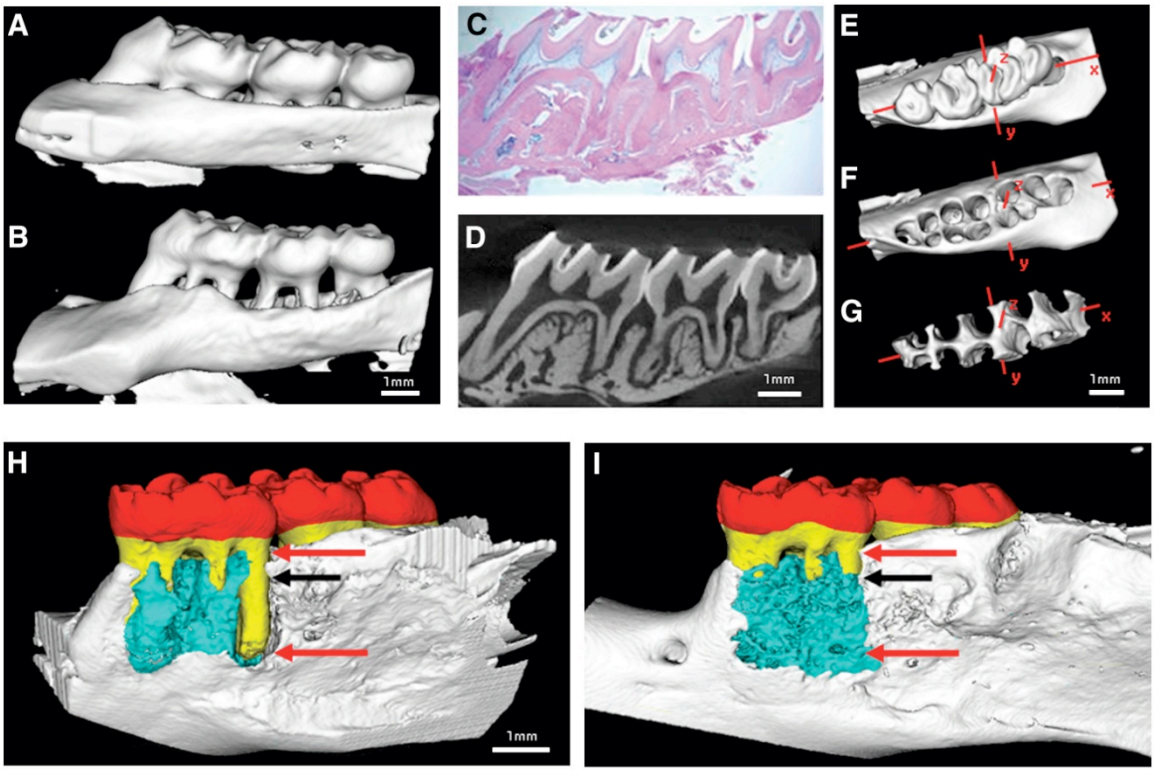

Figure 2.4 Representative specimens displaying bone loss in healthy (A) and diseased (B) periodontia. Cross-sectional histologic image with hematoxylin and eosin (H&E) staining **(C)** and the corresponding micro-CT slice **(D)** demonstrate similarity of sections. Three-dimensional isosurfaces in a Cartesian coordinate system display an extracted rat maxilla including all three molars **(E)**, rat maxilla with teeth extracted digitally **(F)**, and alveolar bone within a preselected ROI used in bone volume determination **(G)**. Surgically-induced dehiscence osseous defects in a mandibular defect biopsied at 5 weeks post-therapy. **(H)** Control group. **(I)** Reconstructive therapy group demonstrating bone repair over the previously dehisced lesion of the M1 distal root. Red = crown; yellow = tooth root; blue = regenerated bone; red arrows = standardized root fenestration osseous effects; black arrows = top side of the scaffold implanted site on the osseous defect.

2.7. TABLE

			95% Confidence Interval	
	Intraclass Correlation Coefficient (ICC)	Coefficient of Variation (CV; %)	Lower Boundary	Upper Boundary
Intra-examiner Calibration				
Examiner 1	0.999	1.2	0.937	1.000
Examiner 2	0.997	0.7	0.980	1.000
Inter-examiner Calibration	0.999	1.4	0.990	1.000

Table 2.1 Statistical results for reliability and reproducibility in developed methodology with intraclass correlation coefficient (ICC) and coefficient of variation (CV).

2.8. REFERENCES

1. Hamada Y, Kondoh T, Noguchi K, et al. Application of limited cone beam computed tomography to clinical assessment of alveolar bone grafting: A preliminary report. *Cleft Palate Craniofac J.* 2005;42:128–137.

2. Hausmann E. Radiographic and digital imaging in periodontal practice. *J Periodontol.* 2000;71:497–503.

3. Bernhardt R, van den Dolder J, Bierbaum S, et al. Osteoconductive modifications of Ti-implants in a goat defect model: Characterization of bone growth with SR muCT and histology. *Biomaterials.* 2005;26:3009–3019.

4. Rawlinson A, Elcock C, Cheung A, et al. An in-vitro and in-vivo methodology study of alveolar bone measurement using extra-oral radiographic alignment apparatus, Image Pro-Plus software and a subtraction programme. *J Dent.* 2005;33:781–788.

5. Van Oossterwyck H, Duyck J, Vander Sloten J, et al. Use of microfocus computerized tomography as a new technique for characterizing bone tissue around oral implants. *J Oral Implantol.* 2000;26:5–12.

6. Mengel R, Candir M, Shiratori K, Flores-de-Jacoby L. Digital volume tomography in the diagnosis of periodontal defects: An in vitro study on native pig and human mandibles. *J Periodontol.* 2005;76:665–673.

7. Rosenstein SW, Long RE, Jr, Dado DV, Vinson B, Alder ME. Comparison of 2-D calculations from periapical and occlusal radiographs versus 3-D calculations from CAT

scans in determining bone support for cleft-adjacent teeth following early alveolar bone grafts. *Cleft Palate Craniofac J.* 1997;34:199–205.

8. Feldkamp LA, Goldstein SA, Parfitt AM, Jesion G, Kleerekoper M. The direct examination of three-dimensional bone architecture in vitro by computed tomography. *J Bone Miner Res.* 1989;4:3–11.

9. Fanuscu MI, Chang TL. Three-dimensional morphometric analysis of human cadaver bone: Microstructural data from maxilla and mandible. *Clin Oral Implants Res.* 2004;15:213–218.

10. Wilensky A, Gabet Y, Yumoto H, Houri-Haddad Y, Shapira L. Three-dimensional quantification of alveolar bone loss in *Porphyromonas gingivalis*-infected mice using micro-computed tomography. *J Periodontol.* 2005;76:1282–1286.

11. Taba MJ, Huffer HH, Shelburne CE, et al. Gene delivery of TNFR:Fc by adeno-associated virus vector blocks progression of periodontitis. *Mol Ther.* 2005;11(Suppl 1):S262.

12. Jin Q, Anusaksathien O, Webb SA, Printz MA, Giannobile WV. Engineering of tooth-supporting structures by delivery of PDGF gene therapy vectors. *Mol Ther.* 2004;9:519–526.

13. Jin QM, Zhao M, Webb SA, et al. Cementum engineering with three-dimensional polymer scaffolds. *J Biomed Mater Res A.* 2003;67:54–60.

14. Zhu F, Sarkar S, Kaitwatcharachai C, et al. Methods and reproducibility of measurement of resistivity in the calf using regional bioimpedance analysis. *Blood Purif.* 2003;21:131–136.

15. Kohler T, Beyeler M, Webster D, Muller R. Compartmental bone morphometry in the mouse femur: Reproducibility and resolution dependence of microtomographic measurements. *Calcif Tissue Int.* 2005;77:281–290.

16. Reddy MS. Radiographic alveolar bone change as an outcome measure for therapies that inhibit bone loss or foster bone gain. *J Int Acad Periodontol.* 2005;7:175–188.

17. Misch KA, Yi ES, Sarment DP. Accuracy of cone beam computed tomography for periodontal defect measurements. *J Periodontol.* 2006;77:1261–1266.

18. Chen SK, Pan JH, Chen CM, Jeng JY. Accuracy of supported root ratio estimation from projected length and area using digital radiographs. *J Periodontol.* 2004;75:866–871.

19. Wolf B, von Bethlenfalvy E, Hassfeld S, Staehle HJ, Eickholz P. Reliability of assessing interproximal bone loss by digital radiography: Intrabony defects. *J Clin Periodontol.* 2001;28:869–878.

20. Sarment DP, Sukovic P, Clinthorne N. Accuracy of implant placement with a stereolithographic surgical guide. *Int J Oral Maxillofac Implants.* 2003;18:571–577.

21. Bianchi J, Fiorellini JP, Howell TH, et al. Measuring the efficacy of rhBMP-2 to regenerate bone: A radiographic study using a commercially available software program. *Int J Periodontics Restorative Dent.* 2004;24:579–587.

22. Sant'Anna EF, Gomez DF, Sumner DR, et al. Micro-computed tomography evaluation of the glenoid fossa and mandibular condyle bone after bilateral vertical ramus mandibular distraction in a canine model. *J Craniofac Surg.* 2006;17:111–119.

23. Luo G, Kinney JH, Kaufman JJ, et al. Relationship between plain radiographic patterns and three-dimensional trabecular architecture in the human calcaneus. *Osteoporos Int.* 1999;9:339–345.

24. Hirabayashi S, Umamoto N, Tachi M, et al. Optimized 3-D CT scan protocol for longitudinal morphological estimation in craniofacial surgery. *J Craniofac Surg.* 2001;12:136–140.

25. Postnov AA, Vinogradov AV, Van Dyck D, Saveliev SV, De Clerck NM. Quantitative analysis of bone mineral content by x-ray microtomography. *Physiol Meas.* 2003;24:165–178.

26. Gauthier O, Muller R, von Stechow D, et al. In vivo bone regeneration with injectable calcium phosphate biomaterial: A three-dimensional micro-computed tomographic, biomechanical and SEM study. *Biomaterials.* 2005;26:5444–5453.

27. Johnson AJW, Wojtowicz AM, Dellinger JG, et al. 3D tissue distribution patterns characterized by micro-CT. *Mat Res Soc Symp Proc.* 2004;EXS-1:F5.18.11–F15.18.13.

28. Yang J, Pham SM, Crabbe DL. Effects of oestrogen deficiency on rat mandibular and tibial microarchitecture. *Dentomaxillofac Radiol.* 2003;32:247–251.

29. Jones AC, Sakellariou A, Limaye A, et al. Investigation of microstructural features in regenerating bone using micro computed tomography. *J Mater Sci Mater Med.* 2004;15:529–532.

CHAPTER THREE

AAV2/1-TNFR:Fc GENE DELIVERY PREVENTS PERIODONTAL DISEASE PROGRESSION

Cirelli JA, **Park CH**, MacKool K, Taba Jr. M, Lustig KH, Burstein H, Giannobile WV.

Gene Therapy, **2009** 16(3): 426-436

3.1. ABSTRACT

Periodontal disease is a chronic inflammatory condition induced by oral microbial biofilms that induce a host immune response. Control of progressive tissue destruction in high-risk patients is a significant challenge in clinical therapy. Soluble protein delivery of antagonists to tumor necrosis factor-alpha (TNF-α) inhibits alveolar bone resorption due to periodontitis. However, protein therapy raises several concerns, such as recurrence of disease activity after treatment cessation requiring repeated dosing regimens. In this study, we used pseudotyped adeno-associated virus vector based on serotype 1 (AAV2/1) to deliver the TNF receptor-immunoglobulin Fc (TNFR:Fc) fusion gene to rats subjected to experimental *Porphyromonas gingivalis* (*Pg*)-lipopolysaccharide (LPS)-mediated bone loss. Animals received intramuscular delivery of pseudotyped AAV2/1-TNFR:Fc vector (1×10^{11} DNase I-resistant particles) and either Pg-LPS delivered to the gingivae thrice

weekly for 8 weeks or vehicle alone, AAV2/1-TNFR:Fc therapy led to a sustained therapeutic level of serum TNFR protein and protected against Pg-LPS-mediated loss of bone volume and bone density. Furthermore, AAV2/1-TNFR:Fc administration reduced local levels of multiple proinflammatory cytokines and osteoclast-like cells at the periodontal lesion sites. These findings suggest that delivery of AAV2/1-TNFR:Fc may be a viable approach to modulate periodontal disease progression.

3.2. INTRODUCTION

Periodontitis is a common oral inflammatory disease that in severe cases, is the leading cause of tooth loss in adults. Periodontal disease has also been associated with increased risk of systemic diseases, such as coronary heart disease, bacterial pneumonia and stroke [1,2]. Although triggered by bacterial biofilms on the tooth surface, tissue destruction and disease progression are driven primarily by mediators of the host immune-inflammatory response to persistent gram-negative pathogens [1]. Activation of pathogen recognition receptors (e.g. toll-like receptors - TLRs) by bacterial LPS and other pathogen-associated molecular patterns (PAMPs) stimulate the production of pro-inflammatory cytokines (Interleukin-1 (IL-1), IL-6 and tumor necrosis factor (TNF-α) and chemokines (IL-8) followed by a cascade of immune-inflammatory events [3]. Thus, therapeutic approaches that target the host response to local oral infection offer significant potential for periodontal disease management [4, 5].

TNF-α is a multifunctional cytokine that plays a crucial role in the pathogenesis of periodontitis [6]. TNF-α is released by activated monocytes, macrophages and T lymphocytes and contributes to both innate and adaptive immune responses, regulating growth, differentiation, survival and physiological function of a variety of different cells and further production of other cytokines, inflammatory mediators and enzymes [6-10]. TNF-α is a potent bone resorption inducer that stimulates osteoclast differentiation and activation [7, 11, 12]. TNF-α's functions are mediated by two receptors, p55 and p75 TNF receptor (TNFR), which, respectively, up-regulate and dampen inflammation [13,

14]. P75 TNFR knockout mice display defects in osteoclastogenesis and inflammation-mediated periodontal tissue destruction [15, 16].

Host-modulation therapies using TNF-α blockers have been successfully used in humans for the treatment of rheumatoid arthritis (RA) [17-19]. One class of drugs consists of monoclonal anti-TNF-α antibodies or fusion proteins containing p75 TNFR linked to the Fc portion of human IgG1. In both cases, the drug binds to TNF-α with high affinity and prevents it from interacting with its cognate cell surface receptors [20]. TNF-α blockers significantly improve clinical outcome by reducing erosive bone damage [21], through inhibition of the receptor activator of nuclear factor kappa B ligand (RANKL) expression in the synovial tissue [22]. In periodontitis management, protein delivery of antagonists to IL-1β and TNF-α lead to reduction in periodontal tissue destruction *in vivo [23-27]*. However, the use of recombinant protein raises several concerns, such as recurrence of disease activity after cessation of therapy and repeated dosing regimens [28]. Recently, delivery of an adeno-associated virus (AAV) vector encoding the p75-TNFR:Fc fusion gene has been evaluated as an alternative approach for TNF-α blockade in animal models of RA and demonstrated long-term disease suppression [29, 30]. The main advantages of gene therapy are maintenance of sustained and therapeutically relevant concentration of the protein [29], eliminating the previously described limitations of recombinant protein delivery.

In this study, AAV2/1-TNFR:Fc was delivered for the prevention of periodontal disease induced by local, chronic, oral exposure of *Porphyromonas gingivalis* lipopolysaccharide

(*Pg*-LPS) *in vivo*. The results of this study show that AAV2/1-TNFR:Fc led to potent inhibition of periodontal disease progression.

3.3. MATERIALS AND METHODS

3.3.1. Plasmids/Vector production and purification

Recombinant AAV2 vectors were produced by a standard calcium phosphate transfection method in adherent human 293 cells, using the Ad helper, trans-packaging, and AAV vector plasmids as described previously [49]. Vector titers were determined by real-time PCR, using a Perkin-Elmer Applied Biosystems Prism 7900 sequence detector (Foster City, CA), and were between 5 and 20×10^{12} DRP/mL. Vector infectivity was assessed in a TCID50 assay using the HeLa-based B50 cell line [50].

3.3.2. Porphyromonas gingivalis lipopolysaccharide (*Pg*-LPS)

Pg-LPS was isolated from *P. gingivalis* strain W83, following a previously described protocol [51]. Briefly, *Pg* strain W83 was cultured in an anaerobic chamber with modified Brucella-Broth medium. After growth, bacteria were centrifuged at 5,000 rpm for 30 min, resuspended in sterile water for washing and the final pellet was sequentially treated with lysozyme, DNAse, RNAse and proteases to extract and purify the lipopolysaccharide [51].

3.3.3. Animal model of Pg-LPS-induced periodontal disease

A total of 45 adult male Sprague-Dawley rats (approximated weight 200 g, 8-10 weeks), were purchased from Charles River Laboratories (Wilmington, MA). All animal experimental procedures were approved by the University of Michigan Committee on the Use and Care of Animals. Animals were allowed to acclimate for seven days before experimentation and were given water and chow *ad libitum*. For all the procedures,

animals were anesthetized with isoflurane (5% with O_2 for induction and 3% maintenance) (Baxter Healthcare Corp., Deerfield, IL). Experimental periodontal disease induction was performed by administering 10 μL of *Pg*-LPS (1.0 mg/mL) into four palatal gingival tissue sites (total of 40 μL/animal) at the base of the interproximal gingival papillae between maxillary molars bilaterally as previously described [52]. The injections were performed three times weekly using custom-designed 0.375 in × 33 ga, 30° bevel needles attached to a 50 μL Hamilton syringe (Hamilton Company, Reno, NV). Disease induction was performed in two groups of animals (n=10/group): diseased group (*Pg*-LPS group) and treatment group (AAV2/1-TNFR:Fc + *Pg*-LPS group). *Pg*-LPS administrations were performed from baseline to sacrifice, for four or eight weeks after the first injection (n=5/group/timepoint).

3.3.4. Administration of AAV2/1-TNFR:Fc vector

After anesthesia, the skin overlying the quadriceps muscle areas was exposed by shaving and disinfection. A single dosage of rAAV2/1-TNFR:Fc viral vector (100 μl of 1×10^{11} DRP/animal) was delivered im, equally divided to both quadriceps (50 μl in each muscle), four weeks before *Pg*-LPS disease induction. AAV2/1-TNFR:Fc was administered via Hamilton syringes and the animals were placed in a recovery cage and observed for normal ambulation. Two groups of animals received vector therapy (n=5/group/timepoint): AAV2/1-TNFR:Fc only or AAV2/1-TNFR:Fc + *Pg*-LPS groups. The vehicle controls were treated as above with formulation buffer containing 20 mM Tris pH 8, 200 mM NaCl, 2 mM MgCl in 1% glycerol.

3.3.5. Short-term experiment

Based on the cytokine expression results for TNFα and IL1β found in this study, a short-term experiment was performed subsequently to evaluate the early cytokine response to a single injection of *Pg*-LPS in the palatal gingival tissue. A total of 52 rats were divided into three groups: Vehicle, *Pg*-LPS, or AAV2/1-TNFR:Fc + *Pg*-LPS. The rats received the same treatment described for animals within the main experiment, except for *Pg*-LPS administration, which consisted of a single injection. Subgroups of animals (n= 4/group/timepoint) were sacrificed at baseline, 12, 24, 48 and 72 h after *Pg*-LPS injection and TNFα and IL1β cytokine expression was evaluated by real-time PCR as described below.

3.3.6. ELISA TNFR serum level determination

Serum was obtained from blood samples collected by tail bleeding at -4 weeks (pre-baseline), 0 (baseline, disease induction), 4 and 8 weeks. Serum TNFR levels were determined by ELISA. Briefly, 96-well plates were coated with a goat anti-murine TNF receptor II antibody (R&D Systems, Minneapolis, MN) overnight at 4°C. Plates were washed 3x with phosphate-buffered saline supplemented with 0.05% Tween-20 (Fisher, Houston, TX), and blocked with 1% bovine serum albumin (Sigma, St Louis, MO) for 3 h at RT on an orbital shaker. After washing, the plates were incubated with serum samples for 1 h at RT on a shaker plate. Following sample incubation, the wells were washed, and incubated with a biotin-conjugated mouse anti-rat immunoglobulin G1 antibody (PharMingen/BD Biosciences, San Jose, CA) for 1 h, washed and then incubated with streptavidin-horseradish peroxidase (Zymed, San Francisco, CA) for 30

min at RT. The presence of rat TNFR:Fc protein was detected using the tetramethylbenzidine (TMB) colorimetric substrate (Pierce, Rockford, IL) and stopped with 1 M sulfuric acid (Sigma, St Louis, MO). Quantitation of rat TNFR:Fc protein was based on OD 450 values (Multiskan Ascent, Thermo Fisher Scientific Inc., Waltham, MA) compared with a standard curve of purified rat TNFR:Fc protein. The limit of detection of the assay was 0.219 ng/mL.

3.3.7. Histological analysis of the inflammatory cell infiltrates

Rats were sacrificed in a CO_2 chamber at designated timepoints. Hemi-maxillae were harvested and fixed for 48 h in 10% neutral-buffered formalin and transferred to 70% ethanol for μCT scanning. Samples were subsequently decalcified with 10% ethylenediaminetetraacetic acid disodium salt (EDTA) for 3 weeks, embedded in paraffin, and cut into 4- to 5 μm-thick serial sections. Transverse sections of the maxillary 2nd molar teeth parallel to the long axis were stained with H&E for stereometric analysis by a masked, calibrated examiner. The presence of inflammatory cell infiltrate and tissue destruction was evaluated in the periodontal region. A point-counting technique was used to evaluate the proportion of the following structures: fibroblastic cells, collagen, vascular structures and inflammatory cells on the H/E-stained sections. Two areas were assessed individually in comparison to the experimental groups: a submarginal area, representing the connective tissue subjacent to the gingival sulcus (apical border of junctional epithelium and tooth structure as the coronal and medial limits, respectively); and a bone crest region, representing the connective tissue in adjacent to the bone crest (coronal portion of the bone crest and tooth structure as apical and medial limits,

respectively). A 500 μm^2 rectangular-lattice grid with 50 intersection points was constructed using image software and the type of structure found on the intersection of the grid lines was counted on an optical microscope (Diastar-Cambridge Instruments) under 200X magnification.

3.3.8. Microcomputed Tomography scanning and bone loss analysis

Microcomputed tomography provides high qualification and accurate quantification of the mineralized tissues such as alveolar bone and teeth [52]. Each maxillary specimen was scanned and reconstructed at 18μm^3 voxels using a μCT system (GE Healthcare, London, ON, Canada). A 3-D volume viewer and analyzer software (Microview Analysis+ v.2.1.2 software, GE Healthcare) was used as the tool for both 3-D and 2-D visualization and quantification as previously described [52]. In brief, linear bone loss was measured as the distance from the cementoenamel junction (CEJ) to the alveolar bone crest or to the base of the alveolar intrabony defect at the palatal surface of the mesio- and disto-palatal roots of the maxillary second molar teeth. For the volumetric analysis, the roof of the furcation and the root apex of the 2nd maxillary molars, the mesial roots of the 3rd molars and the distal roots of the 1st molars were used as reproducible landmarks for estimation of alveolar bone loss. 2-D ROIs were drawn at regular intervals, (average 8 data slices) on a coronal view and reconstructed as a 3-D structure in order to quantify volumetric parameters, bone volume fraction (BVF), and bone mineral density (BMD) (mg/cc). The measurements of coded specimens were made by two independent, calibrated examiners.

3.3.9. Real time PCR for detection of pro-inflammatory cytokines and bone resorption related molecules

Total RNA was extracted from gingival tissue biopsies harvested from a standardized region of the palatal region of the maxillary molar teeth, comprising an ~5 × 2 mm rectangular area from the medial of the first molar to the distal of the third molar extending from the gingival margin to the palatine suture. RNeasy Mini Kit (Qiagen, Valencia, CA) complemented with RNase-Free DNase Set (Qiagen) for RNA purification were used following the protocols recommended by the manufacturer. After determining RNA concentration and purity by spectrophotometry, complementary DNA (cDNA) was synthesized using 1μg of RNA by a reverse transcription reaction (TaqMan Reverse Transcription Reagents, Applied Biosystems, Foster City, CA). Real time quantitative PCR was performed in an ABI Prism 7500 Real Time PCR System using TaqMan Gene Expression Assays (Applied Biosystems). For each reaction (30 μL), 1 μL of cDNA was added to 1.5 μL of specific TaqMan Gene Expression Assay, 15 μL of TaqMan 2x PCR MasterMix (Applied Biosystems) and 12.5 μL of RNase/DNase free water. The PCR conditions were 50°C (2 min), 95°C (10 min), followed by 40 cycles of 95°C (15 sec) and 6 0°C (1 min) and by the standard denaturation curve. The target gene, ABI ID # and reporter probe sequence of each specific TaqMan Gene Expression Assay were: glyceraldehyde-3-phosphate dehydrogenase (GAPDH), ID Rn99999916_s1, CGGGAAACCCATCACCATCTTCCAG; interleukin-1 beta, ID Rn00580432_m1, CATAAGCCAACAAGTGGTATTCTCC; tumor necrosis factor alpha, ID Rn99999017_m1, CACACTCAGATCATCTTCTCAAAAC; interleukin-6, ID Rn00561420_m1, GAGAAAAGAGTTGTGCAATGGCAAT; interleumin-10, ID

Rn00563409_m1, osteoprotegerin, ID Rn00563499_m1, GCTGTGCACTCCTGGTGTTCTTGGA; Receptor Activator of Nuclear Factor-Kappa B Ligand (RANKL), IDRn00589289_m1, TGCCGACATCCCATCGGGTTCCCAT.

3.3.10. Immunohistochemistry of TRAP following gene delivery

Serial sections of the maxillary second molar teeth were prepared as previously described and immunostained for TRAP detection. Deparaffinized tissue sections were pretreated in antigen retrieval buffer (Dako; Glostrup, Denmark) in a pressure chamber (Biocare Medical; Concord, CA) for 20 min. and cooled at RT. ABC Staining System (sc-2023, Santa Cruz Biotechnology, Inc., Santa Cruz, CA) was used following the manufacturer's instructions. Primary antibody was raised in goat and consisted of: TRAP (K17): sc-30833 (4 μg/mL, Santa Cruz Biotechnology, Inc). Control sections were incubated with normal IgG (R&D Systems) pre-immunoserum in the same concentrations to assess background staining. All sections were counterstained with Hematoxylin Gill's Formulation #1 (Fisher Scientific).

Osteoclast enumeration was based on the presence of TRAP-positive multinucleated cells, adjacent to the alveolar bone surface in a pit area. Photomicrographs of the most coronal 1 mm of the palatal bone crest were analyzed by a masked, calibrated examiner and the number of osteoclast-like cells on the palatal bone plate surface were enumerated and in response to *Pg*-LPS administration.

3.3.11. Statistical analysis

Statistical analysis was performed using GraphPad Prism software. Data were pooled by experimental group and the mean ± SD were calculated. One-way ANOVA followed by Tukey's *post hoc* test were performed to determine the presence of any significant difference between groups for serum TNFR:Fc levels, linear bone loss and cytokine expression. P-values less than 0.05 were considered statistically significant.

3.4. RESULTS

3.4.1. Single administration of AAV2/1-TNFR:Fc results in sustained serum rat TNFR:Fc protein levels

The circulating serum levels of rat TNFR:Fc protein were monitored by enzyme linked immunosorbent assay (ELISA) during the study period to confirm the transduction efficiency of AAV2/1-TNFR:Fc after a single IM administration of 10^{11} DNase-resistant particles (DRP). The injections were performed four weeks prior to the *Pg*-LPS delivery to allow for therapeutic levels at the time of disease induction. The administrations resulted in mean TNFR serum levels of 8.2±1.8 μg/mL, by 4 weeks (time of disease induction). These levels were sustained during the 8 week experimental period (Fig. 3.6). In the other groups not treated with the AAV2/1-TNFR:Fc, including *Pg*-LPS, Vehicle only (Veh) or no treatment group (NT), TNFR:Fc serum levels were significantly lower than AAV2/1-TNFR:Fc treated animals with results at or below the detection level. The result is in agreement with a previous report, which demonstrated a long-term and sustained secretion of TNFR after a single IM injection of AAV2/1-TNFR:Fc [30].

3.4.2. AAV2/1-TNFR:Fc inhibits local inflammatory cell infiltrates induced by Pg-LPS in vivo

Animals were sacrificed at four and eight weeks after *Pg*-LPS disease induction. Stereometric histological analysis using hematoxylin and eosin (H/E) staining was performed to evaluate the inflammatory cell infiltrate induced by an 8-week course of local *Pg*-LPS administration with or without IM AAV2/1-TNFR:Fc gene therapy. At both timepoints, an intense inflammatory cell infiltrate was consistently observed in the

subepithelial connective tissue and surrounding alveolar bone of the periodontia of *Pg*-LPS-treated animals (Fig. 3.1b, e). In contrast, a significantly less intense inflammatory reaction was observed in the AAV2/1-TNFR:Fc + *Pg*-LPS-treated animal (Fig. 3.1c, f). Control animals (Veh, NT and vector only) did not display evidence of significant inflammatory cell infiltrates (Fig. 3.1a, d). Statistical analysis demonstrated higher number of inflammatory cells for diseased group (*Pg*-LPS) in both analyzed areas at 4 weeks timepoint and in subepithelial area at 8 weeks timepoint when compared to treated animals (AAV2/1-TNFR:Fc + *Pg*-LPS) (Fig. 3.1). These results demonstrate the anti-inflammatory effect of TNFR:Fc in the face of continued *Pg*-LPS challenge.

3.4.3. AAV2/1-TNFR:Fc prevents alveolar bone loss and preserves bone mineral density in Pg-LPS exposed animals

To investigate the preventive effect of AAV2/1-TNFR:Fc on alveolar bone loss induced by an 8-week course *Pg*-LPS delivery, bi-dimensional (2-D) and three-dimensional (3-D) microcomputed tomography (μCT) images of maxillae and associated teeth were evaluated by linear and volumetric measurements. Linear bone loss was measured from the cementum enamel junction (CEJ) to the bone crest (BC) at the palatal surface of the maxillary second molar teeth, which were the sites most directly affected by *Pg*-LPS local delivery. Significant alveolar bone destruction was observed in the *Pg*-LPS group continuously over the course of eight weeks, demonstrating a progressive loss of tooth-supporting bone (Fig. 3.2, *Pg*-LPS).Administration of the AAV2/1-TNFR:Fc vector prevented linear bone resorption during the entire study observation period, represented

by significant preservation of tooth-supporting bone during *Pg*-LPS challenge, at both timepoints (Fig. 3-A.2, AAV2/1-TNFR:Fc + *Pg*-LPS).

This preservation corresponded, on average, to 61.2% and 48.5% of bone loss reduction at 4 and 8 week timepoints, respectively, compared with the *Pg*-LPS only-treated group that was normalized to Veh-treated animals. Interestingly, a single administration of AAV2/1-TNFR:Fc vector to a group of healthy animals also resulted in preservation of alveolar bone level compared with the vehicle. This bone-sparing effect was significantly greater than that of the vehicle-treated healthy controls, demonstrating a preventive effect in the normal physiologic alveolar bone loss observed in rats (Fig. 3.2). These results clearly show the beneficial effect of the TNF-α blockade on alveolar bone preservation.

Volumetric bone loss was measured in a specific region of interest (ROI) captured from the 3-D images, based on fixed reference points. ROI involved furcation and interproximal alveolar bone around the maxillary second molars and detected the extension of the destructive effect of local *Pg*-LPS delivery. The results were comparable to linear measurements, showing more severe bone loss around molar teeth of the *Pg*-LPS group and a preventive effect for the AAV2/1-TNFR:Fc vector-treated groups. This response was more pronounced after longer periods of disease progression (8 weeks) (Table 3.1). Bone mineral density measures also demonstrated that the AAV2/1-TNFR:Fc vector preserved bone quality in *Pg*-LPS exposed animals, after longer periods of disease induction. Vector alone-treated animals displayed bone density values similar

to that observed in healthy animals and superior to diseased *Pg*-LPS treated animals (Table 3.1).

Taken together, these results strongly suggest that anti-inflammatory TNFα-blocking therapy prevents disease-induced bone loss and preserves bone density in the periodontium.

3.4.4. AAV2/1-TNFR:Fc suppresses inflammatory and bone resorptive cytokine expression in periodontal tissues exposed to Pg-LPS

To better understand the mechanisms by which TNF-α blockade, in AAV2/1-TNFR:Fc-treated animals, suppress the progression of *Pg*-LPS-mediated tissue destruction, the expression of relevant inflammatory cytokines (IL-1 β, TNF-α, IL-6, IL-10) and bone-related molecules [receptor activator of nuclear factor kB ligand (RANKL) and osteoprotegerin (OPG)] involved in periodontal disease progression were evaluated in the gingival tissues, at the RNA level by real-time PCR. Significantly higher RNA expression of IL-6, IL-10, RANKL and OPG was observed at four weeks in *Pg*-LPS-exposed animals, but not in animals previously treated with the AAV2/1-TNRF:Fc vector (Fig. 3.3), suggesting an inhibition of the *Pg*-LPS-mediated inflammatory and bone destructive effects. IL-1β and TNF-α expression levels were not affected by continuous *Pg*-LPS administration and were similar for all the groups at four and eight weeks. These results corroborate previous *in vitro* [31] and *in vivo* [16] studies showing that long term, repeated administration of *Pg*-LPS induces cytokine tolerance to *Pg*-LPS. Based on these observations, a time course experiment was performed to determine IL-1β and TNF-α

gene expression over a short interval (12-72h). This parallel study demonstrated significant up-regulation of IL-1β and TNF-α expression, 24 to 48h after a single injection of *Pg*-LPS when compared to NT or vehicle injected animals (Fig. 3.4). Animals previously treated with AAV2/1-TNFR:Fc presented higher expression of both cytokines than NT or vehicle-injected animals, yet significantly lower than *Pg*-LPS only animals. Taken together, these results suggest that AAV2/1-TNFR:Fc gene therapy has an inhibitory effect on inflammatory and bone resorptive cytokines such as IL-1 and TNF during the short-term and to a lesser degree long-term.

3.4.5. AAV2/1-TNFR:Fc IM administration reduces TRAP+ osteoclasts-like cells associated with the alveolar crest in Pg-LPS-treated animals

To evaluate the effect of AAV2/1-TNFR:Fc administration on osteoclast differentiation at the alveolar crest in *Pg*-LPS-treated animals, histological sections were immunostained and osteoclast-like cells enumerated by image analysis for tartrate-resistant acid phosphatase (TRAP), an enzyme highly expressed in osteoclasts and activated macrophages. *Pg*-LPS-treated animals displayed significantly higher numbers of TRAP+ osteoclasts-like cells on the palatal bone surface compared with all other groups (Fig. 3.5). Administration of AAV2/1-TNFR:Fc vector reduced osteoclast number in animals challenged with *Pg*-LPS yielding results statistically similar to the other control groups. The same results were observed when the linear cumulative distance of the palatal bone surface in contact with multinucleated osteoclast-like cells was measured in the coronal 1 mm of the bone crest. From these results we conclude that AAV2/1-TNFR:Fc gene

therapy reduces active osteoclast presence at the alveolar bone crest level and, consequently, prevents alveolar bone resorption.

3.5. DISCUSSION

Host modulation therapies are rising as promising alternatives for the treatment of periodontal diseases [4]. These new strategies are based on advances in the knowledge of periodontal disease pathogenesis, which indicates the host response against pathogenic bacteria as the major driver of periodontal tissue destruction. However, similar to other chronic diseases, periodontal disease management require long-term treatment that can be affected by patient compliance. In developed countries, the level of adherence to long-term treatment of chronic diseases is 50%, and the problem is significantly worse in developing countries [32], suggesting the necessity of new therapies to overcome this problem. In this study, we evaluated the application of gene therapy technology, using an AAV vector encoding the TNFR:Fc transgene for modulation of the host immune-inflammatory response in periodontal disease. This new approach has been successfully evaluated for the treatment of other chronic diseases, such as neurological, cardiovascular and autoimmune diseases [33]. The AAV2/1-TNFR:Fc vector used in the present study led to high level transduction efficiency, prolonged gene expression and therapeutic efficacy in a RA model, encouraging this new application [29, 30]. Both periodontal disease and RA are chronic inflammatory diseases with complex etiology and clinically characterized by sustained over-expression of pro-inflammatory cytokines culminating in progressive bone destruction [34]. In this study, AAV2/1-TNFR:Fc administration resulted in a significant prevention of experimental periodontal disease progression, illustrating another approach for blocking cytokine production, one driven by pathogenic LPS.

The results of this study found that gene delivery achieved systemically therapeutic circulating levels of soluble TNFR protein, which were maintained during the entire observation period, consistent with our previous studies in RA [30]. To investigate the potential efficacy of a single delivery of AAV2/1-TNFR:Fc in prevention of alveolar bone loss and inflammation, we used a *Pg*-LPS-induced experimental periodontal bone resorption model. This model has the advantage to simulate the complex disease process occurring in human periodontitis. *Pg*-LPS was extracted from a highly pathogenic strain of *Porphyromonas gingivalis*, W-83, which is an important putative periodontal pathogen [35]. This bacterium stimulates the destructive innate host response through releasing high level LPS containing vesicles into the periodontal tissues. *Pg*-LPS is recognized by host cells transmembrane receptors TLR-2 and TLR-4 that activate key intracellular pathways (e.g., mitogen-activated protein kinases) and, thereafter, target genes involved in the activation of the host defense, especially pro-inflammatory cytokine production [36]. In this study, the *Pg*-LPS-induced disease model stimulated expression of key inflammatory and bone-related cytokines, detected at the mRNA level by real time PCR at short timepoints, 24-48h after single *Pg*-LPS administration (TNF-α and IL-1), or at longer intervals, 4 weeks after multiple *Pg*-LPS injections (IL-6, IL-10, RANKL and OPG). The time course experiment demonstrated an initial stimulatory effect of *Pg*-LPS on TNF-α and IL-1 expression, not observed after multiple *Pg*-LPS administration, suggesting an endotoxin tolerance process. TLRs and pro-inflammatory cytokines may become tolerised as a mechanism used in the oral mucosa to attempt to regulate local immune response [31, 37]. In addition, IL-10, an anti-inflammatory cytokine that was highly expressed in *Pg*-LPS challenged animals, also appears to participate in the

tolerance process by mediating immunosuppression and affecting production of pro-inflammatory cytokines [38]. In a previous study, cytokines showed dissimilar susceptibility to LPS challenge, consistent with our findings that TNF and IL-1 generated greater tolerance than other cytokines (e.g., IL-6) after LPS challenge [31]. TNF-α and IL-1 have been shown to be key molecules that contribute to several events essential for the initiation of an inflammatory response and, ultimately, tissue destruction [39]. They can also induce expression of other cytokines that amplify or sustain the inflammatory response and bone resorption as IL-6 and RANKL [40]. RANKL has been demonstrated to be increased during active periodontal disease in both soft and hard tissues [16, 53, 54]. We believe that, in this study, TNF-α and IL-1, followed by IL-6, RANKL and other pro-inflammatory molecules, trigger a cascade of progressive bone destruction that persists during the experimental period, suggesting a similar mechanism of action to what is observed in natural disease. The observed up-regulation of IL-10 and OPG expression after *Pg*-LPS challenge is in parallel with previous studies that demonstrate a stimulatory effect of LPS on the expression of cytokines in gingival [41, 42] and periodontal ligament fibroblasts [43]. As mammalian cells are challenged by polymicrobial infection, they appear to display a defensive mechanism against tissue destruction elicited by bacterial challenge, once IL-10 and OPG stimulate anti-inflammatory and osteoclastogenesis inhibitory effects.

Pg-LPS challenged animals that were previously treated with AAV2/1-TNFR:Fc vector presented reduced inflammatory infiltrates in the palatal gingival tissue parallel to an inhibition of the expression of inflammatory cytokines and bone resorptive-related

molecules (Figs. 3.1, 4-5), which resulted in significantly less alveolar bone loss when compared with *Pg*-LPS treated animals (Fig. 3.2). Taken together, these results support the central role of TNF-α on the TLR-mediated immune-inflammatory cascade of events responsible for the tissue destruction in the chronic periodontal disease. More specifically, TNF-α stimulates the expression of chemoattractants and their receptors for inflammatory cells, OPG and RANKL by periodontal ligament fibroblasts, T and B lymphocytes, and osteoblastic/stromal cells [10, 16, 43, 45, 46]. TNF-α also has direct effects on osteoclast differentiation independent of the RANK-RANKL axis [11, 12].

To better investigate the AAV2/1-TNFR:Fc therapeutic effect on the alveolar bone resorption induced by *Pg*-LPS, we evaluated the presence of osteoclast-like cells at the bone crest surface and the expression of OPG and RANKL, which are key molecules in osteoclastic differentiation and activation [47]. In parallel with inhibition of cytokine expression, AAV2/1-TNFR:Fc-treated animals demonstrated lower levels of RANKL and OPG expression in the gingival tissue, confirming the association of TNFα and other pro-inflammatory cytokines on osteoclast differentiation/activation and subsequent bone loss [47, 48].

In summary, delivery of an AAV2/1-TNFR:Fc gene therapy vector suppresses experimental periodontal disease progression through key cytokine and bone-related molecule modulation, reminiscent to the effects observed in RA. AAV2/1-TNFR:Fc is a promising host modulation approach for use in periodontal disease co-management with anti-infective therapy.

3.6. FIGURES

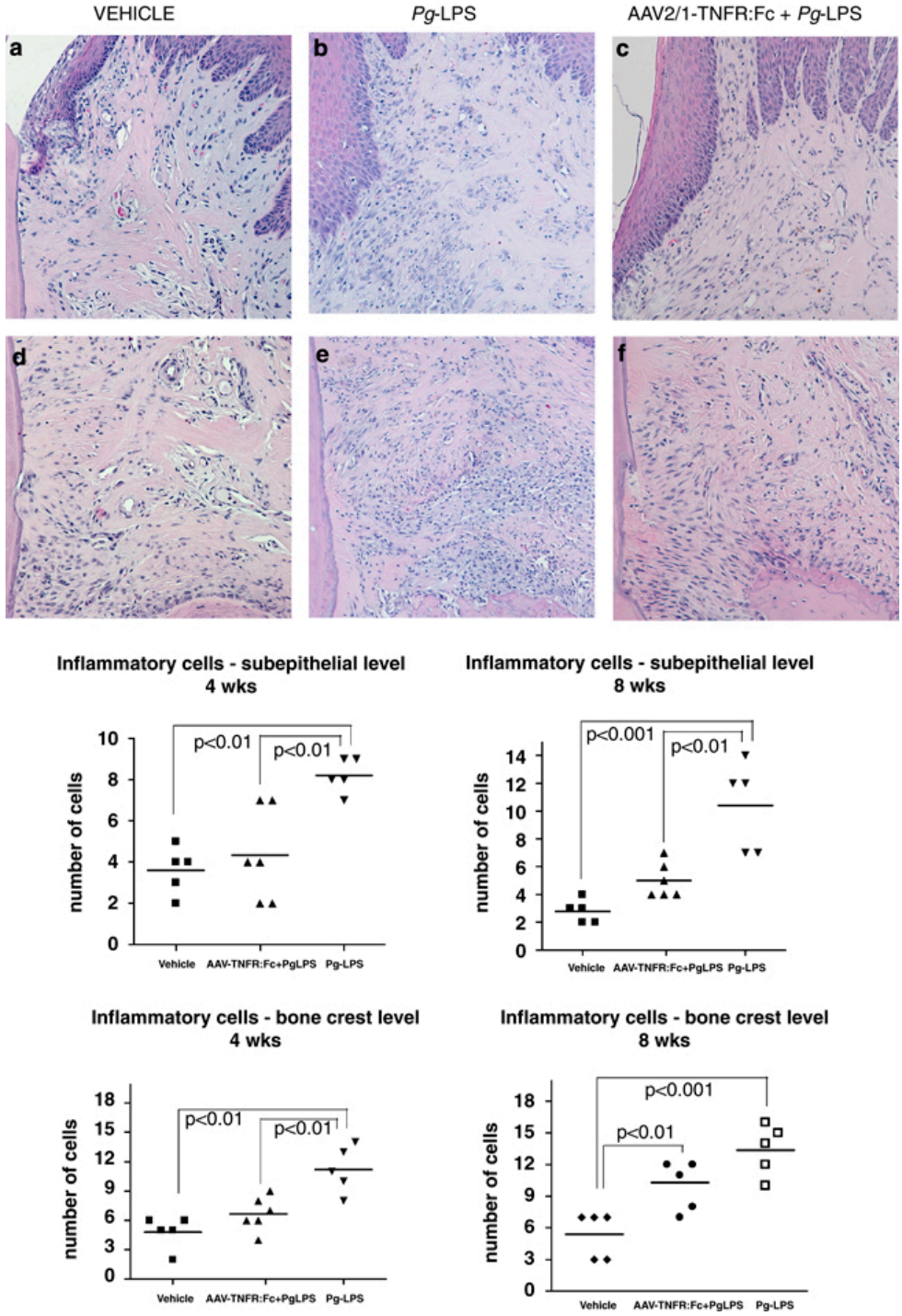

Figure 3.1. Histological sections (H/E, 200X) of subepithelial (upper panels) and bone crest (lower panels) levels of periodontal tissues around the maxillary second molar of Vehicle (a and d), *Pg*-LPS (b and e) and AAV2/1-TNFR:Fc + *Pg*-LPS (c and f) treated

animals, at 4 weeks. The number of inflammatory cells was determined by stereometric analysis using a point-counting technique. A 500 μm^2 rectangular-lattice grid with 50 intersection points was constructed and the type of structure found on the intersection of the grid lines was counted on a optical microscope. (One-way ANOVA and Tukey's *post hoc* tests).

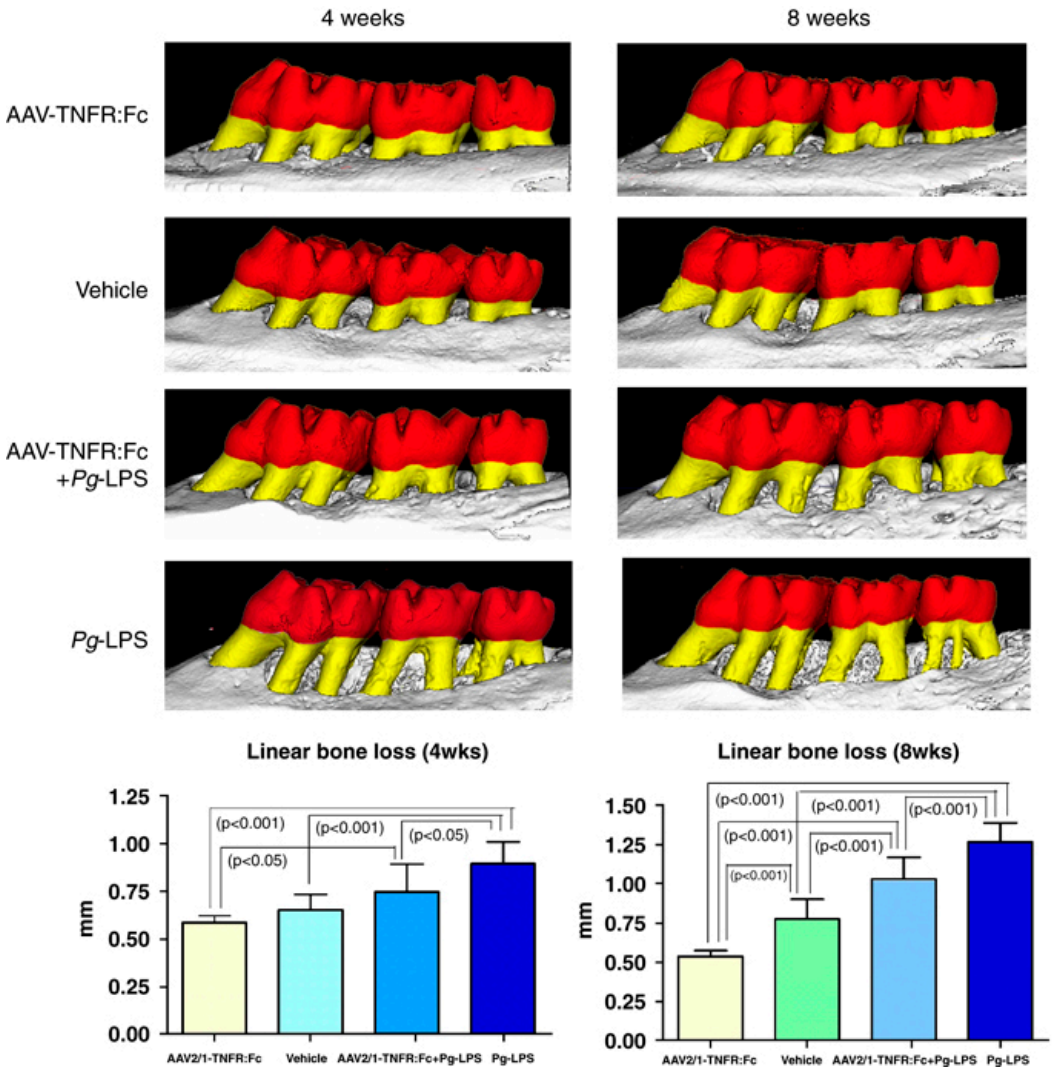

Figure 3.2. Preventive effect of AAV2/1-TNFR:Fc administration on alveolar bone loss induced by *Pg*-LPS injections. Linear vertical bone loss was measured in digitalized micro CT 2D images in the palatal roots of the maxillary second molars at 4 and 8 weeks after *Pg*-LPS-disease induction. Data expressed as means ± SD (n=5/group/timepoint).* Statistically different from all other groups (One-way ANOVA and Tukey's *post hoc* tests).

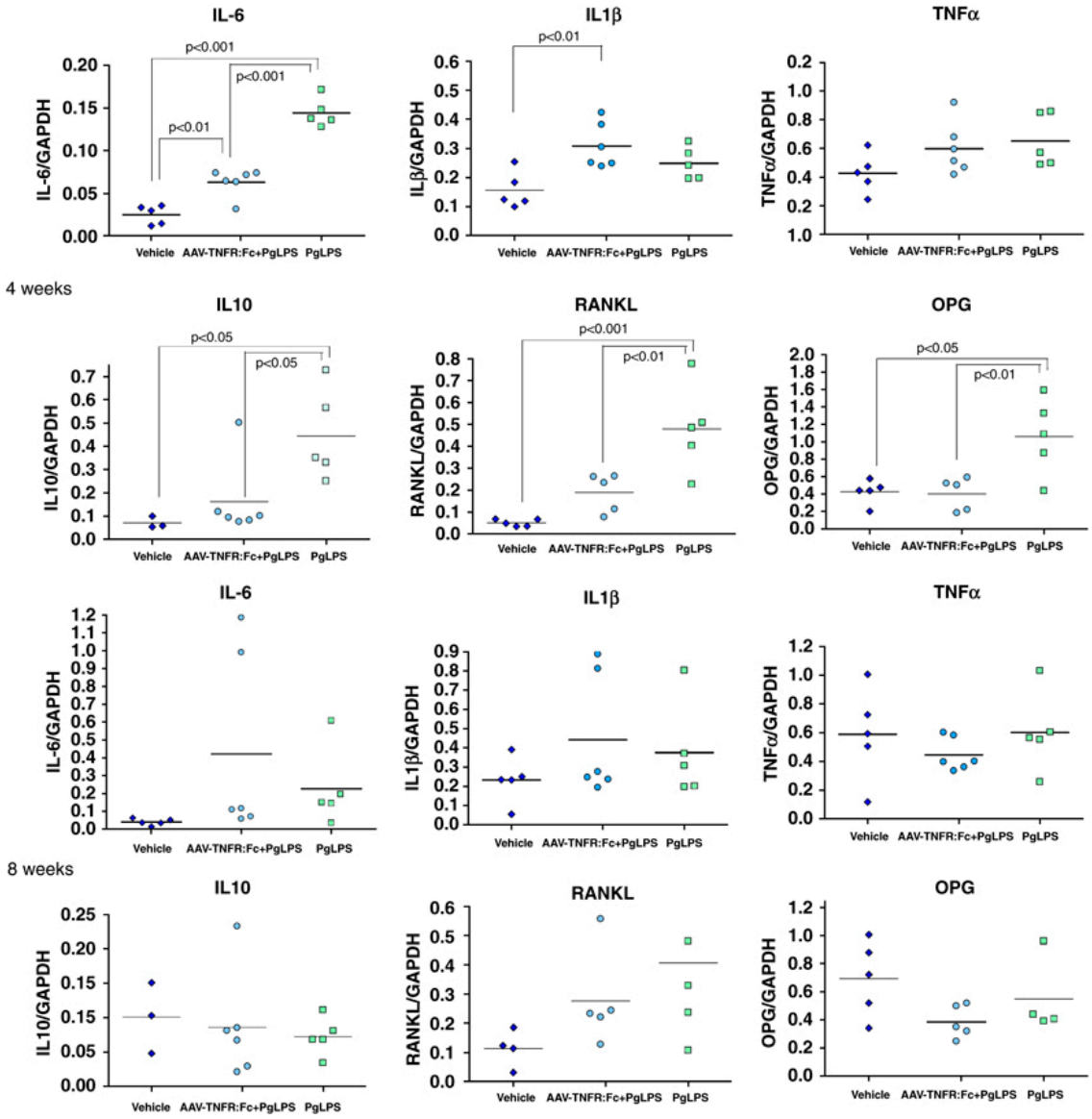

Figure 3.3. Real time PCR results for cytokines (IL-1β, IL-6, TNF-α, IL-10), RANKL and OPG expressions in the palatal gingival tissue, at 4 and 8 weeks timepoints, for groups: AAV2/1:Fc-TNFR + *Pg*-LPS, *Pg*-LPS only and Veh injection. Data expressed as means ± SD (n=5/group/timepoint). (One-way ANOVA and Tukey's *post hoc* tests).

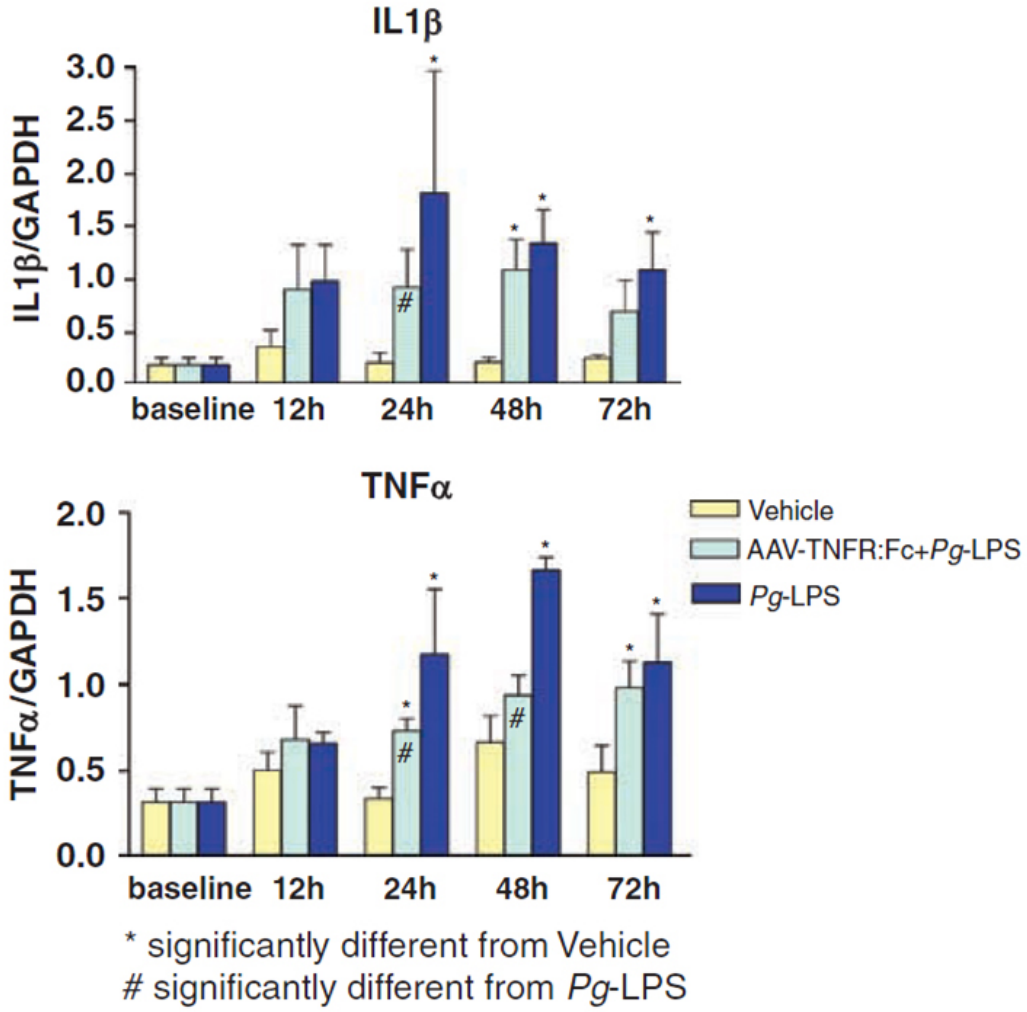

Figure 3.4. Short-term quantitative real time PCR results for TNF-α and IL-1β cytokines expression in a time course experiment after single Pg-LPS injection. Data expressed as means ± SD (n=5/group/timepoit). (One-way ANOVA and Tukey's *post hoc* tests).

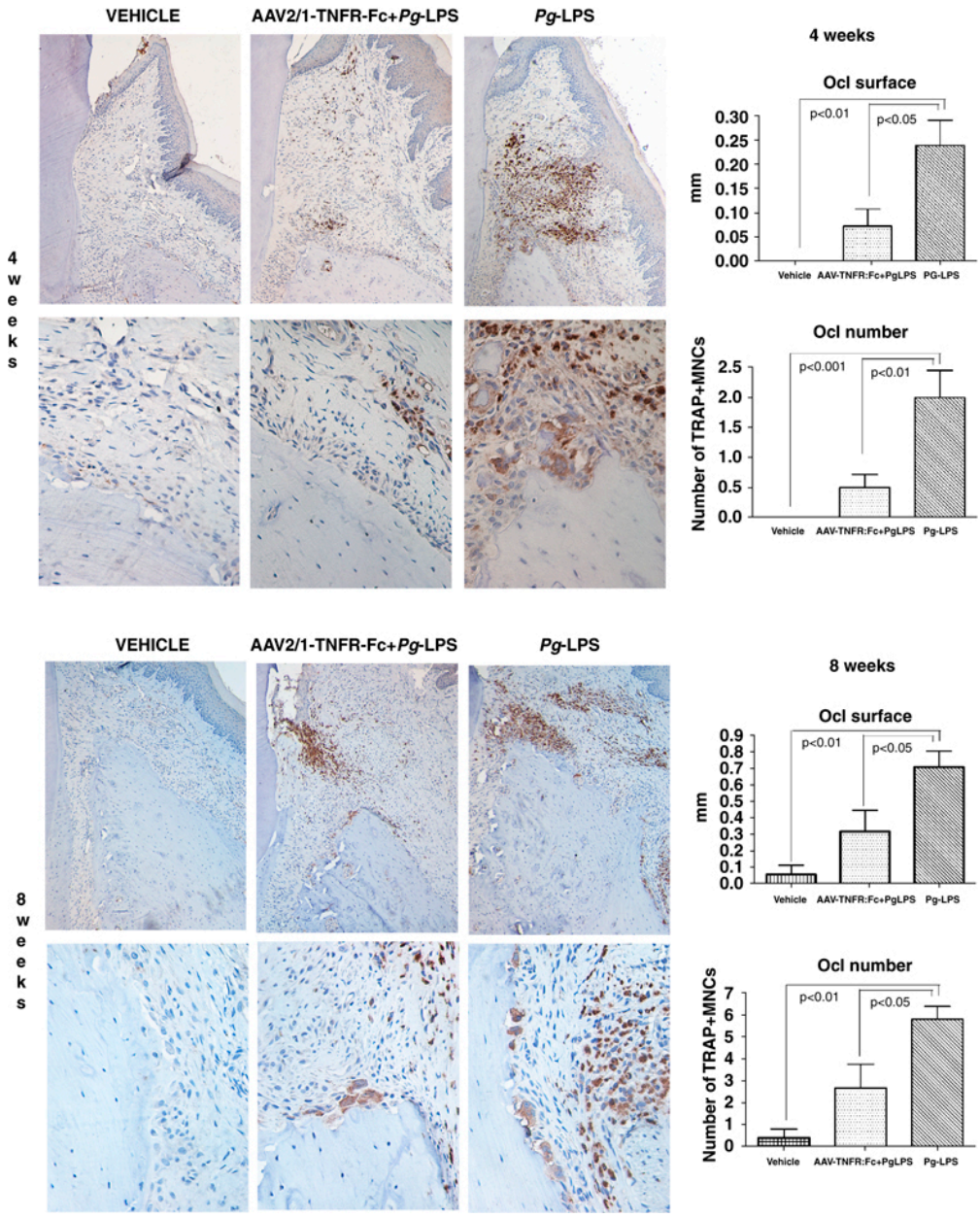

Figure 3.5. TRAP immunohistochemistry for detection of osteoclasts-like cells in the bone surface of the alveolar bone crest in the palatal side of the maxillary molars of animals from the vehicle, *Pg*-LPS only and AAV2/1:Fc-TNFR + *Pg*-LPS groups, at 4 and 8 weeks after experimental disease induction.

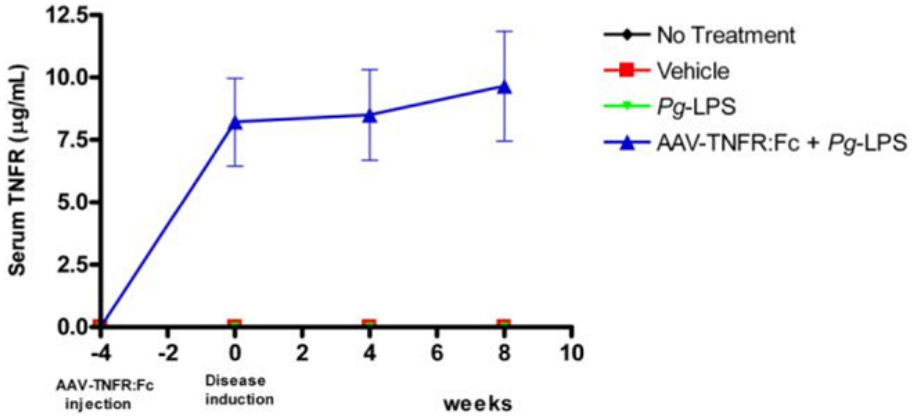

Figure 3.6. Serum TNFR protein levels after intramuscular administration of AAV2/1-TNFR:Fc vector to rats afflicted with *Pg*-LPS experimental periodontitis. Four weeks prior to disease induction, animals were administrated intramuscularly with 10^{11} DRP of AAV2/1-TNFR:Fc vector. Serum levels (µg/mL) of TNFR protein were monitored, at the timepoints indicated, using ELISA. The data are expressed as the means ± SD (n=5/group/timepoint).

* Statistically different from other groups at the same timepoint (One-way ANOVA and Tukey's *post hoc*).

3.7. TABLE

Group	Bone Volume Fraction (BVF)		Bone Mineral Density (BMD)	
	4 weeks Mean ± S.D.	8 weeks Mean ± S.D.	4 weeks Mean ± S.D.	8 weeks Mean ± S.D.
Vehicle	0.617 ± 0.038 [a]	0.596 ± 0.082 [d]	725.67 ± 28.49 [h]	664.95 ± 18.47 [i]
AAV2/1-TNFR:Fc	0.680 ± 0.024 [b,c]	0.682 ± 0.029 [e,f]	673.43 ± 25.38	680.85 ± 31.52 [j,k]
AAV2/1-TNFR:Fc + *Pg*-LPS	0.567 ± 0.099 [b]	0.509 ± 0.079 [e,f]	650.65 ± 90.65	555.50 ± 103.12 [j]
Pg-LPS	0.515 ± 0.032 [a,c]	0.373 ± 0.082 [d,f,g]	587.46 ± 105.47 [h]	489.75 ± 112.68 [I,k]

Table 3.1. Bone Volumetric Fraction (BVF) and Bone Mineral Density (BMD), according to measures 4 and 8 weeks after experimental periodontal disease induction. A-k Similar letters mean statistically significant difference between groups, in the same time point (one-way ANOVA with Tukey's *post-hoc* test)

3.8. REFERENCES

1. Pihlstrom BL, Michalowicz BS, Johnson NW. Periodontal diseases. *Lancet.* 2005;366:1809–1820.

2. Desvarieux M, Demmer RT, Rundek T, Boden-Albala B, Jacobs DR, Jr., Sacco RL, et al. Periodontal microbiota and carotid intima-media thickness: the Oral Infections and Vascular Disease Epidemiology Study (INVEST). *Circulation.* 2005;111:576–582.

3. Akira S, Takeda K, Kaisho T. Toll-like receptors: critical proteins linking innate and acquired immunity. *Nat Immunol.* 2001;2:675–680.

4. Giannobile WV. Host-response therapeutics for periodontal diseases. *J Periodontol.* 2008;79:1592–1600.

5. Reddy MS, Geurs NC, Gunsolley JC. Periodontal host modulation with antiproteinase, anti-inflammatory, and bone-sparing agents. A systematic review. *Ann Periodontol.* 2003;8:12–37.

6. Graves DT, Cochran D. The contribution of interleukin-1 and tumor necrosis factor to periodontal tissue destruction. *J Periodontol.* 2003;74:391–401.

7. Azuma Y, Kaji K, Katogi R, Takeshita S, Kudo A. Tumor necrosis factor-alpha induces differentiation of and bone resorption by osteoclasts. *J Biol Chem.* 2000;275:4858–4864.

8. Ashkenazi A, Dixit VM. Apoptosis control by death and decoy receptors. *Curr Opin Cell Biol.* 1999;11:255–260.

9. Okada H, Murakami S. Cytokine expression in periodontal health and disease. *Crit Rev Oral Biol Med.* 1998;9:248–266.

10. Graves DT, Oskoui M, Volejnikova S, Naguib G, Cai S, Desta T, et al. Tumor necrosis factor modulates fibroblast apoptosis, PMN recruitment, and osteoclast formation in response to P. gingivalis infection. *J Dent Res.* 2001;80:1875–1879.

11. Kim N, Kadono Y, Takami M, Lee J, Lee SH, Okada F, et al. Osteoclast differentiation independent of the TRANCE-RANK-TRAF6 axis. *J Exp Med.* 2005;202:589–595.

12. Kobayashi K, Takahashi N, Jimi E, Udagawa N, Takami M, Kotake S, et al. Tumor necrosis factor alpha stimulates osteoclast differentiation by a mechanism independent of the ODF/RANKL-RANK interaction. *J Exp Med.* 2000;191:275–286.

13. Bouwmeester T, Bauch A, Ruffner H, Angrand PO, Bergamini G, Croughton K, et al. A physical and functional map of the human TNF-alpha/NF-kappa B signal transduction pathway. *Nat Cell Biol.* 2004;6:97–105.

14. Peschon JJ, Torrance DS, Stocking KL, Glaccum MB, Otten C, Willis CR, et al. TNF receptor-deficient mice reveal divergent roles for p55 and p75 in several models of inflammation. *J Immunol.* 1998;160:943–952.

15. Abu-Amer Y, Ross FP, Edwards J, Teitelbaum SL. Lipopolysaccharide-stimulated osteoclastogenesis is mediated by tumor necrosis factor via its P55 receptor. *J Clin Invest.* 1997;100:1557–1565.

16. Garlet GP, Cardoso CR, Campanelli AP, Ferreira BR, Avila-Campos MJ, Cunha FQ, et al. The dual role of p55 tumour necrosis factor-alpha receptor in *Actinobacillus actinomycetemcomitans*-induced experimental periodontitis: host protection and tissue destruction. *Clin Exp Immunol.* 2007;147:128–138.

17. Klareskog L, van der Heijde D, de Jager JP, Gough A, Kalden J, Malaise M, et al. Therapeutic effect of the combination of etanercept and methotrexate compared with each treatment alone in patients with rheumatoid arthritis: double-blind randomised controlled trial. *Lancet.* 2004;363:675–681.

18. van de Putte LB, Atkins C, Malaise M, Sany J, Russell AS, van Riel PL, et al. Efficacy and safety of adalimumab as monotherapy in patients with rheumatoid arthritis for whom previous disease modifying antirheumatic drug treatment has failed. *Ann Rheum Dis.* 2004;63:508–516.

19. Keystone EC, Schiff MH, Kremer JM, Kafka S, Lovy M, DeVries T, et al. Once-weekly administration of 50 mg etanercept in patients with active rheumatoid arthritis: results of a multicenter, randomized, double-blind, placebo-controlled trial. *Arthritis Rheum.* 2004;50:353–363.

20. Scott DL, Kingsley GH. Tumor necrosis factor inhibitors for rheumatoid arthritis. *N Engl J Med.* 2006;355:704–712.

21. van der Heijde DM. Overview of radiologic efficacy of new treatments. *Rheum Dis Clin North Am.* 2004;30:285–293. vi.

22. Catrina AI, af Klint E, Ernestam S, Catrina SB, Makrygiannakis D, Botusan IR, et al. Anti-tumor necrosis factor therapy increases synovial osteoprotegerin expression in rheumatoid arthritis. *Arthritis Rheum.* 2006;54:76–81.

23. Assuma R, Oates T, Cochran D, Amar S, Graves DT. IL-1 and TNF antagonists inhibit the inflammatory response and bone loss in experimental periodontitis. *J Immunol.* 1998;160:403–409.

24. Delima AJ, Oates T, Assuma R, Schwartz Z, Cochran D, Amar S, et al. Soluble antagonists to interleukin-1 (IL-1) and tumor necrosis factor (TNF) inhibits loss of tissue attachment in experimental periodontitis. *J Clin Periodontol.* 2001;28:233–240.

25. Graves DT, Delima AJ, Assuma R, Amar S, Oates T, Cochran D. Interleukin-1 and tumor necrosis factor antagonists inhibit the progression of inflammatory cell infiltration toward alveolar bone in experimental periodontitis. *J Periodontol.* 1998;69:1419–1425.

26. Oates TW, Graves DT, Cochran DL. Clinical, radiographic and biochemical assessment of IL-1/TNF-alpha antagonist inhibition of bone loss in experimental periodontitis. *J Clin Periodontol.* 2002;29:137–143.

27. Lima V, Vidal FD, Rocha FA, Brito GA, Ribeiro RA. Effects of tumor necrosis factor-alpha inhibitors pentoxifylline and thalidomide on alveolar bone loss in short-term experimental periodontal disease in rats. *J Periodontol.* 2004;75:162–168.

28. Taylor PC. Anti-tumor necrosis factor therapies. *Curr Opin Rheumatol.* 2001;13:164–169.

29. Chan JM, Villarreal G, Jin WW, Stepan T, Burstein H, Wahl SM. Intraarticular gene transfer of TNFR:Fc suppresses experimental arthritis with reduced systemic distribution of the gene product. *Mol Ther.* 2002;6:727–736.

30. Sandalon Z, Bruckheimer EM, Lustig KH, Burstein H. Long-term suppression of experimental arthritis following intramuscular administration of a pseudotyped AAV2/1-TNFR:Fc Vector. *Mol Ther.* 2007;15:264–269.

31. Muthukuru M, Jotwani R, Cutler CW. Oral mucosal endotoxin tolerance induction in chronic periodontitis. *Infect Immun.* 2005;73:687–694.

32. WHO *Evidence for action.* World Health Organization; 2003. Adherence to long-term therapies. Available from: http://www.who.int/mediacentre/releases/2003/pr2054/en/.

33. Warrington KH, Jr., Herzog RW. Treatment of human disease by adeno-associated viral gene transfer. *Hum Genet.* 2006;119:571–603.

34. Bartold PM, Marshall RI, Haynes DR. Periodontitis and rheumatoid arthritis: a review. *J Periodontol.* 2005;76:2066–2074.

35. Socransky SS, Haffajee AD. The bacterial etiology of destructive periodontal disease: current concepts. *J Periodontol.* 1992;63:322–331.

36. Darveau RP, Pham TT, Lemley K, Reife RA, Bainbridge BW, Coats SR, et al. Porphyromonas gingivalis lipopolysaccharide contains multiple lipid A species that functionally interact with both toll-like receptors 2 and 4. *Infect Immun.* 2004;72:5041–5051.

37. Broad A, Jones DE, Kirby JA. Toll-like receptor (TLR) response tolerance: a key physiological "damage limitation" effect and an important potential opportunity for therapy. *Curr Med Chem.* 2006;13:2487–2502.

38. Grutz G. New insights into the molecular mechanism of interleukin-10-mediated immunosuppression. *J Leukoc Biol.* 2005;77:3–15.

39. Ridderstad A, Abedi-Valugerdi M, Moller E. Cytokines in rheumatoid arthritis. *Ann Med.* 1991;23:219–223.

40. Nanes MS. Tumor necrosis factor-alpha: molecular and cellular mechanisms in skeletal pathology. *Gene.* 2003;321:1–15.

41. Nagasawa T, Kobayashi H, Kiji M, Aramaki M, Mahanonda R, Kojima T, et al. LPS-stimulated human gingival fibroblasts inhibit the differentiation of monocytes into osteoclasts through the production of osteoprotegerin. *Clin Exp Immunol.* 2002;130:338–344.

42. Almasri A, Wisithphrom K, Windsor LJ, Olson B. Nicotine and lipopolysaccharide affect cytokine expression from gingival fibroblasts. *J Periodontol.* 2007;78:533–541.

43. Wada N, Maeda H, Yoshimine Y, Akamine A. Lipopolysaccharide stimulates expression of osteoprotegerin and receptor activator of NF-kappa B ligand in periodontal ligament fibroblasts through the induction of interleukin-1 beta and tumor necrosis factor-alpha. *Bone.* 2004;35:629–635.

44. Wang PL, Azuma Y, Shinohara M, Ohura K. Toll-like receptor 4-mediated signal pathway induced by Porphyromonas gingivalis lipopolysaccharide in human gingival fibroblasts. *Biochem Biophys Res Commun.* 2000;273:1161–1167.

45. Nakashima T, Kobayashi Y, Yamasaki S, Kawakami A, Eguchi K, Sasaki H, et al. Protein expression and functional difference of membrane-bound and soluble receptor activator of NF-kappaB ligand: modulation of the expression by osteotropic factors and cytokines. *Biochem Biophys Res Commun.* 2000;275:768–775.

46. Kawai T, Matsuyama T, Hosokawa Y, Makihira S, Seki M, Karimbux NY, et al. B and T lymphocytes are the primary sources of RANKL in the bone resorptive lesion of periodontal disease. *Am J Pathol.* 2006;169:987–998.

47. Anderson DM, Maraskovsky E, Billingsley WL, Dougall WC, Tometsko ME, Roux ER, et al. A homologue of the TNF receptor and its ligand enhance T-cell growth and dendritic-cell function. *Nature.* 1997;390:175–179.

48. Teng YT. Protective and destructive immunity in the periodontium: Part 2--T-cell-mediated immunity in the periodontium. *J Dent Res.* 2006;85:209–219.

49. Sandalon Z, Bruckheimer EM, Lustig KH, Rogers LC, Peluso RW, Burstein H. Secretion of a TNFR:Fc fusion protein following pulmonary administration of pseudotyped adeno-associated virus vectors. *J Virol.* 2004;78:12355–12365.

50. Gao GP, Qu G, Faust LZ, Engdahl RK, Xiao W, Hughes JV, et al. High-titer adeno-associated viral vectors from a Rep/Cap cell line and hybrid shuttle virus. *Hum Gene Ther.* 1998;9:2353–2362.

51. Darveau RP, Hancock RE. Procedure for isolation of bacterial lipopolysaccharides from both smooth and rough Pseudomonas aeruginosa and Salmonella typhimurium strains. *J Bacteriol.* 1983;155:831–838.

52. Park CH, Abramson ZR, Taba M, Jr., Jin Q, Chang J, Kreider JM, et al. Three-dimensional micro-computed tomographic imaging of alveolar bone in experimental bone loss or repair. *J Periodontol.* 2007;78:273–281.

53. Liu D, Xu JK, Fibliomeni L, et al. Expression of RANKL and OPG mRNA in periodontal disease: Possible involvement in bone destruction. *Int J Mol Med.* 2003;11:17–21.

54. Wara-aswapati N, Surarit R, Chayasadom A, Boch JA, Pitiphat W. RANKL upregulation associated with periodontitis and Porphyromonas gingivalis. *J Periodontol.* 2007;78:1062–1069.

CHAPTER FOUR

RANKL INHIBITIONS THROUGH OSTEOPROTEGERIN BLOCKS BONE LOSS IN EXPERIMENTAL PERIODONTITIS

Jin Q, Cirelli JA, **Park CH**, Sugai JV, Taba Jr. M, Kostenuik P, Giannobile WV.

Journal of Periodontology, **2007** 78(7): 1300-1308

4.1. ABSTRACT

Background: Prevention of alveolar bone destruction is a clinical challenge in periodontal disease treatment. The receptor activator of nuclear factor-kappa B ligand (RANKL) inhibitor osteoprotegerin (OPG) inhibits osteoclastogenesis and suppresses bone resorption.

Methods: To study the effects of RANKL inhibition on alveolar bone loss, an experimental ligature-induced model of periodontitis was used. A total of 32 rats were administered human OPG-Fc fusion protein (10 mg/kg) or vehicle by subcutaneous delivery twice weekly for 6 weeks. Negative or positive controls received no treatment or disease through vehicle delivery, respectively. Biopsies were harvested after 3 and 6 weeks, and mandibulae were evaluated by microcomputed tomography (μCT) and

histology. Serum levels of human OPG-Fc and tartrate-resistant acid phosphatase-5b (TRAP-5b) were measured throughout the study by enzyme-linked immunosorbent assay (ELISA). Statistical analyses included analysis of variance (ANOVA) and Tukey tests.

Results: Human OPG-Fc was detected in the sera of OPG-Fc–treated animals by 3 days and throughout the study. Serum TRAP-5b was sharply decreased by OPG-Fc treatment soon after OPG-Fc delivery and remained low for the observation period. Significant preservation of alveolar bone volume was observed among OPG-Fc–treated animals compared to the controls at weeks 3 and 6 (P <0.05). Descriptive histology revealed that OPG-Fc significantly suppressed osteoclast surface area at the alveolar crest.

Conclusion: Systemic delivery of OPG-Fc inhibits alveolar bone resorption in experimental periodontitis, suggesting that RANKL inhibition may represent an important therapeutic strategy for the prevention of progressive alveolar bone loss.

4.2. INTRODUCTION

Periodontitis is a destructive disease that targets tooth-supporting structures through complex and multifactorial pathogenic processes. It is triggered by an interaction between bacterial components of tooth-associated biofilms and host response mechanisms [1]. Alveolar bone destruction, a hallmark of periodontitis progression and one of the major causes of tooth loss in humans, is mediated by the host immune and inflammatory response to microbial challenge. In recent decades, studies on cellular and molecular mechanisms of bone loss in periodontitis have suggested that the use of host modulation agents is an important adjunctive therapy to antimicrobial strategies [2].

The discovery of the receptor activator of nuclear factor-kappa B (RANK)/RANK ligand (RANKL)/osteoprotegerin (OPG) axis has improved the knowledge of bone metabolism regulation and created a new field for the study of treatment of bone destruction–related diseases, including rheumatoid arthritis, metastatic bone cancer, and periodontal disease. The RANKL/RANK interaction is needed for differentiation and maturation of osteoclast precursor cells to activated osteoclasts and for the survival of mature osteoclasts. Stimulatory factors such as hormones (vitamin D_3, parathyroid hormone, parathyroid hormone–related protein), cytokines (interleukin-1, -6, -11, and -17), growth factors (tumor necrosis factor-α and bone morphogenetic protein-2), and other molecules (prostaglandin E_2, cytoplasmic domain-40L, and glucocorticoid), upregulate the expression of the RANKL gene in osteoblasts/stromal cells [3, 4]. Sequentially, RANKL triggers osteoclastogenesis through RANK on preosteoclast cells. Acting as a soluble decoy receptor, OPG binds to RANKL and inhibits osteoclast development. Several

studies have shown the opposing effects of RANKL and OPG on bone turnover. Genetic ablation of RANKL in mice results in osteopetrosis [5,6], whereas genetic deletion of OPG in mice results in high bone turnover and severe osteoporosis [7-9]. Moreover, several factors initiating bone resorption not only upregulate RANKL expression but also inhibit OPG expression in osteoblasts/stromal cells [3, 10]. Upregulation of RANKL has also been seen in inflamed periodontal tissues, indicating that RANKL participates in the processes of periodontal tissue destruction [11, 12]. On the other hand, the RANKL/OPG ratio is increased in periodontitis compared to non-diseased individuals, suggesting that this molecular interaction may be important in modulating local bone loss. The RANKL/OPG ratio was found to be significantly increased in gingival crevicular fluid (GCF) of patients with periodontitis compared to healthy individuals [13].

As a therapeutic drug for preventing bone loss, OPG has recently been evaluated in preclinical studies relating to estrogen deficiency, skeletal tumors, and specific cancers [6, 14-17], as well as in clinical trials involving postmenopausal women, juvenile Paget's disease, and lytic bone disease associated with cancer [18-20]. All of these results showed that OPG has significant effects on the inhibition of bone loss.

The use of OPG as an inhibitor of alveolar bone destruction in periodontal disease was studied in mice orally infected with *Actinobacillus actinomycetencomitans*. Inhibition of RANKL function with OPG treatment significantly reduced the number of osteoclasts and alveolar bone loss [21, 22]. The aim of this study was to evaluate the therapeutic effects of human recombinant OPG fusion protein (rhOPG-Fc) on preventing alveolar

bone loss in an acute model of ligature-induced experimental periodontitis as assessed histologically and morphometrically.

4.3. MATERIALS AND METHODS

4.3.1. Experimental Design

All animal experiment procedures in this study were approved by the University of Michigan Committee of Use and Care of Animals.

To explore the OPG-Fc effects on alveolar bone loss in experimental periodontitis, 32 male Sprague-Dawley rats (Harlan, Indianapolis, IN USA; weight: 250 to 300 g) were divided into four experimental groups: group A, animals receiving no treatment (normal healthy control or NT); group B, animals receiving rhOPG-Fc (Amgen, Thousand Oaks, CA USA) subcutaneous administration twice weekly (OPG-treated healthy controls or OPG alone group); group C, animals exposed to disease induction and OPG subcutaneous injection twice weekly (OPG-treated diseased animals); and group D, animals exposed to disease induction and subcutaneous vehicle administration twice weekly (vehicle-treated diseased animals). There were four animals at each designated time point for each group. Block biopsies were harvested at 3 and 6 weeks after disease induction and/or OPG administration.

To further study the in vivo pharmacokinetics of injected rhOPG-Fc, four normal healthy animals received a single subcutaneous administration of rhOPG-Fc, and serum rhOPG-Fc was measured by an enzyme-linked immunosorbent assay (ELISA) at designated time points.

4.3.2. Experimental Periodontal Disease Induction and OPG Administration

Sprague-Dawley rats were anesthetized using inhalation anesthesia with isoflurane. 3/0 cotton ligatures were placed bilaterally into the gingival sulci of the mandibular first molar teeth. The ligatures were evaluated twice weekly, gently displaced apically into the gingival sulci to ensure a subgingival position, and replaced when necessary. The use of ligatures for induction of experimental periodontitis elicits rapid alveolar bone destruction through two combined mechanisms: an inflammatory process induced by increased microbial biofilm formation around the cervix of the teeth and an acute physical irritation factor as a consequence of the subgingival placement of the ligature, typically leading to the loss of approximately one-half of the bone support over a period of 3 to 6 weeks. The rhOPG-Fc was administered subcutaneously at a dose of 10 mg/kg animal body weight twice a week during 3 or 6 weeks.

4.3.3. In Vivo Pharmacokinetics of Injected rhOPG-Fc

To study the pharmacokinetics of a single subcutaneous injection of rhOPG-Fc at a dose of 10 mg/kg rat body weight, ~600 µl blood was drawn from the tail vein of each animal at 0, 0.5, 1, 3, 7, 14, and 21 days. The samples were transferred into serum separator tubes (Becton Dickinson, Franklin Lakes, NY USA) and centrifuged at 4,000 rpm for 10 minutes at 4°C. The supernatants were collected and stored at −80°C until needed for analysis. The content of serum rhOPG-Fc was measured using a commercially available human OPG ELISA kit (American Laboratory, Windham, NH USA). The ELISA procedures were performed according to the manufacturer's instructions.

4.3.4. Serum rhOPG-Fc and Tartrate-Resistant Acid Phosphatase-5b (TRAP-5b) Measurements During Disease Progression

To measure rhOPG-Fc serum concentration after twice weekly OPG injections as a part of the experimental protocol, the blood from the tail vein was drawn at 0, 1.5, 3, 4.5, and 6 weeks, and serum was collected according to the methods outlined above.

Serum rhOPG-Fc and TRAP-5b levels were measured by commercially available human OPG (ALPCO Diagnostics, Salem NH USA) and rat TRAP-5b (RatTRAP Assay, SBA Sciences, Oulu, Finland) ELISA kits, respectively. The ELISA procedures were performed according to the manufacturer's instructions.

4.3.5. OPG-Fc Clearance From Bone

Young male rats were injected once (intravenously [IV]) with rhOPG-Fc at 5 mg/kg. Groups of rats (N = 6) were sacrificed at various times after treatment. Histologic sections of the proximal tibial metaphysis were subjected to immunohistochemistry analysis for human Fc (immunoglobulin [IgG]1). Deparaffinized 4-μm sections were blocked (CAS Block, Zymed Laboratories, San Francisco CA USA), and sections were incubated with rabbit anti-human IgG (Jackson Laboratories, West Grove, PA USA) at 1:4,000 for 1 hour. Antibody was detected by biotinylated goat anti-rabbit IgG (Vector Laboratories, Burlingame, CA USA) and followed with alkaline phosphatase ABC complex (Vector Laboratories). The reaction was visualized with red alkaline phosphatase substrate (Vector Laboratories). All sections were counterstained with hematoxylin.

4.3.6. Microcomputed Tomography (μCT) Scanning and Analysis

In vitro μCT provides high qualification and accurate quantification of mineralized tissues such as alveolar bone and teeth [23]. Each mandibular specimen was scanned and reconstructed at 18 × 18 × 18-μm voxels using a μCT system (GE Healthcare, London, ON Canada). A three-dimensional (3-D) volume viewer and analyzer software (MicroView Analysis+ v.2.1.2 software, GE Healthcare) were used as the tool for both 3-D and 2-D visualization and quantification.

Linear and volumetric analyses were based on a previously developed methodology [23]. In brief, vertical, linear bone loss was obtained by measuring the distance from the cemento-enamel junction (CEJ) to the alveolar bone crest or to the base of the alveolar intrabony defect at the mesial surface of the mandibular first molar teeth. In terms of 3-D analysis, the most mesial root of the first molar (m-M1), the second molar (m-M2), the roof of the furcation, and root apex of M1 were used as reproducible landmarks for estimation of alveolar bone loss. Two-dimensional regions of interest (ROIs) were drawn at regular intervals (average, eight data slices) on a coronal view and reconstructed as a 3-D structure to quantify volumetric parameters, bone volume fraction (BVF), and bone mineral density (BMD; mg/cc). The measurements of coded specimens were made by two independent, calibrated examiners (JAC and CHP).

4.3.7. Histology and TRAP Immunostaining

TRAP immunohistochemical staining was performed to identify and quantify osteoclast-like cells. Harvested mandibulae were fixed for 48 hours in 10% neutral-buffered

formalin, decalcified with 10% EDTA for 2 weeks, embedded in paraffin, and cut into 4- to 5-μm-thick sections. TRAP immunohistochemical staining was performed on these sections with anti-TRAP antibody (sc-30833, Santa Cruz Biotechnology, Santa Cruz, CA USA) and an immunostaining kit (Goat ABC Staining System kit (sc-2023), Santa Cruz Biotechnology) to identify osteoclast-like cells covering the bone surface.

Images of coded specimens were captured using a microscope (Eclipse 50i, Nikon, Melville, NY USA) fitted with a digital camera (Digital Sight DS U1, Nikon) for analysis using software (Image Pro Plus, Media Cybernetics, Silver Spring, MD USA). The length of the bone surface covered by osteoclasts in a 0.5-mm coronal ROI at the alveolar crestal bone was measured by a single calibrated examiner (QJ).

4.3.8. Statistical Analysis

The differences among groups for linear and volumetric bone loss measurements, serum level of rhOPG-Fc and TRAP5b, and osteoclast-like cell surface area were statistically assessed by one-way analysis of variation (ANOVA) with Tukey multiple comparison post hoc test using a statistical software package (GraphPad Prism version 4.0, GraphPad Software, Sandiego, CA USA). The level of significance was set as $P \leq 0.05$.

4.4. RESULTS

4.4.1. In Vivo rhOPG-Fc Pharmacokinetics

The healthy animals receiving a single injection of rhOPG-Fc displayed an increase in serum rhOPG within 12 hours after administration, reaching a maximal level of 23.2 ± 5.1 μg/ml at 3 days. Serum rhOPG subsequently decreased to 1.2 ± 1.4 μg/ml at 14 days and 0.125 ± 0.152 μg/ml at 21 days (Fig. 4.1).

4.4.2. OPG-Fc Clearance From the Vasculature of Rat Bone

After IV injection of human OPG-Fc, OPG primarily was circulated in blood rather than in the bone matrix. At 12 hours after administration, the peak level of serum OPG was reached and subsequently decreased over time. At 20 days, no circulating OPG was found in the blood vessels of bone (Fig. 4.1B).

4.4.3.Serum rhOPG-Fc and TRAP-5b Levels During Disease Progression

Figure 4.2 shows serum rhOPG and TRAP-5b levels after rhOPG-Fc administration twice a week. By 10 days after injection, the serum rhOPG levels of OPG-treated healthy and diseased animals rose sharply to 31.6 ± 12.3 μg/ml and 34 ± 28.4 μg/ml, respectively. The serum OPG within the OPG-treated diseased animals steadily increased over 6 weeks, whereas the serum OPG level within the OPG-treated healthy control showed no changes through 6 weeks. At 6 weeks, the OPG levels in OPG-treated diseased animals were significantly greater than the OPG-treated healthy controls (P <0.01). Compared to the vehicle-treated diseased animals, OPG levels of OPG-treated animals were significantly

higher at each designated time point (P <0.01; Fig. 4.2A). The endogenous OPG levels in normal healthy controls and vehicle-treated animals were low (data not shown).

The changes in serum TRAP-5b levels within the rhOPG-Fc–injected and nonrhOPG-Fc–injected animals are shown in Figure 3-B.2B. During the first 10 days after rhOPG-Fc administration, serum TRAP-5b levels in rhOPG-Fc–injected animals sharply declined to undetectable levels, whereas TRAP-5b levels in non-rhOPGFc–treated animals decreased only slightly or remained unchanged. After 10 days, the serum TRAP-5b levels of rhOPG-Fc–treated animals sustained lower levels, but the serum TRAP-5b levels of non-rhOPG-Fc–treated animals slowly decreased. At all time points except baseline, the TRAP-5b levels in rhOPG-Fc–delivered animals were significantly lower than those of non-rhOPG-Fc–injected animals (P <0.01). No other groups displayed differences in TRAP-5b levels (Fig. 4.2B).

4.4.4. μCT Analysis

The alveolar bone crest at 3 weeks within the vehicle-treated animals significantly decreased from 0.83 ± 0.1 mm (no treatment group) to 1.28 ± 0.2 mm, which indicates that ~50% bone loss was elicited by experimental periodontitis (Figs. 4.3 and 4.4A). At 6 weeks, the bone crest within the vehicle-treated animals also decreased from 1.05 ± 0.1 mm (no treatment group) to 1.4 ± 0.2 mm, resulting in 40% bone loss. Significant differences of CEJ to bone crest (C-C) distance were only found in the vehicle-treated animals compared to the other three groups.

For volumetric measurements at the 3-week time point, experimental periodontitis resulted in the lowest BVF in the vehicle-treated animals compared to the other three groups, whereas the OPG-treated healthy controls had the highest BVF (Fig. 4.4B). At 6 weeks, the vehicle-treated animals again showed the lowest BVF among all groups, whereas the OPG administration groups had significantly higher BVF compared to the no treatment group (Fig. 4.4B). In terms of BMD, the OPG-treated healthy controls showed the highest BMD, whereas the vehicle-treated animals had the lowest BMD at 3 weeks. At 6 weeks, the vehicle-treated animals had the lowest BMD, and there was a significant difference found between the normal healthy and OPG-treated healthy controls (Fig. 4.4C).

4.4.5.TRAP Immunostaining and Osteoclast Surface Analysis of Alveolar Bone

Histologic analysis of four animals in each group at 3 and 6 weeks revealed increases in TRAP-stained osteoclasts in the region of the alveolar bone crest in diseased vehicle-treated animals compared to healthy controls (Fig. 4.3). In accordance with histologic observations, the coverage of osteoclasts at the alveolar bone crest showed that osteoclasts in vehicle-treated animals occupied ~50% the surface of the alveolar bone within the coronal 0.5 mm, which was the highest of all the groups (Fig. 4.5). In contrast, very few TRAP-stained osteoclasts were observed in OPG-treated animals. OPG treatment of healthy animals was associated with a virtual absence of osteoclasts along the alveolar bone crest, whereas OPG treatment of diseased animals resulted in a three-fold reduction in osteoclast surface compared to vehicle-treated diseased animals (Fig. 4.5). This level of suppression reduced osteoclast surface area to levels found in normal

healthy animals. In addition, compared to the linear bone loss measurement, the bone loss is related to the osteoclast surface area covering the bone (Fig. 4.5). The vehicle-treated diseased animals showed the highest osteoclast coverage and the most extensive bone loss.

4.5. DISCUSSION

To the best of our knowledge, this study showed for the first time a protective effect of OPG in an acute model of experimental periodontitis. To evaluate the effect of human OPG on the alveolar bone changes of rats at physiologic and pathologic conditions, it is imperative to show adequate systemic drug exposure. Human proteins including OPG-Fc can be immunogenic in rats, which would lead to rapid clearance of the drug and inadequate drug exposure. Single-dose pharmacokinetic assessment of human OPG-Fc revealed a C_{max} at day 3, which indicates that twice-weekly administrations would ensure maximal exposure. After twice-weekly OPG administration, >30 μg/ml serum OPG concentration was obtained and sustained, which proved to be the effective serum OPG level to reduce the number of osteoclasts and inhibit bone loss (Figs. 4.4 and 4.5). This serum OPG concentration is similar to the serum OPG level (26.1 ± 5.2 μg/ml) found to be optimal for preventing bone resorption as previously reported by Capparelli et al [24]. However, inflammation may influence in vivo OPG degradation. Serum OPG levels in OPG-treated diseased animals remained elevated and were two-fold higher at 6 weeks compared to the OPG alone group, which may result from the decrease of the OPG degradation-related enzymes elicited by periodontal inflammation.

Three-dimensional images of the mandibular molars generated by μCT were used to evaluate the preventive effects of OPG on alveolar bone loss. Linear measurements indicated that the vehicle-treated animals displayed higher levels of bone loss compared to other groups, whereas both groups receiving OPG injection showed similar bone levels compared to the healthy controls. This suggests that OPG inhibits alveolar bone loss

induced by experimental periodontitis. Protective effects of OPG on alveolar bone resorption were previously shown in an *A. actinomycetencomitans* oral inoculation-induced periodontitis model [21, 22] and a tooth biomechanical movement model (our unpublished data). In addition, measurements of the BVF, representing the percentage of bone volume of the delineated region, were statistically lower in the vehicle-treated animals compared to all other groups at 3 and 6 weeks, showing that experimental periodontitis stimulated more bone loss in the absence of OPG administration. Therefore, OPG seems to rescue not only alveolar bone height but also loss of BMD induced by experimental periodontitis.

To evaluate the effects of OPG on the osteoclast formation in alveolar bone, the coronal 0.5 mm of bone crest at the mesial surface of the first molars was chosen because those areas are under the direct influence of experimental periodontitis and most subject to osteoclast formation. Our results showed that the vehicle-treated diseased animals showed a higher percentage of bone surface covered by TRAP-positive osteoclasts than the other groups at 3 weeks, whereas the OPG-treated diseased animals had the same bone surface coverage of TRAP-positive osteoclasts as normal rats, which suggests that OPG inhibits osteoclast formation. Similar results were also seen in the application of OPG to situations of increased osteoclastic bone resorption, which results from certain types of cancers, rheumatoid arthritis [25] or *A. actinomycetencomitans* inoculation [21, 22]. In addition, OPG administration also causes a decrease in serum TRAP-5b, a marker of osteoclastic resorption [26]. This indicates that the reduction of osteoclast number elicited by OPG application results in a decrease of TRAP-5b originating from osteoclasts.

A potentially important advantage for clinical application of OPG is the lack of incorporation of OPG into bone matrix, as shown in Figure 3-B.1B. As a result, its effects on osteoclasts and bone remodeling are fully reversible [24, 27]. This mechanism of action could have benefits versus agents such as bisphosphonates, which are directly incorporated into bone matrix and thus have poor reversibility. Bisphosphonates have shown efficacy in patients with osteoporosis, Paget's disease, and tumor bone disease [28], and these agents have shown potent effects as host-modulating agents for periodontal disease treatment [29-31]. However, bisphosphonate therapy has also been associated with osteonecrosis of the jaw (ONJ) [32, 33], a condition described by the persistent exposure of necrotic bone in the oral cavity. The etiology of bisphosphonate-related ONJ is poorly understood, but periodontal disease has been the most common comorbidity in bisphosphonate-treated patients with ONJ [32]. In cancer patients on IV bisphosphonates, the relative risk of developing ONJ increases markedly after several years of bisphosphonate use [33]. Bisphosphonate accumulation in bone matrix is a direct function of the total administered dose [34], and the skeletal uptake of bisphosphonates is not reduced by prior high-dose bisphosphonate therapy [35]. These observations suggest that skeletal accumulation of bisphosphonates continues despite the ability of these agents to markedly suppress bone turnover. Because periodontitis can be a chronic disease, it may be inappropriate to use long-term bisphosphonates for the prevention of alveolar bone loss until the etiology of bisphosphonate-related ONJ is elucidated

4.6. CONCLUSIONS

In this study, OPG revealed strong preventive effects on alveolar bone loss in experimental periodontitis, thus showing promising therapeutic potential of OPG for treatment of periodontal disease. Future studies will need to examine the ability of OPG to block progression of established disease and human application.

4.7. FIGURES

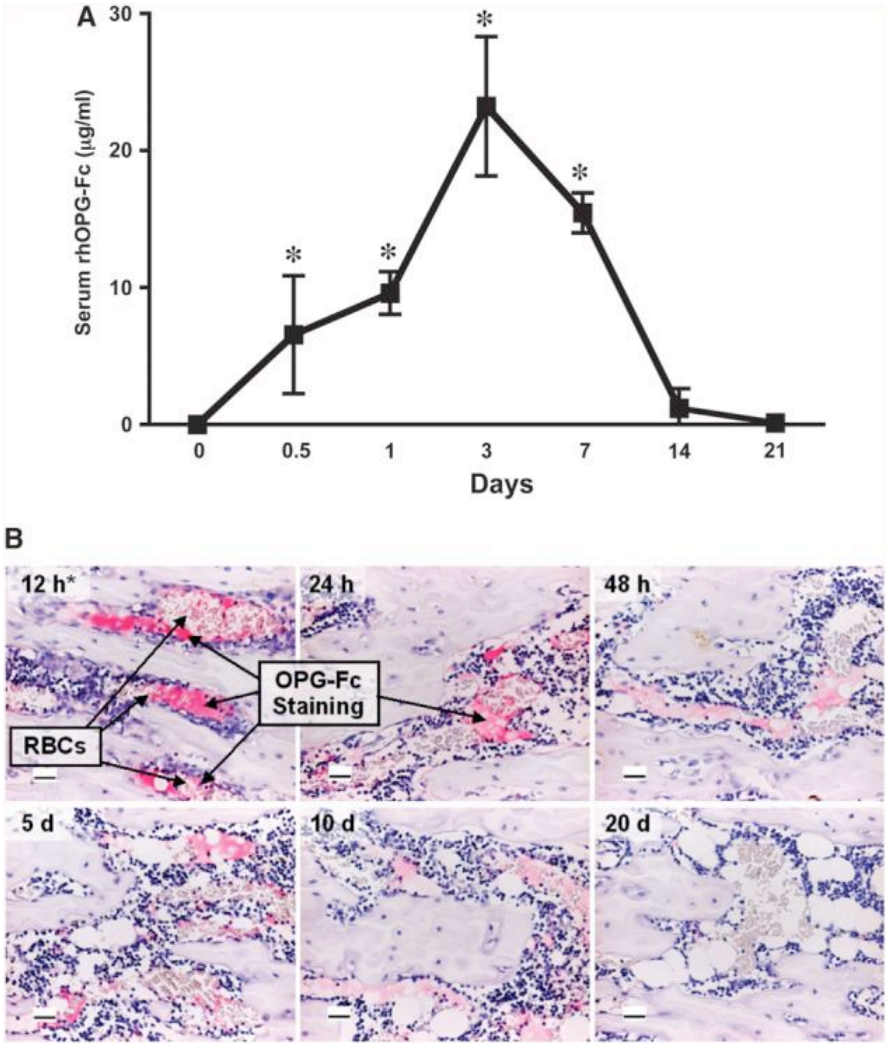

Figure 4. 1. In vivo rhOPG-Fc pharmacokinetics after a single subcutaneous administration. A) The maximum level of serum rhOPG was seen at 3 days after administration. Serum rhOPG decreased within 14 days. At 21 days after injection, the delivered rhOPG was eliminated completely. Bars represent SDs. *P <0.01 compared to baseline. **B)** Human OPG immunostaining in the proximal tibial metaphysis. Young male rats received a single infusion IV with human OPG-Fc at 5 mg/kg. The delivered human OPG circulated primarily in the blood rather than integrating into the bone matrix. The highest serum level of administered human OPG appeared 12 hours after IV infusion, and

the serum OPG was eliminated over time. N = 6 animals per group. Bars = 25 μm. RBCs = red blood cells; h = hours; d = days.

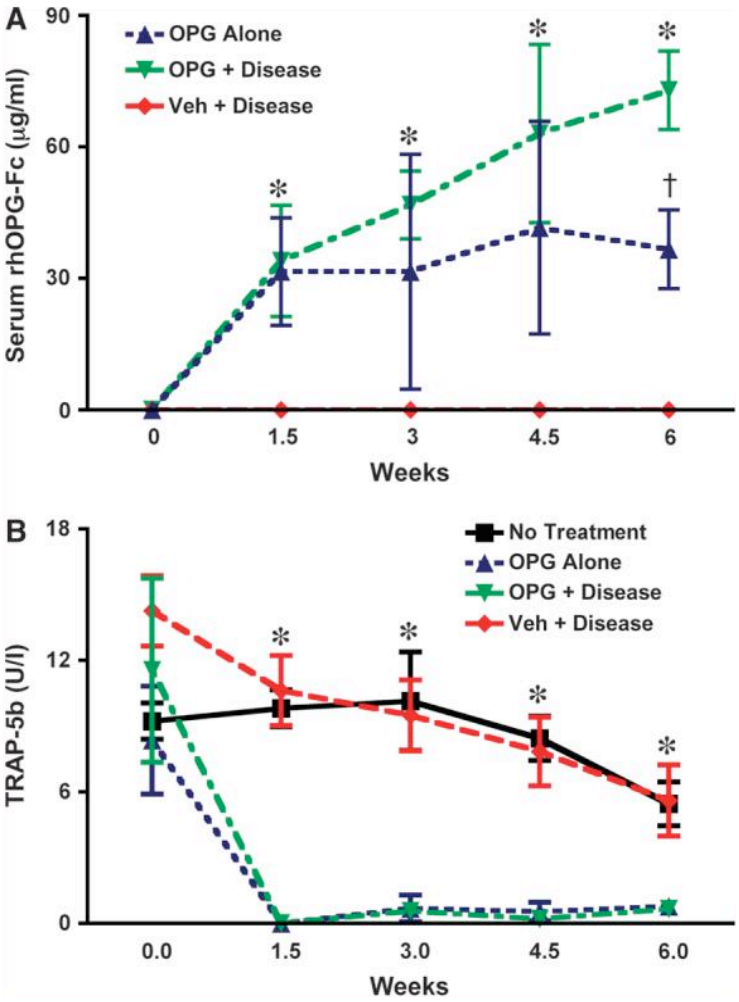

Figure 4. 2. A) **Serum rhOPG levels after twice weekly subcutaneous administration.** Higher serum rhOPG levels were seen in OPG delivery groups, whereas rhOPG levels remained almost undetectable in vehicle-treated animals. At 6 weeks, the serum rhOPG levels between the OPG + disease and the OPG alone groups were statistically significantly different ($^{\dagger}P < 0.05$). *P <0.05 compared to the vehicle group. Bars represent SDs. **B)** Serum TRAP-5b levels after repeated subcutaneous administration. Serum TRAP-5b levels in rhOPG-injected animals decreased sharply at 10 days and remained very low until 6 weeks, whereas the serum TRAP-5b levels in non-rhOPG-injected

animals gradually declined. Except at baseline, the TRAP-5b levels in non-rhOPG-treated groups were significantly higher than those in rhOPG-injected groups. *P <0.05 compared to non-rhOPG-treated groups. Bars represent SDs. N = 4 animals per group. Veh = vehicle.

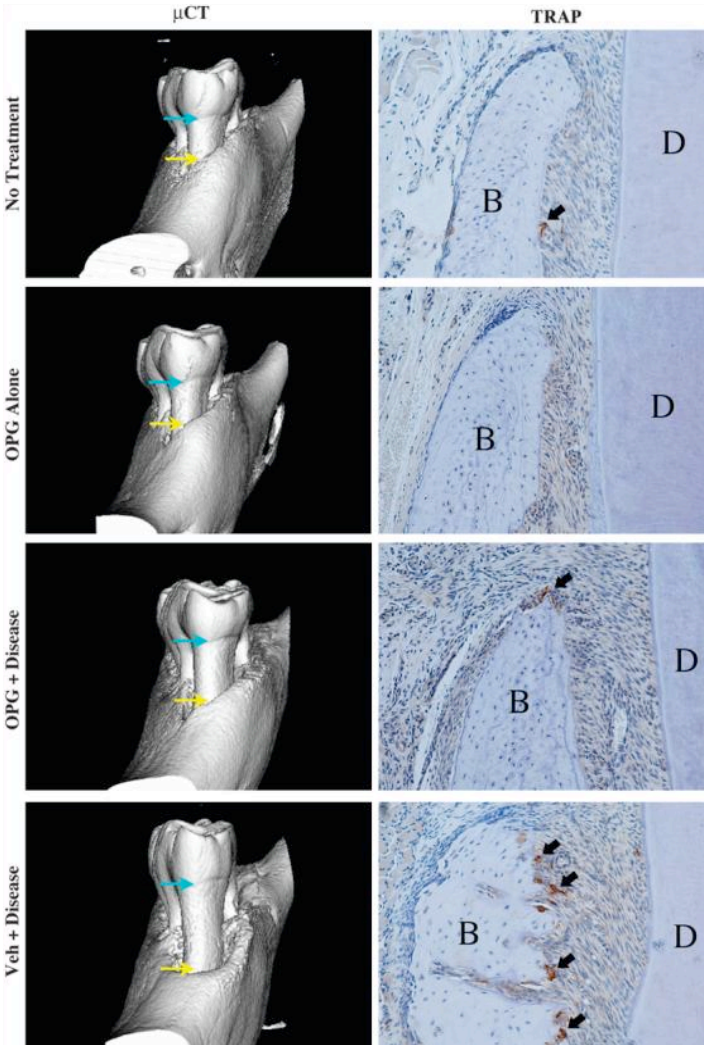

Figure 4. 3. OPG-Fc blocks alveolar bone loss in experimental periodontitis. Left panels show the mesial view of µCT 3-D images of mandibular first molars of each group at 3 weeks. The vehicle + disease group shows the greatest degree of bone loss. Right panels show the histology of the alveolar bone at the mesial side of mandibular first molars of each group at 3 weeks (TRAP immunostaining; magnification, ×200). TRAP-positive osteoclasts are stained brown. Higher numbers of positively stained osteoclasts were noted on the surface of alveolar bone in the vehicle + disease groups. Few osteoclasts were seen at the alveolar bone crest in the OPG + disease group. Furthermore,

no positively stained cells were found in the OPG alone group. Blue arrows demarcate the CEJ. Yellow arrows indicate the alveolar bone crest. Black arrows indicate positive TRAP-stained osteoclast-like cells. Veh = vehicle; B = bone crest; D = dentin. N = 4 animals per group.

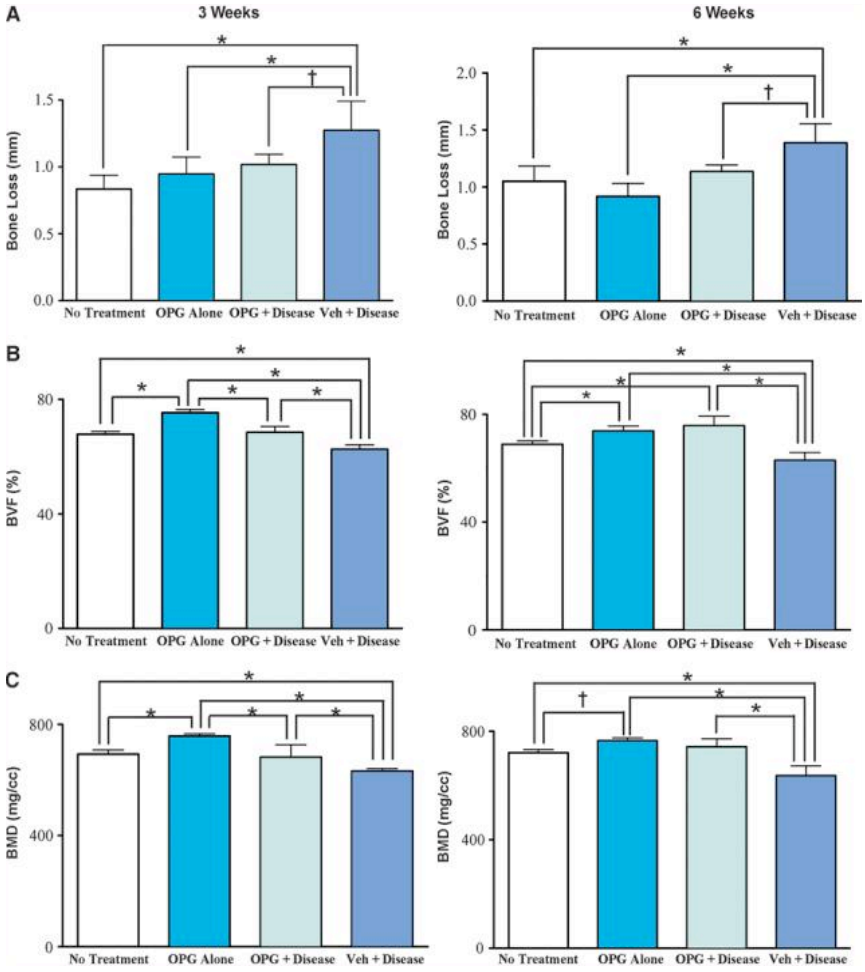

Figure 4. 4. OPG-Fc blocks alveolar bone loss in experimental periodontitis as measured by linear and volumetric µCT. A) The linear measurement of the distance from the CEJ to alveolar bone crest at the mesial roots of mandibular first molars in each group. The greatest difference was seen in the vehicle + disease group at both 3 and 6 weeks, whereas there was no significant difference among other groups. **B)** The fractions of bone volume versus the total volume surrounded by the superficial surfaces of five roots of first mandibular molar. At 3 and 6 weeks, the vehicle + disease group showed the smallest BVF, whereas the OPG alone group displayed the greatest BVF. No significant

difference was found between the no treatment and OPG + disease groups. **C)** BMD for the regions surrounded by the superficial surfaces of all roots of first mandibular molars of each group. At 3 and 6 weeks, BMD in the vehicle + disease group was the lowest, whereas the OPG alone group displayed the highest BMD. No significant difference was found between no treatment and OPG + disease groups. N = 4 animals per group.*P <0.05; †P <0.01; bars represent SDs. Veh = vehicle.

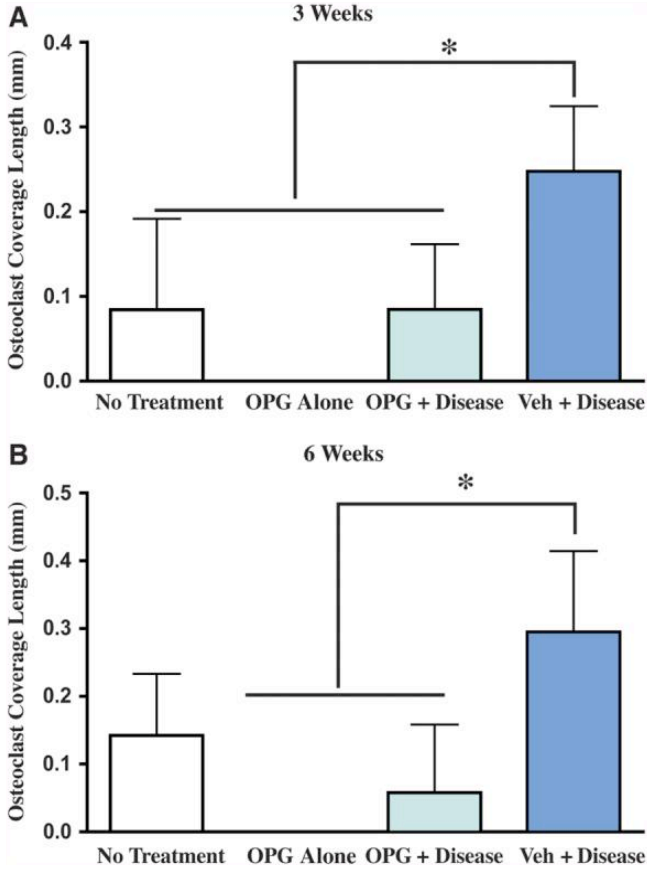

Figure 4. 5. OPG administration inhibits osteoclast formation at the alveolar bone crest in experimental periodontitis. The osteoclast surface coverage at the coronal 0.5-mm region of interest in alveolar bone at the mesial of the mandibular first molars was evaluated histomorphometrically at 3 and 6 weeks using TRAP immunostaining. At 3 weeks, osteoclast coverage area was the greatest in the vehicle + disease group, whereas there were no significant differences noted among the other three groups. At 6 weeks, the vehicle + disease group had the greatest osteoclast coverage at the alveolar crest compared to OPG administration groups, with no significant difference with the no treatment group. *P <0.05. N = 4 animals per group. Veh = vehicle.

4.8. REFERENCES

1. Page RC, Kornman KS. The pathogenesis of human periodontitis: An introduction. *Periodontol 2000.* 1997;14:9–11.

2. Kirkwood KL, Cirelli J, Rogers J, Giannobile WV. Novel host response therapeutic approaches to treat periodontal diseases. *Periodontol 2000.* 2007;43:294–315.

3. Hofbauer LC, Khosla S, Dunstan CR, Lacey DL, Boyle WJ, Riggs BL. The roles of osteoprotegerin and osteoprotegerin ligand in the paracrine regulation of bone resorption. *J Bone Miner Res.* 2000;15:2–12.

4. Nakashima T, Kobayashi Y, Yamasaki S, et al. Protein expression and functional difference of membrane-bound and soluble receptor activator of NF-kappaB ligand: Modulation of the expression by osteotropic factors and cytokines. *Biochem Biophys Res Commun.* 2000;275:768–775.

5. Kong YY, Yoshida H, Sarosi I, et al. OPGL is a key regulator of osteoclastogenesis, lymphocyte development and lymph-node organogenesis. *Nature.* 1999;397:315–323.

6. Simonet WS, Lacey DL, Dunstan CR, et al. Osteoprotegerin: A novel secreted protein involved in the regulation of bone density. *Cell.* 1997;89:309–319.

7. Bucay N, Sarosi I, Dunstan CR, et al. Osteoprotegerin-deficient mice develop early onset osteoporosis and arterial calcification. *Genes Dev.* 1998;12:1260–1268.

8. Mizuno A, Amizuka N, Irie K, et al. Severe osteoporosis in mice lacking osteoclastogenesis inhibitory factor/osteoprotegerin. *Biochem Biophys Res Commun.* 1998;247:610–615.

9. Udagawa N, Takahashi N, Yasuda H, et al. Osteoprotegerin produced by osteoblasts is an important regulator in osteoclast development and function. *Endocrinology.* 2000;141:3478–3484.

10. Hasegawa T, Yoshimura Y, Kikuiri T, et al. Expression of receptor activator of NF-kappa B ligand and osteoprotegerin in culture of human periodontal ligament cells. *J Periodontal Res.* 2002;37:405–411.

11. Liu D, Xu JK, Figliomeni L, et al. Expression of RANKL and OPG mRNA in periodontal disease: Possible involvement in bone destruction. *Int J Mol Med.* 2003;11:17–21.

12. Crotti T, Smith MD, Hirsch R, et al. Receptor activator NF kappaB ligand (RANKL) and osteoprotegerin (OPG) protein expression in periodontitis. *J Periodontal Res.* 2003;38:380–387.

13. Mogi M, Otogoto J, Ota N, Togari A. Differential expression of RANKL and osteoprotegerin in gingival crevicular fluid of patients with periodontitis. *J Dent Res.* 2004;83:166–169.

14. Morony S, Capparelli C, Sarosi I, Lacey DL, Dunstan CR, Kostenuik PJ. Osteoprotegerin inhibits osteolysis and decreases skeletal tumor burden in syngeneic and nude mouse models of experimental bone metastasis. *Cancer Res.* 2001;61:4432–4436.

15. Zhang J, Dai J, Qi Y, et al. Osteoprotegerin inhibits prostate cancer-induced osteoclastogenesis and prevents prostate tumor growth in the bone. *J Clin Invest.* 2001;107:1235–1244.

16. Capparelli C, Kostenuik PJ, Morony S, et al. Osteoprotegerin prevents and reverses hypercalcemia in a murine model of humoral hypercalcemia of malignancy. *Cancer Res.* 2000;60:783–787.

17. Oyajobi BO, Anderson DM, Traianedes K, Williams BJ, Yoneda T, Mundy GR. Therapeutic efficacy of a soluble receptor activator of nuclear factor kappaB-IgG Fc

fusion protein in suppressing bone resorption and hypercalcemia in a model of humoral hypercalcemia of malignancy. *Cancer Res.* 2001;61:2572–2578.

18. Bekker PJ, Holloway D, Nakanishi A, Arrighi M, Leese PT, Dunstan CR. The effect of a single dose of osteoprotegerin in postmenopausal women. *J Bone Miner Res.* 2001;16:348–360.

19. Body JJ, Greipp P, Coleman RE, et al. A phase I study of AMGN-0007, a recombinant osteoprotegerin construct, in patients with multiple myeloma or breast carcinoma related bone metastases. *Cancer.* 2003;97:887–892.

20. Cundy T, Davidson J, Rutland MD, Stewart C, DePaoli AM. Recombinant osteoprotegerin for juvenile Paget's disease. *N Engl J Med.* 2005;353:918–923.

21. Teng YT, Nguyen H, Gao X, et al. Functional human T-cell immunity and osteoprotegerin ligand control alveolar bone destruction in periodontal infection. *J Clin Invest.* 2000;106:R59–R67.

22. Mahamed DA, Marleau A, Alnaeeli M, et al. G(−) anaerobes-reactive CD4+ T-cells trigger RANKL-mediated enhanced alveolar bone loss in diabetic NOD mice. *Diabetes.* 2005;54:1477–1486.

23. Park CH, Abramson Z, Taba M, Jr., et al. 3-D micro-CT image analysis of alveolar bone resorption and repair. *J Periodontol.* 2007;78:273–281.

24. Capparelli C, Morony S, Warmington K, et al. Sustained antiresorptive effects after a single treatment with human recombinant osteoprotegerin (OPG): A pharmacodynamic and pharmacokinetic analysis in rats. *J Bone Miner Res.* 2003;18:852–858.

25. Romas E, Sims NA, Hards DK, et al. Osteoprotegerin reduces osteoclast numbers and prevents bone erosion in collagen-induced arthritis. *Am J Pathol.* 2002;161:1419–1427.

26. Halleen JM. Tartrate-resistant acid phosphatase 5B is a specific and sensitive marker of bone resorption. *Anticancer Res.* 2003;23:1027–1029.

27. Kostenuik PJ. Osteoprotegerin and RANKL regulate bone resorption, density, geometry and strength. *Curr Opin Pharmacol.* 2005;5:618–625.

28. Fleisch H. Bisphosphonates: Mechanisms of action and clinical use in osteoporosis – An update. *Horm Metab Res.* 1997;29:145–150.

29. Lane N, Armitage GC, Loomer P, et al. Bisphosphonate therapy improves the outcome of conventional periodontal treatment: Results of a 12-month, randomized, placebo-controlled study. *J Periodontol.* 2005;76:1113–1122.

30. Rocha M, Nava LE, Vazquez de la Torre C, Sanchez-Marin FJ, Garay-Sevilla ME, Malacara JM. Clinical and radiological improvement of periodontal disease in patients with type 2 diabetes mellitus treated with alendronate: A randomized, placebo-controlled trial. *J Periodontol.* 2001;72:204–209.

31. Rocha ML, Malacara JM, Sanchez-Marin FJ, Vazquez de la Torre CJ, Fajardo ME. Effect of alendronate on periodontal disease in postmenopausal women: A randomized placebo-controlled trial. *J Periodontol.* 2004;75:1579–1585.

32. Marx RE, Sawatari Y, Fortin M, Broumand V. Bisphosphonate-induced exposed bone (osteonecrosis/osteopetrosis) of the jaws: Risk factors, recognition, prevention, and treatment. *J Oral Maxillofac Surg.* 2005;63:1567–1575.

33. Bamias A, Kastritis E, Bamia C, et al. Osteonecrosis of the jaw in cancer after treatment with bisphosphonates: Incidence and risk factors. *J Clin Oncol.* 2005;23:8580–8587.

34. Komatsubara S, Mori S, Mashiba T, et al. Long-term treatment of incadronate disodium accumulates microdamage but improves the trabecular bone microarchitecture in dog vertebra. *J Bone Miner Res.* 2003;18:512–520.

35. Lin JH, Chen IW, Duggan DE. Effects of dose, sex, and age on the disposition of alendronate, a potent anti-osteolytic bisphosphonate, in rats. *Drug Metab Dispos.* 1992;20:473–478.

CHAPTER FIVE

LOCAL DELIVERY OF OSTEOPROTEGERIN INHIBITS MECHANICALLY MEDIATED BONE REMODELING IN ORTHODONTIC TOOTH MOVEMENT

Dunn MD, **Park CH**, Kostenuik PJ, Kapila S, Giannobile WV.

Bone, **2007** 41(3): 446-455.

5.1. ABSTRACT

Introduction: The RANKL-OPG axis is a key regulator of osteoclastogenesis and bone turnover activity. Its contribution to bone resorption under altered mechanical states, however, has not been fully elucidated. Here we examined the role of OPG in regulating mechanically induced bone modeling in a rat model of orthodontic tooth movement.

Methods: The maxillary first molars of male Sprague-Dawley rats were moved mesially using a calibrated nickel–titanium spring attached to the maxillary incisor teeth. Two different doses (0.5 mg/kg, 5.0 mg/kg) of a recombinant fusion protein (OPG-Fc), were injected twice weekly mesial to the first molars. Tooth movement was measured using stone casts that were scanned and magnified. Changes in bone quantity were measured using micro-computed tomography and histomorphometric analysis was used to quantify

osteoclasts and volumetric parameters. Finally, circulating levels of TRAP-5b (a bone resorption marker) was measured using enzyme-linked immunosorbent assay.

Results: The 5.0 mg/kg OPG-Fc dose showed a potent reduction in mesial molar movement and osteoclast numbers compared to controls ($p<0.01$). The molar movement was inhibited by 45.7%, 70.6%, and 78.7% compared to controls at days 7, 14, and 21 respectively, with the high dose of OPG. The 0.5 mg dose also significantly ($p<0.05$) inhibited molar movement at days 7 (43.8%) and 14 (31.8%). While incisor retraction was also decreased by OPG-Fc, the ratio of incisor to molar tooth movement was markedly better in the high-dose OPG group (5.2:1, $p<0.001$) compared to the control group (2.3:1) and the low-dose OPG group (2.0:1).

Conclusions: Local delivery of OPG-Fc inhibits osteoclastogenesis and tooth movement at targeted dental sites.

5.2. INTRODUCTION

Bone deposition and resorption result from the interaction between bone-forming osteoblasts and bone-resorbing osteoclasts. Cells of the osteoblast lineage are not only involved in bone formation, but also regulate osteoclast formation, activation, and survival. This regulation is indirectly mediated by receptor activator of nuclear factor κB ligand (RANKL), a member of the tumor necrosis factor (TNF) superfamily. RANKL is produced by osteoblast lineage cells, periodontal ligament (PDL) cells, and by T lymphocytes. RANKL binds to a receptor called RANK, which is located on the surface of osteoclasts and osteoclast precursors. The binding of RANKL to RANK induces osteoclastogenesis, activates mature osteoclasts, mediates their attachment to bone, and promotes their survival. The activity of RANKL is controlled by a soluble decoy receptor called osteoprotegerin (OPG), which binds to RANK and inhibits osteoclast formation, activation, and survival [1].

While the contribution of RANKL–OPG in bone turnover mediated via systemic and local biologic agents has been well studied [2, 3], less is known of the contribution of these proteins to mechanically induced bone turnover. Several in vitro studies provide important insights into the potential role of mechanically regulated OPG and RANKL in modulating bone turnover in altered strain environments. Compressive mechanical loading of isolated PDL cells leads to a substantial upregulation of RANKL with little change or slight increase in OPG expression which in turn increases osteoclastogenesis when loaded cells are co-cultured with peripheral bone mononuclear cells [4, 5]. Also, conditioned media from osteoblasts subjected to microgravity show an increase in the

RANKL/OPG ratio, which is accompanied by increased osteoclastogenesis and bone resorption in mouse bone marrow cultures when compared to cells grown at 1 *g*. In contrast, dynamic tensile loading upregulates OPG mRNA and concentration of OPG in conditioned medium, while having little effect on the levels of RANKL in human PDL cells [6], and conditioned media of PDL cells subjected to cyclical tensile force inhibit osteoclastogenesis [7]. Similarly, human osteoblasts demonstrate increased OPG expression but also a decrease in soluble RANKL when subjected to cyclic tensile strain [8]. Moreover, osteoblasts cultured on artificial substrates and subjected to bending also demonstrate increased levels of OPG relative to RANKL [9]. Finally, ST-2 murine bone marrow stromal cells exposed to oscillating fluid flow show a maximal reduction in RANKL/OPG immediately after the end of flow with a significant increase in OPG and decrease in RANKL[10]. RAW 264.7 monocytes co-cultured with ST-2 cells and subjected to fluid flow showed a decrease in osteoclast formation when compared with control cells. Together, these studies demonstrate that different types of mechanical strains by differentially regulating OPG and RANKL result in important differences in the net osteolytic responses. Specifically, the findings suggest that while microgravity and cyclic compressive forces likely contribute to a net increase in osteolytic activity by enhancing the RANKL/OPG ratio, the reverse is true for cyclic tensile strain and oscillating fluid flow. While these in vitro studies may not precisely represent the complex nature of mechanical strains experienced by loaded bone in vivo, including that in the PDL during orthodontic tooth movement, they indicate that cells are capable of perceiving and responding differently to diverse strain histories.

Limited in vivo data also point to the role of RANKL and OPG in modulating mechanically mediated bone turnover. This includes the effects of the administration of recombinant human OPG in reversing the decrease in bone mineral content (BMC), bone mineral density (BMD), and bone strength back to normal levels in limbs of immobilized rats [11]. It has also been demonstrated that excess OPG actually impairs bone remodeling in a situation such as callus repair following fracture indicating that the ideal ratio of OPG to RANKL is dependent on the mechanical model being employed [12]. Finally, local OPG gene transfer to sites significantly diminishes while RANKL gene transfer significantly enhances orthodontic tooth movement possibly by respectively inhibiting or enhancing RANKL-mediated osteoclastogenesis [13, 14]. Orthodontic tooth movement is a well-utilized in vivo model for determining the contributions of various exogenous and endogenous agents to mechanically mediated bone modeling [15-19]. It results from the application of forces to teeth that cause bone resorption under pressure and bone deposition under tension. The entire process is based on bone turnover in which the bone surrounding the roots undergoes degradation and active reparative mechanisms as a response to orthodontic forces.

Recently, a fusion protein OPG-Fc and other RANKL inhibitors have been shown to reduce bone resorption systemically and preserve bone in a variety of clinical and preclinical disease settings. Examples include primary osteoporosis, Paget's disease, rheumatoid arthritis, hypercalcemia of malignancy, osteolytic metastases, postmenopausal bone loss, and periodontal disease [1, 20-27]. While the potential benefits of these RANKL inhibitors in systemic conditions resulting in significant bone

loss are evident, there are also possible uses for local RANKL inhibition such as during mechano-modulation of bone modeling during orthodontic tooth movement, where it is often necessary to minimize unnecessary movement of teeth. The stability of anchor teeth, which tend to inadvertently move during treatment, is a critical shortcoming in orthodontics. In order to combat this undesirable movement, orthodontists have developed several mechanical methods of improving anchorage. However, these have substantial limitations including the need for compliance, discomfort, cost or lack of efficacy [28, 29]. Given these disadvantages, a pharmacological approach aimed at utilizing the known biological mechanisms underlying tooth movement may provide an effective, non-compliant, non-visible means of anchorage. If the resorptive process of modeling during tooth movement can be inhibited, tooth movement may be inhibited as well. Accordingly, if OPG is involved in mechano-modulation of bone modeling, its local inhibition of RANKL may provide a novel pharmacological approach for preventing unneeded tooth movement that is highly desirable for preserving orthodontic anchorage.

In this study we tested the hypothesis that local delivery of OPG-Fc will inhibit mechanically induced bone modeling in a rat model of orthodontic tooth movement at the site of OPG-Fc delivery. The specific objectives of this study were to: (1) assess the magnitude of movement of molar and incisor teeth at sites closest and distant, respectively, to the administration of OPG-Fc; (2) quantify the bone resportive activity by histomorphometric assessment of osteoclasts; (3) determine the effects of OPG-Fc on bone density through micro-CT analysis; and (4) assay for serum levels of a bone resorption maker, TRAP-5b.

5.3. MATERIALS AND METHODS

5.3.1. Animals

A total of 39 male Sprague-Dawley rats (approximate weight 250–300 g) were utilized in this study. Thirty animals divided into groups of ten were subject to orthodontic forces in addition to volumetrically equivalent injections of 5.0 mg/kg human OPG-Fc (AMGEN, Inc., Thousand Oaks, CA), 0.5 mg/kg OPG-Fc, or phosphate-buffered saline (PBS) vehicle. Three animals received no appliances or injections and were sacrificed at baseline; three animals were vehicle-injected with no appliances, and three animals received high-dose OPG and no appliances. All injections were administered into the palatal mucosa adjacent to the mesial surface of the first molar teeth using 33-gauge microneedles (Hamilton Company, Reno, NV). The animals were evaluated at baseline, 3,7,10,14,17, and 21 days after appliance placement. All procedures were approved by the University of Michigan Committee of Use and Care of Animals. For baseline procedures including appliance placement, the animals were anaesthetized as described below.

5.3.2. Appliance placement

We utilized a previously established rat tooth movement model and appliance design (Fig. 3-C.1A) [30]. Animals were first placed under general anesthesia with ketamine (87 mg/kg) and xylazine (13 mg/kg) for initial appliance placement. A closed coil nickel-titanium spring (Sentalloy®, GAC, Ctr. Islip, NY) calibrated by an Instron Universal Testing Machine (Model 5565, Norwood, MA) providing a force of 54±2 g at 4 mm activation was connected between the maxillary first molar and maxillary central incisor

teeth with 0.010-in. steel ligatures. Previous studies have demonstrated that a 40–60 g level of force stimulated substantial molar tooth movement in rats [23, 30-34]. A nickel–titanium spring was used to provide a relatively constant force level over the course of the experiment.

For placement of springs, grooves were prepared along the distolingual line angles of the maxillary first molars to allow easier ligature placement as well as prevent the ligatures from slipping over the contact areas once the teeth started to move [30]. In addition, grooves were prepared on the facial, mesial, and distal surfaces of the maxillary central incisors to prevent the ligatures from dislodging from the teeth due to their lingual curvature and eruption pattern. After the ligatures were tied and cut, composite resin (Transbond XT Light Cure Adhesive Paste, 3M Unitek, Monrovia, CA) was placed over the wire to prevent slipping as well as pulpal irritation due to exposed dentin. Finally, the mandibular incisors were reduced to prevent appliance breakage.

5.3.3. Measurement of tooth movement

Tooth movement was measured as previously described, with minor modifications [14,19]. At each time point including baseline, polyvinylsiloxane (Dimension Garant 2 L Quick, 3M/ESPE, St. Paul, MN) impressions were taken of the maxillary arches. Following fabrication of precise stone models (Jade Stone, Whip Mix Corp., Louisville, KY), the occlusal tooth surfaces were scanned (Epson Expression 1680, Epson America, Inc., Long Beach, CA) adjacent to a 100 mm ruler and then magnified 100× using calibrated imaging software (Adobe Photoshop 7.0.1, Adobe Systems, Inc., San Jose,

CA). Using Adobe Photoshop's measuring tool, a single masked, calibrated examiner (ICC>0.972; 0.954 ≤ 95% confidence interval ≤ 0.983) made measurements from the distobuccal groove of the maxillary first molar to the most distal surface of the maxillary third molar at each time point. The amount of tooth movement was calculated as the difference between the pre-treatment, intra- and post-treatment measurements. In addition to molar movement, the amount of incisor retraction was also measured relative to the distal surface of the third molar teeth. Incisor position was measured from the mesiodistal center of each central incisor at the facial gingival margin. The amount of tooth movement was calculated as the difference between the measurements made during and at the end of treatment and the measurement at baseline. Given that maxillary growth also results in a change of incisor position relative to the third molar reference point, the amount of incisor retraction was calculated in terms of incisor position relative to that of untreated controls at day 21. The impressions did not include the incisors during the intra-study time points to avoid altering the springs involved in the promotion of tooth movement. Therefore, since the untreated controls showed a mean of 1.42 mm of forward incisor displacement, this value was added to all values of incisor movement derived from the models of the experimental animals.

5.3.4. Biopsy harvest and histological preparation

The animals were sacrificed by CO_2 euthanasia at 21 days following appliance placement. After taking final impressions, block biopsies of the right and left maxillae were harvested, immediately fixed and stored in 10% formalin for 48 h, and then transferred to 70% ethanol. Samples were divided randomly (right and left) so that half the samples

were imaged using micro-computed tomography and the other half prepared for histology. Samples used for histology were decalcified with 10% vol./vol. EDTA and the embedded in paraffin. Sagittal sections (4–5 μm thick) were obtained of the mesial root of the maxillary first molar. The mesial root was chosen because it is the largest of the first molar's five roots, is in approximately the same plane as the applied force and is most commonly evaluated in tooth movement studies [30, 35-37]. The sections were stained with hematoxylin and eosin (H & E) for descriptive histology.

5.3.5. Immunohistochemical analysis

Tartrate-resistant acid phosphatase (TRAP) immunohistochemical staining was performed to identify and quantify osteoclasts. A minimum of six, randomly selected midsagittal sections per animal were deparaffinized and then incubated in DakoCytomation Target Retrieval Solution (Dako Corp., Capinteria, CA) for 30 m. TRAP immunohistochemical staining was performed with a goat ABC Staining System kit (sc-2023; Santa Cruz Biotechnology) and anti-TRAP antibody (sc-30833; Santa Cruz Biotechnology).

Images of coded specimens were captured using a Nikon Eclipse 50i microscope (Nikon, Inc., Melville, NY) fitted with a Nikon Digital Sight DS U1 camera (Nikon, Inc., Melville, NY) for analysis using Image Pro Plus™ software (Media Cybernetics, Silver Spring, MD). A single masked, calibrated examiner examined the images and quantified tension side, compression side, and total osteoclasts (TRAP-positive cells) present on the alveolar bone surface adjacent to the entire mesial root.

5.3.6. Micro-computed tomography

Micro-CT analysis was done to quantify alveolar bone in the proximity of the first molar roots. Regions of fixed, non-demineralized rat maxillae were scanned in de-ionized water using a cone beam micro-CT system (GE Healthcare, London, ON, Canada). Each scan was reconstructed at a mesh size of 18 μm × 18 μm × 18 μm, allowing a three-dimensional digitized image to be generated for each specimen (Fig. 5.1B). Using GE Healthcare Microview Analysis+ software, the images were rotated into a standard orientation and threshold to distinguish the degree of mineralization of tissues such as bone, tooth roots and tooth crowns. For each specimen, a gray voxel value histogram was generated to determine an optimal threshold value. An average of the individual threshold values was calculated and a representative value was used to threshold all images.

Measurements of the bone volume fraction (BVF) in the first molar furcation area were carried out as previously described [38]. The furcation area and root apex was chosen because they provide reproducible, morphological landmarks. Briefly, the most mesial and distal roots of the first molar were selected as endpoint landmark borders. Two-dimensional regions of interest (ROIs) were then drawn at regular intervals (mean =144 μm) in order to quantify tooth-supporting alveolar bone.

Systemic measure of osteoclast activity was determined by assaying for TRAP-5b by ELISA (RatTRAP Assay, SBA Sciences, Finland), in accordance with manufacturer's instructions. TRAP-5b is specific for osteoclast activity thus providing a marker of bone resorption [40].

5.3.7. Statistical analysis

Descriptive statistics (mean, standard error) for each parameter were calculated for all groups. Each animal was used as the experimental unit. Comparisons of tooth movement were made using repeated measures, analysis of variance and Tukey's HSD post-hoc comparison. Osteoclast number, bone volume fraction, serum OPG, and serum TRAP-5b comparisons were made using analysis of variance (ANOVA) and Tukey's HSD post-hoc comparison. Kruskal–Wallis analysis of ranks was used to compare ratios of incisor retraction to molar movement. Differences with $p<0.05$ were considered statistically significant.

5.4. RESULTS

5.4.1. Animal status

Appliance placement and injections did not appear to hinder the animals' ability to thrive. There were no significant differences in weight gain among the groups. The mean + SD starting weight of all animals at baseline was 272.6±13.4 g. At 21 days, the animals weighed 372.0±25.8 g, 377.4±15.8 g, and 353.5±25.5 g in the vehicle, 0.5 mg/kg OPG-Fc, and 5.0 mg/kg OPG-Fc groups, respectively. There was 100% appliance success rate as no tooth movement appliances broke or needed to be replaced over the 3-week experimental period.

5.4.2. Tooth movement

Local delivery of OPG-Fc resulted in a substantial decrease in mesial movement of the first molar tooth when compared to vehicle-injected control animals (Fig. 5.2A). At day 7, there was a significant decrease in molar movement in both the 0.5 mg/kg OPG-Fc group (0.15±0.02 mm, $p<0.05$) and 5.0 mg/kg OPG-Fc group (0.14±0.02 mm, $p<0.01$) when compared to controls (0.27±0.03 mm). However, at this time-point there was no significant difference in amount of molar movement between groups receiving the two doses of OPG-Fc. By day 14, not only was there a significant decrease in mesial molar movement in the low (0.37 ± 0.05 mm, $p<0.05$) and high (0.16±0.03 mm, $p<0.001$) OPG groups compared to controls (0.54±0.05 mm) but there was also a significant difference between the low- and high-dose OPG groups $p<0.05$). Only the high-dose OPG group (0.20±0.03 mm, $p< 0.001$) showed a significant decrease in molar movement at day 21

compared to controls (0.93±0.07 mm). The high-dose OPG group also had significantly less ($p< 0.001$) mesial molar movement than the low-dose OPG group (0.75±0.10 mm). Using the data reported in Figure. 5.2A to determine percentages of tooth movement, it was noted that rats administered a dose of 5.0 mg/kg OPG-Fc demonstrated only 54.3%, 29.5%, and 21.3% of the total mesial molar movement compared to that observed in control rats at days 7,14, and 21, respectively. These differences were all statistically significant. Rats receiving 0.5 mg/kg OPG-Fc had a statistically significant 56.2% and 68.2% of the molar movement relative that that in control rats at days 7 and 14, respectively. At day 21, animals treated with 0.5 mg of OPG-Fc did not demonstrate significant molar tooth movement compared to controls. At days 14 and 21, the 5.0 mg/kg OPG-Fc group showed significantly less ($p<0.05$) percent molar movement compared to the 0.5 mg/kg OPG-Fc group.

The amount of incisor retraction appeared also to be inhibited dose dependently (Fig. 5.2C). Animals without active springs demonstrated 1.42±0.06 mm of forward maxillary incisor movement over the 3-week experimental time period. The vehicle-injected animals with active springs showed 2.17 ± 0.05 mm of incisor retraction relative to the untreated controls corrected for the abovementioned growth-associated anterior movement of the incisors. The 0.5 mg/kg OPG-Fc-injected group showed significantly less incisor retraction (1.53±0.03 mm, $p<0.0l$) than the vehicle-injected group. Likewise, the 5.0 mg/kg OPG-Fc group showed significantly less incisor retraction (1.05±0.03 mm, $p<0.0l$) than either the vehicle or 0.5 mg/kg OPG-Fc-injected animals. No tooth

movement was noted for the three groups not receiving appliances (i.e., the no-treatment control, vehicle-control or high-dose OPG treatment control, data not shown).

In order to evaluate the relative effect of OPG on movement of the first molars and incisors, the ratio of incisor to molar tooth movement was calculated (Fig. 5.2D). In the vehicle-injected rats, the incisors were retracted 2.3 mm for every millimeter of anchorage loss at the first molar. Injecting 0.5 mg/kg OPG-Fc, allowed for only 2.0 mm of incisor retraction for every millimeter of anchorage loss. Finally, the 5.0 mg/kg OPG-Fc group demonstrated 5.2 mm ($p<0.001$) of incisor retraction for every millimeter of molar anchorage loss.

5.4.3. Descriptive histology

The control and low-dose OPG groups showed many osteoclasts, inflammatory cells, and areas of bone resorption (Fig. 5.3). In contrast, very few osteoclasts and areas of bone resorption were found in the high-dose OPG group. The periodontal ligament appeared to be normal in all groups and there was no evidence of ankylosis. Isolated areas of root resorption were noted but did not appear to correlate with any particular treatment group (data not shown).

5.4.4. Immunohistochemical analysis

Osteoclasts were enumerated along the compression and tension sides of the mesial tooth roots of the maxillary first molars (Fig. 5.4). The 5.0 mg/kg OPG-Fc group showed significantly fewer osteoclasts (3.2±1.7) than either the vehicle-(23.3±2.9, $p<0.001$) or

0.5 mg/kg OPG-Fc-injected(16.0±4.2, $p<0.05$) groups in terms of osteoclasts along the compression side of the mesial root (Fig. 5.4A). Along the tension side, the high-dose OPG group also showed fewer osteoclasts (3.1±1.2) compared to the low-dose OPG group (13.4±2.5, $p<0.05$), but was not significantly different than controls (8.9±2.0) (Fig. 3-C.4B). Finally, the high-dose OPG group had significantly less total osteoclasts (6.3±2.8) than either the control (32.2±3.3, $p<0.00l$) or the low-dose OPG (29.4±4.7, $p<0.001$) groups (Fig. 5.4C). One animal in each of the low- and high-dose OPG groups could not be evaluated because the tissue sections demonstrated histological artifacts abrogating analysis.

5.4.5. Micro-computed tomography

BVF was measured in the first molar furcation area. Compared to the baseline group that received no treatment (0.524 ± 0.020), there were no significant differences in BVF (Fig. 5.5) in the vehicle (0.515±0.029) and 0.5 mg/kg OPG (0.374±0.133) groups. The 5.0 mg/kg OPG group (0.666±0.049), however, demonstrated a significant ($p<0.001$) increase in BVF compared to all other groups. In addition, the low-dose OPG group showed significantly ($p<0.01$) less BVF than the control group. One animal in the low-dose OPG group was excluded because the specimen was damaged during biopsy retrieval.

5.4.6. ELISA of serum TRAP-5b

At baseline, animals showed 1.9±0.4, 1.7±0.3, and 1.5 ± 0.2 U/L of serum TRAP-5b in the control, low-dose OPG, and high-dose OPG groups, respectively (fig. 5.6). By day 7,

the high-dose group (0.0±0.0 U/L) demonstrated a significant decrease (p<0.05) compared to controls (1.2±0.2 U/L). The low-dose group showed a non-significant decrease (0.5±0.4 U/L). At day 14, the high-dose group remained significantly lower (0.3±0.2 U/L, p<0.05) than the control group (2.1±0.5 U/L). Serum TRAP-5b levels in the low-dose group rebounded to 2.5 ± 0.6 U/L. At day 21, the animals demonstrated 1.5±0.3, 2.2±0.5, and0.9 ± 0.4 U/L of serum TRAP-5b in the control, low-dose OPG, and high-dose OPG groups, respectively. The differences were not statistically significant.

5.5. DISCUSSION

The binding of RANKL to RANK is critical for osteoclastogenesis and bone resorption. By preventing this binding, the soluble decoy receptor OPG inhibits osteoclast formation, activation, and survival [41]. Considering OPG is a competitive inhibitor, the ratio of RANKL to OPG ultimately is responsible for the activation of RANK and inducing osteoclast progenitor cells to form mature osteoclasts. At the cellular and molecular levels, tooth movement is the result of the interaction between bone-forming osteoblasts and bone-resorbing osteoclasts. Given the critical role osteoclasts play in tooth movement, it follows that the RANK/RANKL/OPG pathway is likely to be critical in this process. Indeed, it has been shown that application of orthodontic forces results in the expression of RANKL protein in osteoblasts, osteocytes, fibroblasts, and osteoclasts [42]. In our studies, we utilized the knowledge of the basic biologic mechanisms of osteoclastogenesis and the important role played by the OPG–RANKL axis in osteoclast function to test the hypothesis that OPG participates in mechano-modulation of osteolysis to diminish orthodontic tooth movement and could therefore serve as a biologic mediator for enhancing orthodontic anchorage.

Bearing in mind the shortcomings of traditional orthodontic anchorage approaches, a number of different groups have attempted to alter rates of tooth movement with a variety of bioactive molecules. Bisphosphonates [15, 19], nitric oxide synthase inhibitor [17], echistatin [16], and matrix metallo-proteinase inhibitors [18] have all been shown to decrease tooth movement. Bisphosphonates are not indicated for orthodontic use currently, and osteonecrosis of the jaw has recently become a concern with

bisphosphonate therapy [43, 44]. Bisphosphonates incorporate directly into bone where they reside for many years, and their effects are not readily reversible. In contrast, RANKL inhibitors including OPG are not incorporated into bone and have reversible effects on bone resorption [23]. As such, RANKL inhibitors may be desirable when transient osteoclast suppression is desirable in clinical situations such as with tooth anchorage.

While multiple studies have demonstrated the ability to alter rates of tooth movement, the agents used affect osteoclasts indirectly rather than directly targeting the RANK/RANKL/OPG pathway. Using an *in vivo* gene transfer approach, molar movement was decreased by 47.8% ($p<0.001$) after 3 weeks of twice weekly OPG plasmid DNA injections [14]. In contrast to RANKL plasmid DNA injections that resulted in 31.6% ($p<0.01$) more molar movement [13]. These two gene therapy studies showed the potential of directly targeting this pathway in altering tooth movement.

Using the recombinant fusion protein, OPG-Fc, we successfully inhibited molar movement by 78.7% ($p<0.001$) with a 5.0 mg/kg twice weekly local injection protocol. Even with a 10-fold reduction in dose (0.5 mg/kg), there was still a significant reduction ($p<0.05$) in molar movement until day 21. It is likely that the 0.5 mg/kg OPG-Fc-treated animals' inability to maintain anchorage throughout the study was due to an inadequate dose compared to the level of RANKL expression that is induced during tooth movement. As we were using a human protein in a rat, we used higher and more frequent dosing than would likely be required for a human in order to overcome the animal's immune response

to foreign human OPG-Fc. In a human study, using the same protein, a single subcutaneous dose (3.0 mg/kg) of OPG-Fc demonstrated a half-life of 6–7 days and remained effective for at least 30 days [22]. In addition, AMG 162 [21], a specific fully human monoclonal antibody to RANKL based on OPG, has demonstrated an 81% suppression in bone turnover six months after a single injection of 3.0 mg/kg. However, this human antibody cannot be studied in the rat model to directly compare its efficacy to humans.

It is also of interest to note that the majority (57%) of the total molar movement in both OPG groups occurred within the first 3 days, corresponding with the displacement phase of tooth movement. The displacement phase is the initial movement caused by physical compression of the viscoelastic periodontal ligament. As it is not the result of tissue remodeling, the amount of movement in this phase is dependent on its biophysical limitations. During the remaining phases (days 3–21), the high OPG group demonstrated almost no additional molar movement.

Considering the substantial decrease in molar tooth movement, it is likely that local OPG-Fc injections were effectively inhibiting osteoclastogenesis. This was indeed the case as the animals in the high OPG group demonstrated 86% ($p< 0.001$) fewer osteoclasts along the compression side of the mesial root when compared to controls. The low-dose OPG group also showed a non-significant trend towards decreased osteoclasts.

One of the advantages of the mesial molar movement model that was used in the present study is that incisor retraction also can be measured. This allowed for evaluation of the effects of OPG on neighboring teeth. While there was a decreased rate of incisor retraction with increased levels of OPG, the overall treatment efficacy as measured by the ratio of incisor retraction to molar anchorage loss was greatly improved in the 5.0 mg/kg OPG-Fc group (incisor:molar movement=5.2:1) compared to the low-dose OPG group (2.0:1) or controls (2.3:1). As differentially regulating rates and magnitudes of tooth movement is the ultimate goal in maintaining orthodontic anchorage, this was an encouraging observation. This finding also demonstrates relative localization of the effects of the OPG-Fc-injected in proximity to the molar teeth. While these findings are promising, future research is recommended in order to determine the optimal dose regimen (quantity/frequency) that permits the greatest amount of incisor retraction with the least molar movement, and optimal time-release methods for administering OPG-Fc to obtain highly localized and long-term pharmacologic effects.

Using three-dimensional imaging, we were also able to evaluate the quantity of tooth-supporting alveolar bone. Not only did the animals in the high OPG group show greater BVF than the control and low OPG groups but they were also actually higher than the baseline sacrificed animals that never received any tooth movement appliances or tooth movement (Fig. 5.5). The modest but significant reduction in BVF associated with the low dose of OPG-Fc is consistent with the possibility that anti-human OPG-Fc antibodies that were induced by repeated injections resulted in some cross-reactive neutralization of endogenous rat OPG as well. Rat and human OPG are highly homologous and cross-

reactive antibodies have been observed in previous rat studies (P. Kostenuik, personal communication). The potential for this phenomenon in the current study is supported by data obtained at the end of the study, wherein serum TRAP-5b values were slightly elevated in the low-dose OPG-Fc group, drug levels were not different from vehicle controls, and BVF was reduced. It is likely that this low dose produced pharmacologic effects for the first half of the study, followed by rapid immune-related clearance of the drug, and possible neutralization of endogenous OPG at the end of the study.

While the low-dose group had no significant effect on serum TRAP-5b, there was significant suppression of this resorption marker in the high-dose group (Fig. 5.6). It is likely that the reduced TRAP-5b suppression with low-dose OPG is related to an immune response to the foreign protein. In other words, it is likely that there was significant serum TRAP-5b suppression during the first part of the study, but at some point (probably between days 10 and 14), the immune response was sufficient to clear or neutralize the drug. With the high-dose group, an immune response also probably occurred but enough protein was delivered to overwhelm the immune response and maintain therapeutic circulating levels of OPG-Fc to effectively suppress bone resorption. By 21 days the TRAP-5b suppression was reduced, indicating that the immune response was likely eventually sufficient to neutralize even the high dose administration.

The effects of the local gingival delivery method employed in this study were not entirely contained as demonstrated by TRAP-5b assays (Fig. 3-C.6). Given its transient effect, the minimal safety concerns with systemic RANKL inhibition, and potential improvement in

bone mineral density, this result does not appear to be of significant concern [23, 24]. However, the targeted, primarily localized effects of OPG particularly with the high-dose group were demonstrated for therapeutic tooth anchorage. This phenomenon suggests that local OPG concentrations at the site of anchorage may have been higher than at other sites, perhaps due to simple diffusion of the protein within the gingivae.

Inhibition of tooth movement using pharmacological anchorage could have many applications for orthodontics and dentistry beyond simply maintaining molar anchorage during incisor/canine retraction and may have benefits in molar distalization, molar protraction, vertical anchorage of posterior teeth and other applications where dental anchorage is critical for a favorable functional and esthetic result. Overall, this study demonstrates for the first time that local delivery of the recombinant RANKL inhibitor, OPG, effectively inhibits mechanically induced osteoclastogenesis resulting in improved bone quantity, orthodontic anchorage, and would likely lead to enhanced treatment efficacy.

5.6. FIGURES

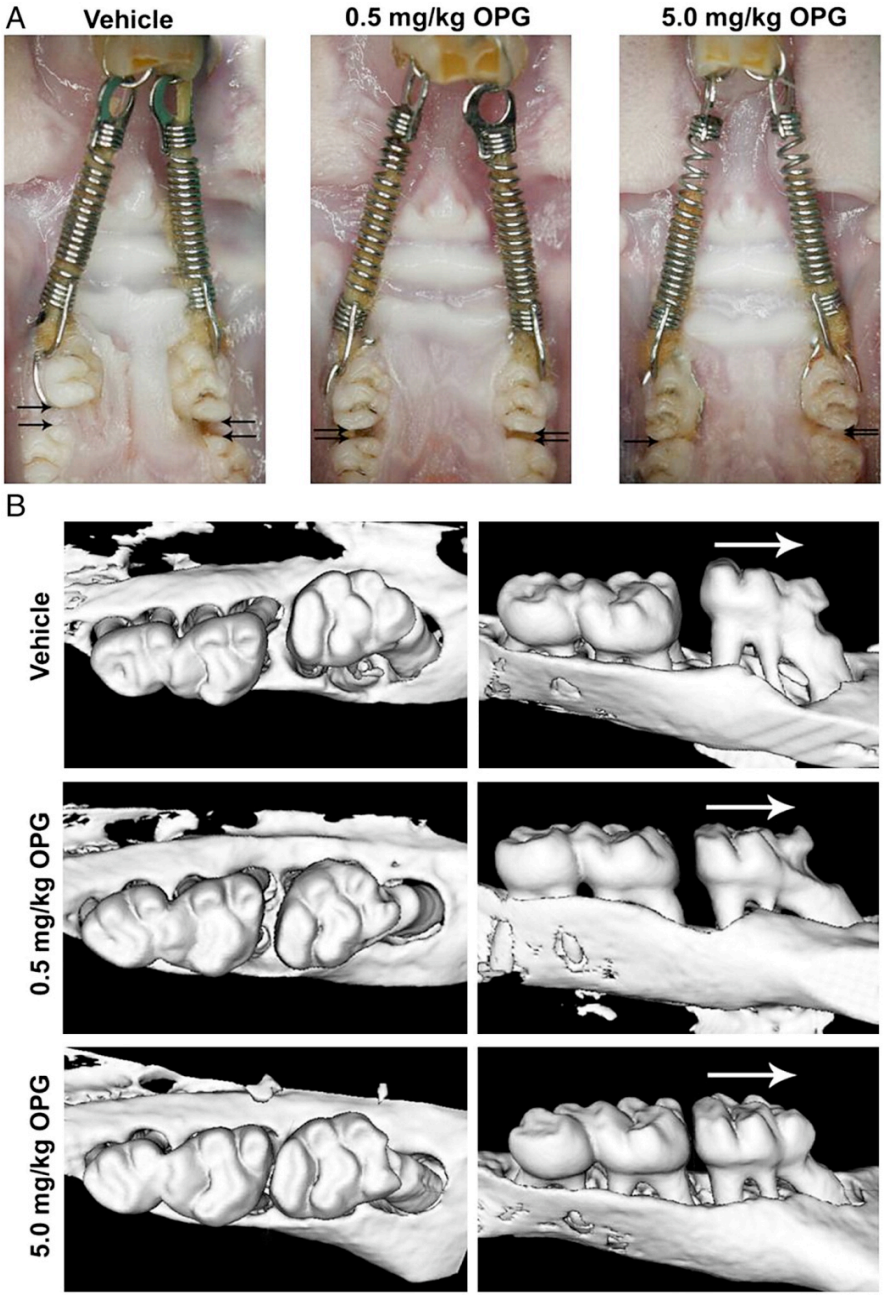

Figure 5.1. (A) Intraoral photographs of orthodontic appliances in place at day 21 prior to sacrifice. Animals received twice weekly injections of vehicle, 0.5 mg/kg OPG-Fc, or 5.0 mg/kg OPG-Fc into the mucosa just mesial to the maxillary first molars. Note the amount of space visible between the first and second molar teeth. (B) Three-dimensional coronal and sagittal micro-computed tomography views of the same animals shown in

panel A. Note the interdental distance visible between the first and second molar teeth as well as the differences in bone quantity around the first molars. Arrows indicate 2-D force direction.

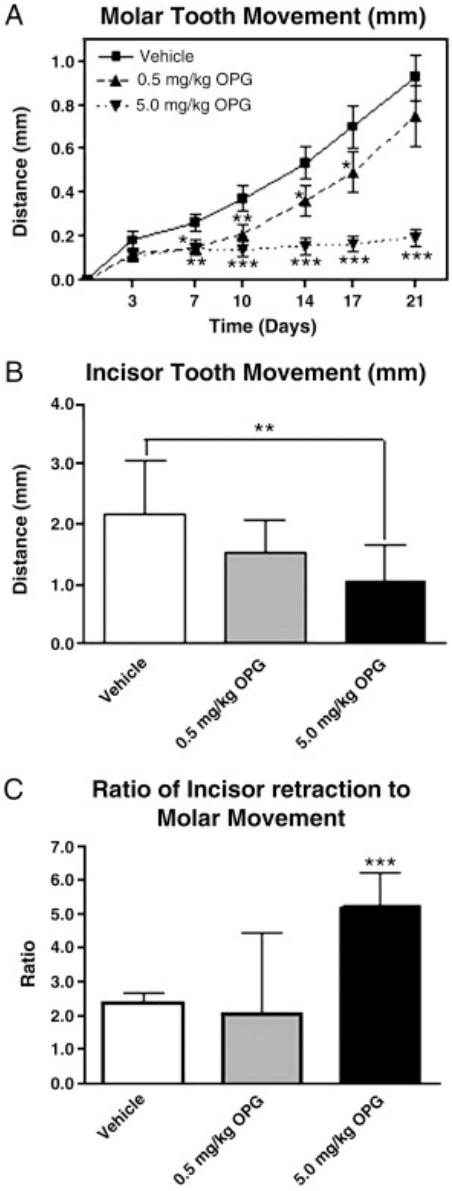

Figure 5.2. Inhibition of tooth movement by local delivery of OPG-Fc. (A) Molar tooth movement over the course of time in vehicle, 0.5 mg/kg OPG-Fc, and 5.0 mg/kg OPG-Fc injected groups. No tooth movement was noted in sham control animals (inactive spring) (data not shown). (B) Incisor retraction measured at day 21. (C) Ratio of incisor retraction to molar tooth movement at day 21. All results are expressed as the

mean ± SEM, $n = 10$: $*p < 0.05$; $**p < 0.01$; $***p < 0.001$. Comparisons made versus time-matched vehicle groups.

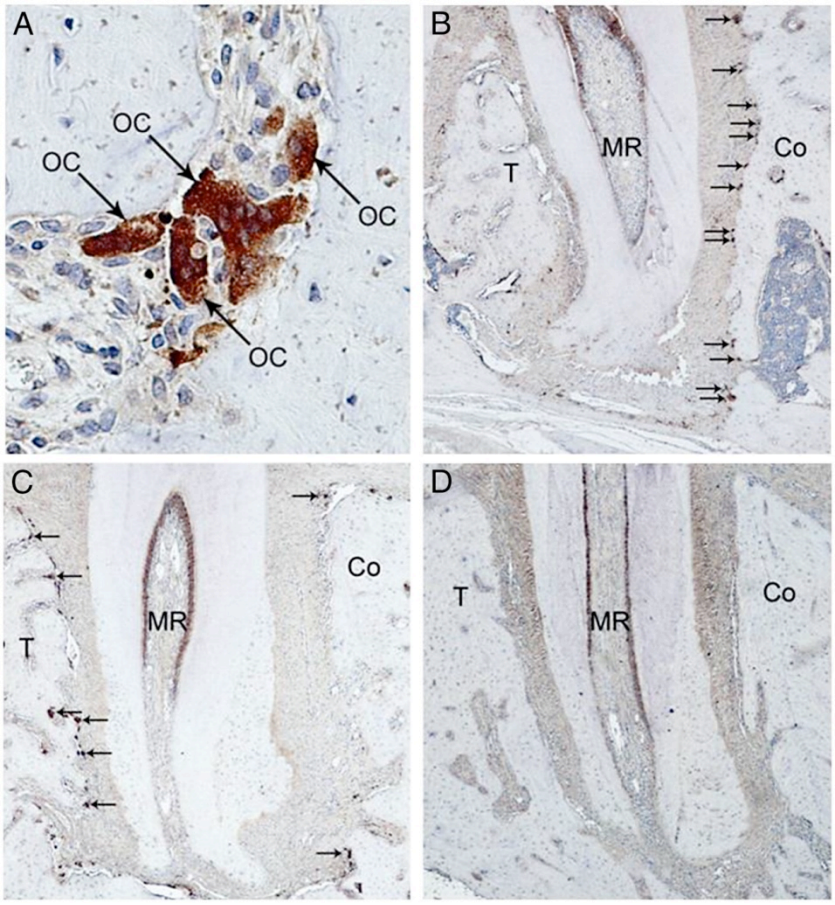

Figure 5. 3. TRAP-stained histological sections (4–5 μm) counterstained with hematoxylin taken from the mesial tooth root of the maxillary first molar. (A) TRAP-positive multinucleated osteoclasts (40× magnification); (B) control group (4× magnification); (C) low-dose OPG group (4× magnification); (D) high-dose OPG group (4× magnification), which lacks osteoclasts. MR, mesial root; Co, compression side alveolar bone; T, tension side alveolar bone; OC, osteoclast. Arrows indicate osteoclasts.

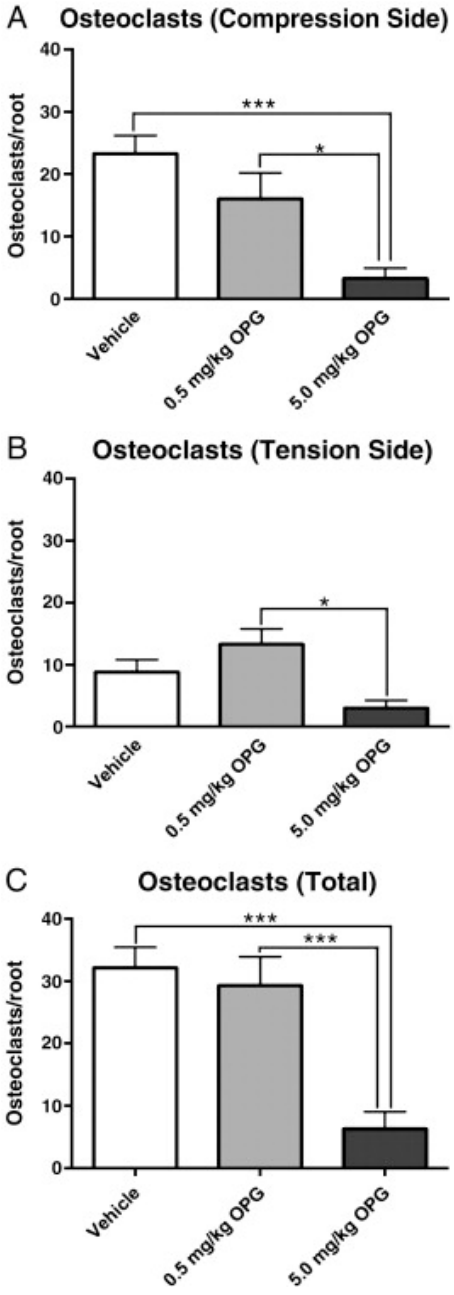

Figure 5. 4. Osteoclasts per root surface on the tooth compression surface (A), tension side (B), and total osteoclasts (C) along the alveolar bone adjacent to the mesial root of the maxillary first molar. All results are expressed as the mean ± SEM, $n = 10$ (vehicle), 9 (low-dose OPG, high-dose OPG): $*p < 0.05$; $***p < 0.001$. Comparisons made versus time-matched groups.

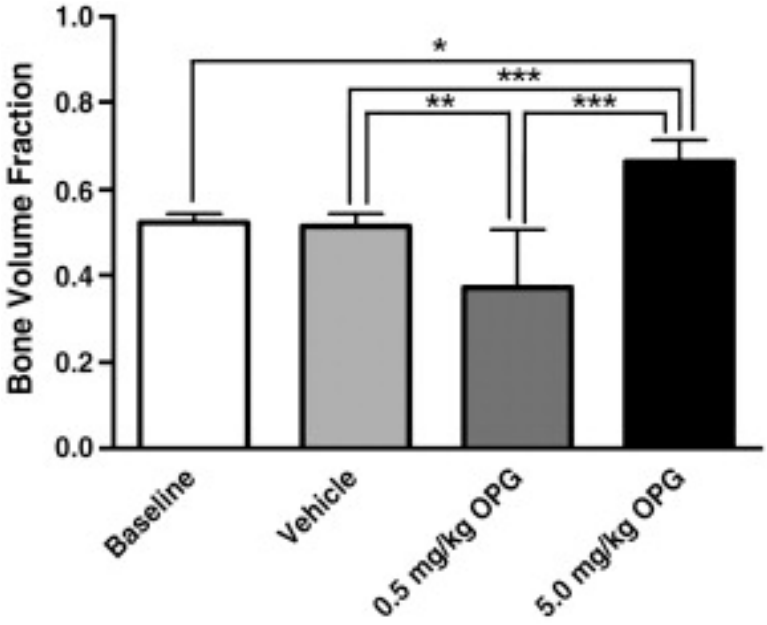

Figure 5. 5. Comparison of bone volume fraction measured from the furcation area to tooth root apex of the maxillary first molar with micro-computed tomography. Specimens were placed on a rotating stage allowing polychromatic X-rays to penetrate the sample, pass through an image intensifier, and be captured by a CCD camera, producing 2-D slices of 18 μm thickness. These cross-sectional images were then reconstructed into a 3-D structure by GE Healthcare reconstruction utility. Results are expressed as the mean ± SD, $n = 3$ (baseline), $n = 10$ (vehicle, high-dose OPG), $n = 9$ (low-dose OPG): $*p < 0.05$; $**p < 0.01$; $***p < 0.001$. Comparisons made versus time-matched groups.

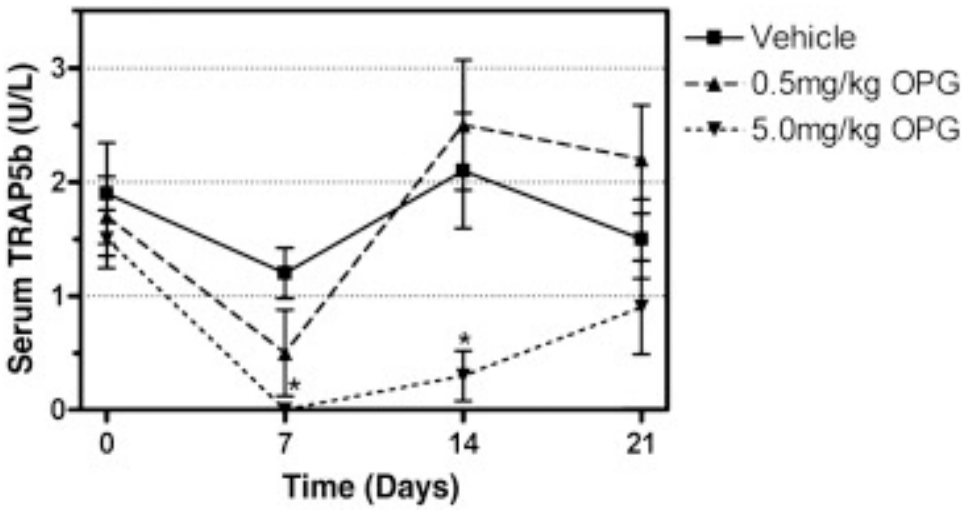

Figure 5. 6. Concentrations of TRAP-5b in serum as measured by ELISA. Blood was drawn from the lateral tail vein at days 0, 7, 14, and 21 prior to the next administration of OPG-Fc or vehicle. Results are expressed as the mean ± SEM, $n = 10$; $*p < 0.05$. Comparisons made versus time-matched groups.

5.7. REFERENCES

1. Simonet WS, Lacey DL, Dunstan CR, Kelley M, Chang MS, Luthy R, et al. Osteoprotegerin: a novel secreted protein involved in the regulation of bone density. *Cell.* 1997;89:309–19.

2. Kostenuik PJ. Osteoprotegerin and RANKL regulate bone resorption, density, geometry and strength. *Curr Opin Pharmacol.* 2005;5:618–25.

3. Kostenuik PJ, Shalhoub V. Osteoprotegerin: a physiological and pharmacological inhibitor of bone resorption. *Curr Pharm Des.* 2001;7:613–35.

4. Kanzaki H, Chiba M, Shimizu Y, Mitani H. Periodontal ligament cells under mechanical stress induce osteoclastogenesis by receptor activator of nuclear factor κB ligand up-regulation via prostaglandin E_2 synthesis. *J Bone Miner Res.* 2002;17:210–20.

5. Nishijima Y, Yamaguchi M, Kojima T, Aihara N, Nakajima R, Kasai K. Levels of RANKL and OPG in gingival crevicular fluid during orthodontic tooth movement and effect of compression force on releases from periodontal ligament cells in vitro. *Orthod Craniofac Res.* 2006;9:63–70.

6. Tsuji K, Uno K, Zhang GX, Tamura M. *J Bone Miner Metab.* Vol. 22. 2004. Periodontal ligament cells under intermittent tensile stress regulate mRNA expression of Osteoprotegerin and tissue inhibitor of matrix metalloprotease-1 and -2; pp. 94–103.

7. Kanzaki H, Chiba M, Sato A, Miyagawa A, Arai K, Nukatsuka S, et al. Cyclical tensile force on periodontal ligament cells inhibits osteoclastogenesis through OPG induction. *J Dent Res.* 2006;85:457–62.

8. Kusumi A, Sakaki H, Kusumi T, Oda M, Narita K, Nakagawa H, et al. Regulation of synthesis of Osteoprotegerin and soluble receptor activator of nuclear factor-kappaB

ligand in normal human osteoblasts via the p38 mitogen-activated protein kinase pathway by the application of cyclic tensile strain. *J Bone Miner Metab.* 2005;23:373–81.

9. Saunders MM, Taylor AF, Du C, Zhou Z, Pellegrini VD, Jr, Donahue HJ. Mechanical stimulation effects on functional end effectors in osteoblastic MG-63 cells. *J Biomech.* 2006;39:1419–27.

10. Kim CH, You L, Yellowley CE, Jacobs CR. Oscillatory fluid flow-induced shear stress decreases osteoclastogenesis through RANKL and OPG signaling. *Bone.* 2006;39(5):1043–7.

11. Ichinose Y, Tanaka H, Inoue M, Mochizuki S, Tsuda E, Seino Y. Osteoclastogenesis inhibitory factor/osteoprotegerin reduced bone loss induced by mechanical unloading. *Calcif Tissue Int.* 2004;75:338–43.

12. Ulrich-Vinther M, Andreassen TT. Osteoprotegerin treatment impairs remodeling and apparent material properties of callus tissue without influencing structural fracture strength. *Calcif Tissue Int.* 2005;76:280–6.

13. Kanzaki H, Chiba M, Arai K, Takahashi I, Haruyama N, Nishimura M, et al. Local RANKL gene transfer to the periodontal tissue accelerates orthodontic tooth movement. *Gene Ther.* 2006;13:678–85.

14. Kanzaki H, Chiba M, Takahashi I, Haruyama N, Nishimura M, Mitani H. Local OPG gene transfer to periodontal tissue inhibits orthodontic tooth movement. *J Dent Res.* 2004;83:920–5.

15. Adachi H, Igarashi K, Mitani H, Shinoda H. Effects of topical administration of a bisphosphonate (risedronate) on orthodontic tooth movement in rats. *J Dent Res.* 1994;73:1478–86.

16. Dolce C, Vakani A, Archer L, Morris-Wiman JA, Holliday LS. Effects of echistatin and an RGD peptide on orthodontic tooth movement. *J Dent Res.* 2003;82:682–6.

17. Hayashi K, Igarashi K, Miyoshi K, Shinoda H, Mitani H. Involvement of nitric oxide in orthodontic tooth movement in rats. *Am J Orthod Dentofacial Orthop.* 2002;122:306–9.

18. Holliday LS, Vakani A, Archer L, Dolce C. Effects of matrix metalloproteinase inhibitors on bone resorption and orthodontic tooth movement. *J Dent Res.* 2003;82:687–91.

19. Igarashi K, Mitani H, Adachi H, Shinoda H. Anchorage and retentive effects of a bisphosphonate (AHBuBP) on tooth movements in rats. *Am J Orthod Dentofacial Orthop.* 1994;106:279–89.

20. Bekker PJ, Holloway D, Nakanishi A, Arrighi M, Leese PT, Dunstan CR. The effect of a single dose of Osteoprotegerin in postmenopausal women. *J Bone Miner Res.* 2001;16:348–60.

21. Bekker PJ, Holloway DL, Rasmussen AS, Murphy R, Martin SW, Leese PT, et al. A single-dose placebo-controlled study of AMG 162, a fully human monoclonal antibody to RANKL, in postmenopausal women. *J Bone Miner Res.* 2004;19:1059–66.

22. Body J-J, Greipp P, Coleman RE, Facon T, Geurs F, Fermand J-P, et al. A Phase I study of AMGN-0007, a recombinant Osteoprotegerin construct, in patients with multiple myeloma or breast carcinoma related bone metastases. *Cancer.* 2003;97:887–92.

23. Capparelli C, Morony S, Warmington K, Adamu S, Lacey DL, Dunstan CR, et al. Sustained antiresorptive effects after a single treatment with human recombinant Osteoprotegerin (OPG): a pharmacodynamic and pharmacokinetic analysis in rats. *J Bone Miner Res.* 2003;18:852–8.

24. Kostenuik PJ, Bolon B, Morony S, Daris M, Geng Z, Carter C, et al. Gene therapy with human recombinant Osteoprotegerin reverses established osteopenia in ovariectomized mice. *Bone.* 2004;34:656–64.

25. Morony S, Capparelli C, Lee R, Shimamoto G, Boone T, Lacey DL, et al. A chimeric form of Osteoprotegerin inhibits hypercalcemia and bone resorption induced by IL-1β, TNF-α, PTH, PTHrP, and $1,25(OH)_2D_3$. *J Bone Miner Res.* 1999;14:1478–85.

26. Schett G, Redlich K, Hayer S, Zwerina J, Bolon B, Dunstan CR, et al. Osteoprotegerin protects against generalized bone loss in tumor necrosis factor-transgenic mice. *Arthritis Rheum.* 2003;48:2042–51.

27. Teng Y-TA, Nguyen HQ, Gao X, Kong Y-K, Gorczynski RM, Singh B, et al. Functional human T-cell immunity and Osteoprotegerin ligand control alveolar bone destruction in periodontal infection. *J Clin Invest.* 2000;106:R59–67.

28. Bondemark L, Thornéus J. Anchorage provided during intra-arch distal molar movement: a comparison between the Nance appliance and a fixed frontal bite plane. *Angle Orthod.* 2005;75:437–43.

29. Zablocki H. *The effect of the transpalatal arch on anchorage in extraction treatment.* Ann Arbor: Unpublished Master's Thesis, Department of Orthodontics & Pediatric Dentistry, University of Michigan; 2005.

30. Leiker BJ, Nanda RS, Currier GF, Howes RI, Sinha PK. The effects of exogenous prostaglandins on orthodontic tooth movement in rats. *Am J Orthod Dentofacial Orthop.* 1995;108:300–88.

31. Bridges T, King GJ, Mohammed A. The effect of age on tooth movement and mineral density in the alveolar tissues of the rat. *Am J Orthod Dentofacial Orthop.* 1988;93:245–50.

32. King GJ, Fischlschweiger W. The effect offeree magnitude on extractable bone resorptive activity and cemental watering in orthodontic tooth movement. *J Dent Res.* 1982;61:775–9.

33. King GJ, Keeling SD, McCoy EA, Ward TH. Measuring dental drift and orthodontic tooth movement in response to various initial forces in adult rats. *Am J Orthod Dentofacial Orthop.* 1991;99:456–65.

34. Rody WJJ, King GJ, Gu G. Osteoclast recruitment to sites of compression in orthodontic tooth movement. *Am J Orthod Dentofacial Orthop.* 2001;120:477–89.

35. Kalia S, Melsen B, Verna C. Tissue reaction to orthodontic tooth movement in acute and chronic corticosteroid treatment. *Orthod Craniofacial Res.* 2004;7:26–34.

36. Seifi M, Eslami B, Saffar AS. The effect of prostaglandin E_2 and calcium gluconate on orthodontic tooth movement and root resorption in rats. *Eur J Orthod.* 2003;25:199–204.

37. Sekhavat AR, Mousavizadeh K, Pakshir HR, Aslani FS. Effect of misoprostol, a prostaglandin E_1 analog, on orthodontic tooth movement in rats. *Am J Orthod Dentofacial Orthop.* 2002;122:542–7.

38. Park C, Abramson Z, Taba M, Jr, Jin Q, Chang J, Kreider J, et al. Three-dimensional micro-computed tomographic imaging of alveolar bone in experimental bone loss and repair. *J Periodontol.2007* ;78(2):273-81

40. Halleen JM, Alatalo SL, Suominen H, Cheng S, Janckila AJ, Vaananen HK. Tartrate-resistant acid phosphatase 5b: a novel serum marker of bone resorption. *J Bone Miner Res.* 2000;15:1337–45.

41. Bolon B, Campagnuolo G, Feige U. Duration of bone protection by a single osteoprotegerin injection in rats with adjuvant-induced arthritis. *Cell Mol Life Sci.* 2002;59:1569–76.

42. Shiotani A, Shibasaki Y, Sasaki T. Localization of receptor activator of NFkappaB ligand, RANKL, in periodontal tissues during experimental movement of rat molars. *J Electron Microsc (Tokyo).* 2001;50:365–9.

43. Markiewicz MR, Margarone JE, III, Campbell JH, Aguirre A. Bisphosphonate-associated osteonecrosis of the jaws: a review of current knowledge. *J Am Dent Assoc.* 2005;136:1669–74.

44. Migliorati CA, Casiglia J, Epstein J, Jacobsen PL, Siegel MA, Woo SB. Managing the care of patients with bisphosphonate-associated osteonecrosis: an American Academy of Oral Medicine position paper. *J Am Dent Assoc.* 2005;136:1658–68.

CHAPTER SIX

ANALYSIS OF TISSUE NEOGENESIS IN GBR-TREATED EXTRACTION SOCKETS: CLINICAL, HISTOLOGICAL, AND MICRO-CT RESULTS

Neiva RF, Pagni G, Duarte F, Yi E, **Park CH**, Rayburn LA, Giannobile WV.

International Journal of Periodontics and Restorative Dentistry **2010** (in press)

6.1. ABSTRACT

AIMS: To perform a detailed evaluation of the healing of extraction sockets covered with a resorbable collagen membrane 12 weeks following exodontia, and to determine if this device has ossifying properties.

METHODS: Ten consecutive subjects in need of extraction of maxillary premolars were recruited. Each subject had a hopeless maxillary premolar extracted with minimal trauma. Sockets were then covered with a collagen barrier membrane alone. At 12 weeks, a re-entry surgery was performed, clinical measurements were repeated, and bone core biopsies were obtained prior to dental implant placement for histological and micro-CT analysis.

RESULTS: Study sites showed mean bone regeneration horizontally of 7.7 mm (B-L) and 4.6mm (M-D). Vertical bone repair showed a mean 10.9 mm of gain. Subtraction radiography showed a mean apical shift of the crestal bone at the center of the socket of 2.1mm (range: 0.7 - 4.3mm). Micro-CT and histology revealed formation of well-mineralized tissue at 12 weeks, with mean percentage of vital of bone of 45.87% + 12.35%. No signs of membrane ossification were observed.

CONCLUSION: A detailed analysis of tissue neogenesis in extraction sites protected by this barrier membrane has demonstrated that adequate bone formation for implant placement occurs as early as 12 weeks following exodontia, with minimal changes in alveolar ridge dimensions. No evidence of membrane ossification was observed.

6.2. INTRODUCTION

Tooth extraction leads to alveolar bone loss due to atrophy of the edentulous ridge [1,2]. Significant bone resorption occurs in the first 6 months following tooth extraction [3,4,5]. Reduction in alveolar ridge height and width may complicate or even prohibit optimal implant placement, and often compromises the esthetic and functional treatment outcome [6]. Alveolar ridge preservation has been evaluated in many studies [7-11]. A variety of bone grafting materials and barrier membranes have been studied for their ability to enhance bone formation in alveolar ridges [6,12], and to evaluate their bone healing and bone-forming capacity in extraction sockets [13,14]. However, these studies have only partially evaluated the events following tooth extraction. The aim of this study was to evaluate in detail bone tissue neogenesis that takes place following tooth extraction through clinical, histological, and microcomputed tomography (micro-CT) analyzes using a long-lasting collagen membraneα to protect the osseous defect from soft tissue invasion, maximizing the natural healing potential of the extraction socket. The secondary aim of this study is to further investigate the combination of histological, clinical and tomographic measures to model bone repair in vivo.

6.3. MATERIALS AND METHODS

The research protocol for this case-series clinical trial was approved by the University of Michigan committee governing the use of human subjects in clinical experimentation (IRB). This study was registered on the clinicaltrials.gov registry NCT00639860.

Inclusion & Exclusion Criteria - Ten consecutive subjects requiring extraction of maxillary premolars were selected from the patient pool of the Michigan Center of Oral Health Research (MCOHR), University of Michigan, School of Dentistry. Patient inclusion criteria for this study included: 1) systemically healthy subjects with 1 maxillary premolar tooth requiring extraction; 2) contained residual extraction sockets possess <80% bone loss in all dimensions (4-walled bony defects); 3) nonsmokers; 4) subjects willing and able to comply with all study-related procedures; and 5) subjects who read, understood, and were willing to sign an informed consent statement. Subjects with any of the following conditions were excluded from the study: 1) inadequate zone of keratinized gingiva or alveolar mucosa to obtain primary wound closure of the surgical site; 2) presence of acute infections at the time of tooth extraction; 3) clinically significant or unstable systemic diseases affecting bone or soft tissue growth; or other renal, hepatic, cardiac, endocrine, hematological, autoimmune or acute infectious diseases; 4) a history of head & neck radiation therapy; 5) subjects taking steroids, tetracycline or tetracycline analogues, bone therapeutic levels of fluorides, bisphosphonates, and other medications affecting bone turnover, or any investigational drug; 6) patients who were or become pregnant during the length of the study; 7) sites in

which one or both adjacent teeth were missing; 8) sites in which the buccal plate was missing or damaged during exodontia.

Preoperative Procedures - At the initial screening examination, a complete medical and dental history was obtained, and the goals of the study, potential risks and benefits were explained. Each subject received full-arch alginate impressions for fabrication of study models. Customized radiographic templates were created using the study models and stock radiograph positioning devices (XCP®, Rinn Corp., Elgin, IL) modified with a malleable acrylic (Triad®, Dentsply orp, York, PA) that was adapted to fit around an occlusal aluminum step wedge (Stanley M. Dunn, PhD, Neshanic Station, NJ). The study models were also used to fabricate occlusal templates to permit reproducible clinical measurements of the alveolar ridge dimensions.

Outcome Measures - The primary outcome variables evaluated included bone gain or loss in millimeters, radiographic bone changes, and percentage of new bone formation of the alveolar bone core biopsies. Bone topography was documented using UNC probes and occlusal templates. The following clinical measurements were made at baseline and re-entry: 1) distance from the occlusal template to the mesial, distal and mid crestal bone; and 2) socket depth (or template to crest distance at the 3-month re-entry surgery). Thickness of the buccal plate was measured 3 mm below the osseous crest at the center of the mesio-distal aspect of the socket using a boley-gauge caliper. All measurements were rounded to the nearest one-half millimeter.

Surgical Protocol & Treatment Assessment – A summary of study-related procedures is listed in Figure 6.1. To help minimize technical variances in the surgical treatment protocol, a single surgeon (RN) performed both baseline & 3-month re-entry surgeries. Under local anesthesia, full-thickness mucoperiosteal flaps were elevated; the selected tooth was extracted atraumatically15, followed by debridement of the sockets, and collection of all clinical measurements. Resorbable collagen barrier membranes (OSSIX^{TM} PLUS^{TM} is a trade mark of OraPharma, Inc. Warminster, PA USA) were used to cover the extraction sockets and flaps were advanced to achieve primary wound coverage. Flaps were secured with 4.0 and 5.0 polyglactin 910 sutures, utilizing an interrupted technique (Fig. 6.2). Postoperatively, a standardized periapical radiograph was taken of each surgical site utilizing a custom radiographic template and an aluminum step wedge (Stanley M. Dunn, PhD, Neshanic Station, NJ). All radiographs for each subject used the same digital x-ray unit, voltage & amperage (70 kV, 5 mA); and step wedge. The exposure time was recorded and the same settings were used again in subsequent radiographs. All subjects were prescribed ibuprofen (2.4 g/day), and either oral amoxicillin (1.5 g/day) or clindamycin (0.6 g/day) for 5 days. Subjects were instructed to change their diet to semi-liquid for 48 hours, followed by soft foods for the first 2 weeks. Subjects were also instructed to avoid toothbrushing close to the surgical site and to rinsetwice daily with a 0.12% chlorhexidine solution. At 1 and 2 weeks post-surgery, the extraction sites were inspected and gently cleaned with chlorhexidine-soaked gauze, health histories were reviewed, and photographs were taken. At 12 weeks, these procedures were repeated, and standardized periapical radiographs were taken. Soft tissue healing was assessed at 1, 2 and 12 weeks with a wound-healing index (WHI) according

to the following scheme: score "1" for uneventful wound healing with no gingival edema, erythema, suppuration, discomfort or membrane exposure; score "2" for uneventful wound healing with slight gingival edema, erythema, or discomfort, or membrane exposure and no suppuration; score "3" for poor wound healing with significant gingival edema, erythema, discomfort, loss of membrane or any suppuration. At 12 weeks, re-entry surgeries were performed and all clinical measurements were repeated. Bone core biopsies approximately 3 x 10 mm in size were harvested with a 3.7-mm (external diameter) trephine drill (Ace Surgical Supply Co., Inc., Brockton, MA) from the area corresponding to the center of the previous extraction socket. These biopsies were obtained through a flapless approach to include gingival tissues in the specimens (Fig. 6.2). The cores were immediately placed in bottles of 10% neutral buffered formalin (NBF) for fixation, and labeled for histological and micro-CT analysis. Following biopsy removal, flaps were elevated for additional clinical assessment and measurements and dental implants were placed in a single-stage approach.

Radiographic Image Analysis - Computer-assisted densitometric image analysis (CADIA) was used for evaluation of the radiographic bone density, utilizing a previously described technique.16 Radiographs obtained at baseline and 12 weeks were aligned using a real-time subtraction program17 and digitized in this spatial orientation. Images were then analyzed using CADIA (Fig. 6.3).

Micro-CT Analysis: Bone core specimens were scanned with 18x18x18um^3 voxel and 2x2 binning sizes. For beam filtration, 0.01 in. aluminum was used in front of the x-ray

source and polymethylmethacrylate (PMMA) bath-block was placed surrounding the sample in the PBS chamber, for prevention of beam hardening phenomena and equalization of the x-ray beam, respectively. The voltage and current were 80kV and 80uA. The region of interest (ROI) consisted of a 0.5mm thick and 6.0mm long hollow tube-shaped. ROI and original entire bone cores were analyzed volumetrically from apical to coronal sites. The assessment of 0.5mm thick outer layer samples was used to represent the osseous structure that surrounded the implants placed following bone core harvesting. The entire bone core measurements represent the mineralized tissue present in each biopsy (Fig. 6.4).

Histologic Processing and Analysis - Pictures were taken of each bone core biopsy prior to processing. The cores were demineralized in 10% formic acid to remove the calcium; dehydrated in a series of graded alcohols (Clear Rite, Richard Allen); and then embedded in glycol methacrylate (JB-4, PolySciences Inc.). Each core was cut into 5 μm sections, mounted on slides, and stained with Hematoxin & Eosin. The central most section of the bone cores was chosen for histomorphometric analysis. The sample was examined after its length was subdivided into 1.5mm long sections from the coronal to the apical portion of the core in a saggital orientation. The same sections were also divided longitudinally into 3 zones. Zones 1 and 2 represent the outer 0.5 mm layer, while zone 3 represents the innermost cylinder of bone. This histomorphometric approach was considered given that the most external layer, in relation to the inner core, more closely represents the bone quality of the bone in which the implant fixture will subsequently engage. The area of the analyzed section/layer was then divided by its total value in order to measure the bone

fraction area using image analysis (Image-Pro Plus). Total bone fraction areas for each sample and the mean SD of all samples is also included, as previously reported18. (Fig. 6.5)

Statistical Analysis - The data was analyzed on a per subject basis. Mean values of each parameter were calculated for each subject and each site at all time points and averaged within a subject and then across subjects.

6.4. RESULTS

Demographics – Mean age of research subjects was 47.7 y/o (range: 25-64 y/o). Six females and 4 males were included in this study.

Clinical Measurements – Table 1 shows pre- and post-treatment values of all clinical parameters.

Mean buccal plate thickness at baseline was 1.12mm (range: 0.5-2.0 mm). Study sites showed mean horizontal neogenesis of 7.7 mm (buccal to lingual) and 4.6 mm (mesial to distal). Vertical bone neogenesis measured 12 weeks following exodontia showed a mean value of 10.9 mm. Insignificant changes in ridge dimensions were observed at re-entry.

Subtraction Radiography – The position of the crestal bone at the center of the extraction socket appeared to be, on average, 2.1mm below its original position (range: 0.7 - 4.3mm). Subtracted images of the area of the extraction sockets revealed 13.5% of mean changes (STD: 0.27%) from baseline to 12 weeks, resulting in a mean value of 86.5% of radiographic bone fill.

Micro-CT – Statistically significant differences with the entire bone core measurements of bone volume fraction (BVF) and bone mineral density (BMD) were observed. However, in the outer layer measurement, there was no significant difference (Table 6.1). The statistical comparison between entire bone core measurements and outer layer measurements demonstrated that even though the inner zone (1.7 mm inner-diameter) of the bone core still had relatively different mineralization, the outer zone already had well-

mineralized tissue formations on the most coronal 6.0 mm. Therefore, based on micro-CT analysis it is clear that the collagen membrane used in this study successfully prevented epithelial down growth into the extraction socket, maximizing bone formation (Fig. 6.6).

Histomorphometry – Mean vital bone values for each section were the following: S1 = 46.34%. (+13.08%), S2 = 46.11% (+13.79%), S3 = 49.22% (+14.67%), and S4 = 50.47% (+10.89%). When these values were combined and divided by the number of section, the total mean percentage of vital bone was 45.87% (+12.35%). Mean vital bone values for the external and internal layers of the cores were 47.96% (+15.42%) and 44.24% (+10.46%), respectively. When these values were combined and divided by the number of layers, the total mean percentage of vital bone was 46.09% + 12.47%. These values are schematically represented. It is not clear from the statistical analysis used whether the bone quality was superior in the apical or in the coronal portion of the regenerated bone. However, it is evident that a higher bone fraction area was encountered in the external layer when compared to the inner core, suggesting the possibility that the overall bone fraction area of the whole sample might indeed be lower that that of the bone surrounding a dental implant (Fig. 6.6).

4-A.5. DISCUSSION

Tooth extraction results in alveolar bone loss due to resorption of the edentulous ridge [19-22]. An average of 40-60% of original height and width is expected to be lost after tooth extraction, with the greatest loss occurring during the first 2 years [23-27]. This can negatively influence bone volume that is needed for future dental implant placement. Research has demonstrated that the alveolar ridge in the maxillary anterior area can be reduced by 23% in the first 6 months after exodontia, and an additional 11% in the following 5 years [8]. In the posterior mandible, resorption happens primarily in the buccal/labial direction, resulting in a lingual displacement of the alveolar crest8. The rate of reduction of residual alveolar ridges has shown to be greater in mandibular (0.4 mm/year) than in maxillary arches (0.1 mm/year) [28]. As a consequence, alveolar ridge atrophy may prohibit optimal implant placement, compromising the final esthetic and functional outcomes [29].

Alveolar ridge preservation (a.k.a., socket preservation; socket augmentation) has been evaluated in many studies [9-11]. Multiple bone grafting regimens and techniques have been suggested to limit alveolar ridge atrophy, and to evaluate the osteogenic capacity of extraction sockets [30-32]. Generally, these procedures are primarily aimed at maintaining current bone level and secondarily, regenerating new bone [15]. Studies have also shown negative results when alveolar ridge preservation was attempted, possibly due to utilization of inadequate techniques and/or materials [33-36]. For example, Zubillaga et al. (2003) evaluated a combination of demineralized freeze-dried bone allograft and a bioresorbable membrane for socket augmentation. The negative results observed were

attributed to the slow resorption of the gelatin carrier of the graft material and possible inhibition of new bone formation [36]. Hence, utilization of certain materials may in fact inhibit tissue neogenesis. Other forms of bone grafting materials have also been suggested for this purpose. However, the need to fill an extraction socket following exodontia is controversial. This study intended to better understand the healing of extraction sockets without grafting materials by maximizing the healing potential that these defects have. Research has demonstrated the utility of resorbable and non-resorbable barrier membranes in preserving alveolar ridges following tooth extraction [37-43]. When combined with barrier membranes, bone graft materials have also shown to prevent collapse of the barrier membrane [43-49]. This study failed to support this hypothesis since it demonstrated that the clot that is formed following tooth extraction appears to prevent membrane collapse in this type of osseous defect.

This study aimed to describe tissue neogenesis following exodontia, when the extraction site was protected from epithelial down growth using a collagen membrane, following a controlled and detailed analysis. Collagen membranes are preferable due to their resorbable property that eliminates membrane retrieval procedures and are highly biocompatible with the surrounding oral tissues [50, 51]. The device evaluated in this study is a resorbable porcine-derived collagen membrane, which is manufactured using a special cross-linking technology that utilizes a sugar-based agent, as opposed to chemicals (glutaraldehyde) or physical techniques (UV or gamma irradiation). The nonenzymatic glycation process provides ability to control biodurability of the barrier membrane for 4-6 months, allowing sufficient time for osseous defects to achieve optimal

bone regeneration. Evidence of this capacity was noted since all sites showed some remnants of this barrier at re-entry. No adverse events (i.e. membrane exposure, infection) following GBR therapy were noted throughout the study and the device used appeared to be well tolerated clinically and histologically during the healing process of all subjects. It has been suggested in the literature that the device used in this study possesses ossifying properties [52, 53]. Despite the excellent handling and barrier properties demonstrated in this study, no signs of membrane ossification were identified. In order to evaluate tissue neogenesis in extraction sites in a controlled manner, it is important to attempt to standardize the size of the osseous defects and the location of these defects in the dental arches. The maxillary premolar region was selected for its consistent root length, common need for tooth replacement, and anatomical features that would allow reproducibility of study-related procedures. Table 4-A.1 demonstrates that a short range of defect sizes was observed. It is unclear if significant differences in terms of tissue neogenesis exist when maxillary and mandibular sites arecompared, but it can be hypothesized that differences may exist due to morphometric characteristics of mandibular and maxillary alveolar bone. Hence, in order to exclude a possible variable, only maxillary sites were included.

Given the importance of landmarks for clinical measures, occlusal guides were utilized, using a supposedly fixed reference point (occlusal surface of adjacent teeth). This device allows the examiner to simply slide the probe through groves, allowing measurement to be recorded from the exact same location and angulations. Clinical measurement revealed insignificant morphologic changes from baseline to re-entry procedures. It is important to

emphasize that all sites presented with intact socket walls following exodontia. A common factor known to limit the healing potential of extraction sockets and to indicate the use of bone grafting materials for ridge preservation, is the absence or the thickness of the buccal plate of the socket [54-56]. Despite the reduced mean thickness of the buccal plates (1.12 mm) evaluated, ridge dimensions were preserved and new bone formation occurred. It can be hypothesized however, that less favorable results should be expected when only a barrier membrane is used and one or more socket walls are missing.

Radiographic analysis of bone formation is limited by the two-dimensional nature of radiographs. When a series of radiographs is compared, it becomes difficult to determine if changes have occurred, mainly due to differences in film positioning and angulations. To compensate for these limitations, standardized radiographs were used in this study. A radiographic film holder was created for each subject, and the same device was used for additional radiographs. Subtraction radiography revealed that this method of radiographic standardization is valid, since comparable images were obtained. When images were compared, the follow-up position of the crestal bone at the center of the defect appeared to be in average, 2.1mm below its original position. Previous studies have reported similar findings [57-59]. What is important to note is that the mean degree ofradiopacity within the socket at 12 weeks compared to the radiopacity of the surrounding alveolar bone showed 86.5% percentage of bone fill. This is a significant finding since no bone substitutes were used in this study, although for ethical reasons only contained lesions were selected for treatment.

Histomorphometric analysis of bone cores has been used to evaluate bone quality, and particularly the percentage of vital bone, when bone substitutes were used [59]. In this study, a more detailed evaluation was performed. Bone cores were harvested using a flapless approach to obtain a detailed observation of the bone/soft tissue interface and to detect changes in bone quality along an apical-coronal axis. Hence, slides were divided in 1.5mm sections, with each section being analyzed independently. Surprisingly, no significant differences were observed, meaning that a very homogenous pattern of neogenesis was observed within the entire bone core. An additional evaluation was performed, by stratifying the bone cores in outer and inner layers. A significant difference was observed, which supports the knowledge that tissue neogenesis in an extraction site is mostly originated from the socket walls rather than the apical region. Based on the nature of tissue neogenesis following exodontia, analysis of the entire core may underestimate the quality and the composition of the newly formed tissue. Hence, a more detailed evaluation of these bone cores was performed using micro-CT images. This technology enables a three-dimensional evaluation of the entire core, instead of only a slide. Micro-CT confirmed the finding of histomorphometry, with more mineralization present on the outer layers of the core. This is a significant finding since it may better represent the area of interest, i.e., the alveolar bone immediately adjacent to the location of the biopsy harvest (zone adjacent to implant-anchoring osseous support). It is important to emphasize that these biopsies were composed of newly formed bone from a protected blood clot, and not from graft particles that became incorporated into newly developed mineralized tissue. Graft particles undergo a slow process of resorption, which may or may not be followed by new bone formation.

6.6. CONCLUSIONS

Based on these results it can be concluded that a detailed analysis of tissue neogenesis in extraction sites protected by a barrier membrane has demonstrated that adequate bone tissue formation for implant placement occurs as early as 12 weeks following exodontia, with minimal changes in alveolar ridge dimensions. No signs of membrane ossification were observed.

6.7. FIGURES

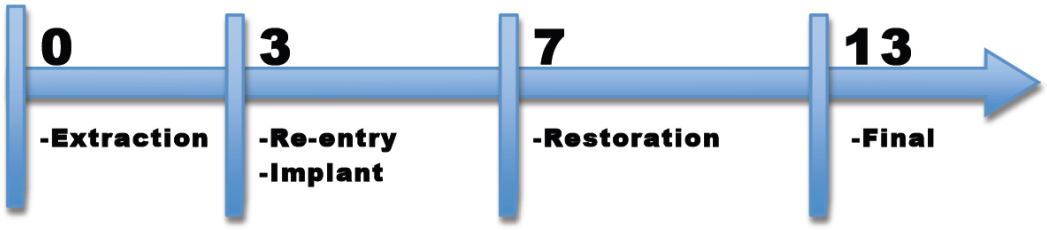

Figure 6.1. Timeline of study procedures in months. (0) Tooth extraction, alveolar ridge preservation and initial measurements; (3) Re-entry procedures including core biopsy and implant placement; (7) Implant restoration; (13) Final follow-up appointment.

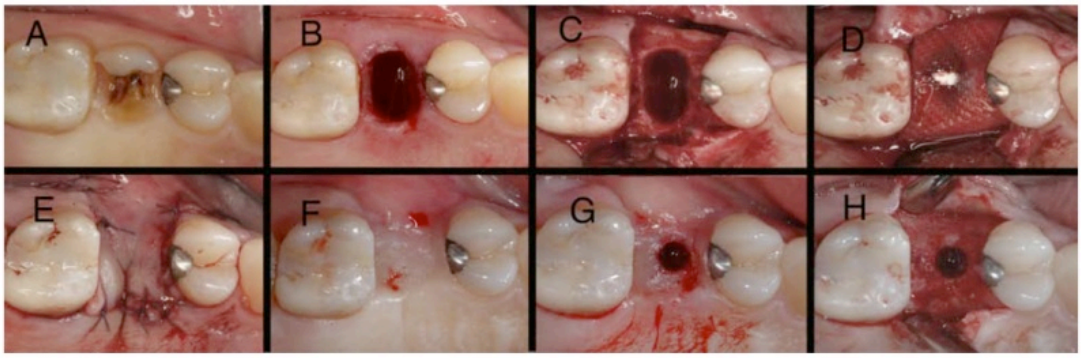

Figure 6.2. Steps of clinical assessment of GBR therapy for extraction sockets. (A) Baseline; (B) Atraumatic exodontias; (C) Flap elevated for clinical measurements; (D) Barrier membrane placed over the socket; (E) Flap advancement for primary wound coverage; (F) 12-week follow-up; (G) Flapless core biopsy; (H) Re-entry for second clinical measurements.

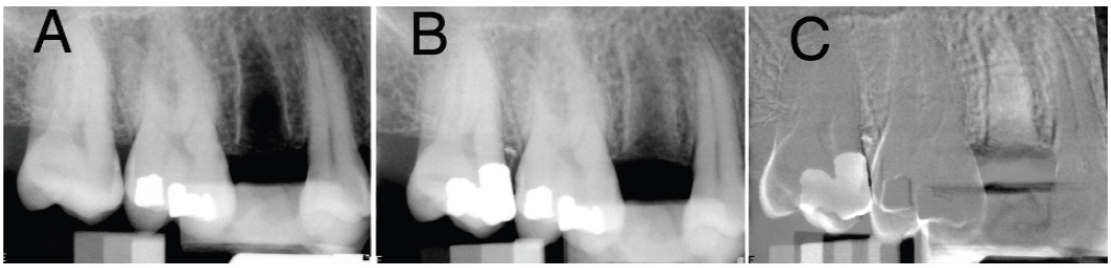

Figure 6.3. Subtraction radiography. (A) Standardized digital radiograph immediately following tooth extraction; (B) 12-week follow-up radiograph; (C) Subtracted image.

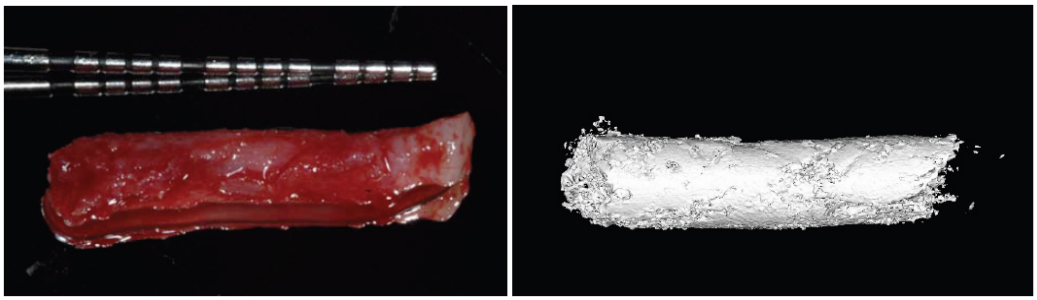

Figure 6.4. Micro-CT analysis. (A) Bone core biopsy harvested with a flapless approach; (B) corresponding micro-CT image.

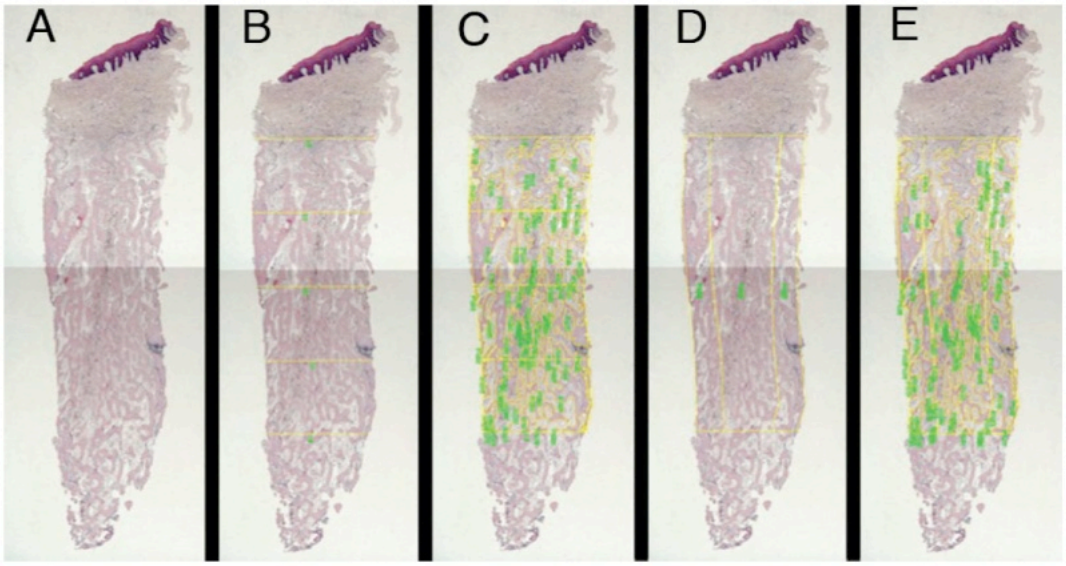

Figure 6.5. Histomorphometry. (A) Original image; (B) 1.5mm sections; (C) sectional histomorphometry; (D) outer and inner layers; (E) longitudinal histomorphometry.

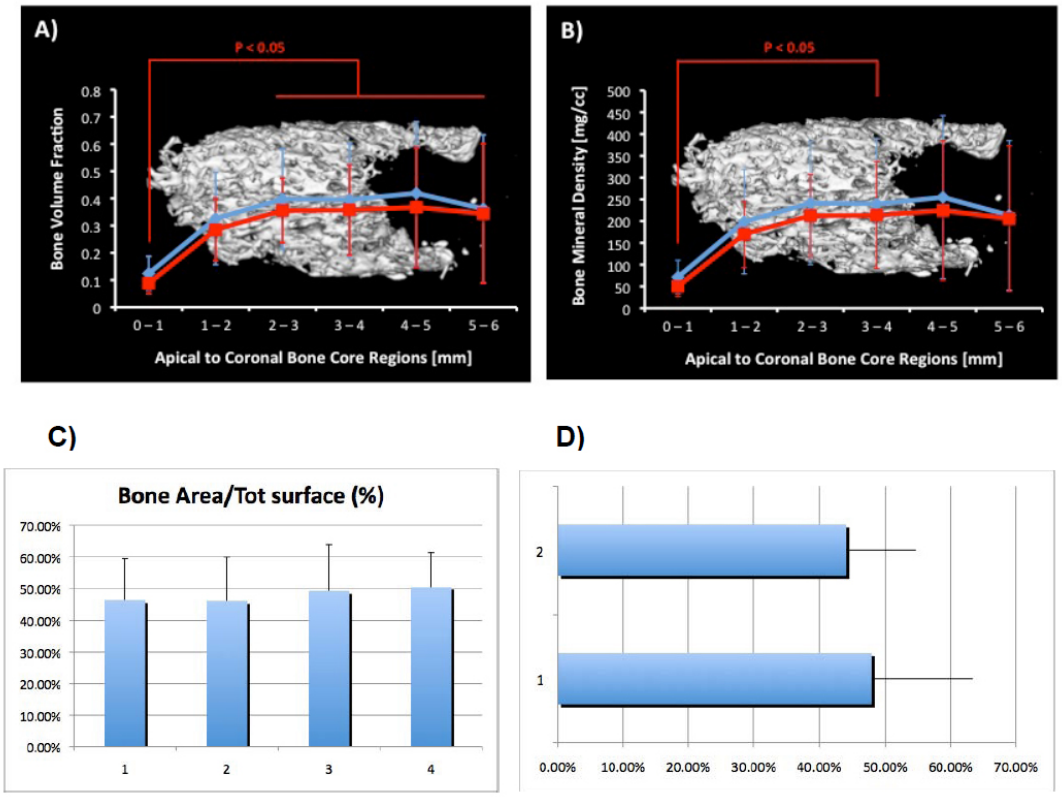

Figure 6.6. GBR promotes bone repair as measured histomorphometrically. (A) Bone volume fraction for the entire bone core (red) and the outer 0.5mm (blue); (B) bone mineral density for the entire bone core (red) and the outer 0.5mm (blue); (C() percentage of vital bone on each 1.5mm section (1=most coronal, 4=most apical); (D) mean values for outer (1) and inner (2) layers.

6.8. TABLE

	Day 0	12-wks	Changes
Socket Width (B/L)	8.3 mm (7-10 mm)	0.6 mm (0-3 mm)	- 7.7 mm*
Socket Width (M/D)	5.1 mm (4-8 mm)	0.5 mm (0-3 mm)	- 4.6 mm*
Stent-to-Buccal Plate	5.6 mm (4-8 mm)	5.5 mm (4-8 mm)	- 0.1 mm
Stent-to-Mesial Osseous Crest	4.0 mm (2-6 mm)	4.1 mm (3-5 mm)	+ 0.1 mm
Stent-to-Distal Osseous Crest	4.1 mm (2-6 mm)	4.2 mm (3-5 mm)	+0.1 mm
Stent-to-Mid Osseous Crest	4.7 mm (3-7 mm)	4.9 mm (3-8 mm)	+0.2 mm
Stent-to-Apex of Socket	16.5 mm (11-20 mm)	5.6 mm (3-8 mm)	- 10.9 mm*

Table 6.1. Clinical open bone measurements following GBR of contained extraction sockets.

6.9. REFERENCES

1. Bays RA. The pathophysiology and anatomy of edentulous bone loss. In: Fonseca RJ, Davis WH, editors. Reconstructive Preprosthetic Oral and Maxillofacial Surgery. 1st ed. Philadelphia: W B Saunders; 1986. p. 1-17.

2. Mecall RA, Rosenfeld AL. The influence of residual ridge resorption patterns on implant fixture placement and tooth position. Part I. Int J Periodont Rest Dent 1991;11:9-23.

3. Sevor JJ, Meffert R. Placement of implants into fresh extraction sites using a resorbable collagen membrane: Case Reports. Pract Periodont Aesth Dent 1992;4:35-41.

4. Werbitt MJ, Goldberg TV. The immediate implant: Bone preservation and bone regeneration. Int J Periodont Rest Dent 1992;12:207-17.

5. Bragger U, Hammerle CHF, Lang NP. Immediate transmucosal implants using the principle of guided tissue regeneration (II). A cross-sectional study comparing the clinical outcome 1 year after immediate to standard implant placement. Clin Oral Implants Res 1996;7:268-76.

6. Howell TH, Fiorellini J, Jones A, Alder M, Nummikoski P, Lazaro M, et al. A feasibility study evaluating rhBMP-2/absorbable collagen sponge device for local alveolar ridge preservation or augmentation. Int J Periodont Rest Dent 1997;17:125-39.

7. Artzi Z, Nemcovsky CE. The application of deproteinized bovine bone mineral for ridge preservation prior to implantation. Clinical and histological observations in a case report. J Periodontol 1998;69(9):1062-7.

8. Artzi Z, Tal H, Dayan D. Porous bovine bone mineral in healing of human extraction sockets. Part 1: histomorphometric evaluations at 9 months. J Periodontol 2000;71(6):1015-23.

9. Ashman A, Lopinto J. Placement of implants into ridges grafted with bioplant HTR synthetic bone: histological long-term case history reports. J Oral Implantol 2000;26(4):276-90.

10. Froum S, Orlowski W. Ridge preservation utilizing an alloplast prior to implant placement-- clinical and histological case reports. Pract Periodontics Aesthet Dent 2000;12(4):393-402; quiz 04.

11. Froum S, Cho SC, Rosenberg E, Rohrer M, Tarnow D. Histological comparison of healing extraction sockets implanted with bioactive glass or demineralized freeze-dried bone allograft: a pilot study. J Periodontol 2002;73(1):94-102.

12. Nevins M, Mellonig JT. Enhancement of the damaged edentulous ridge to receive dental implants: A combination of allograft and the Gore-Tex membrane. Int J Periodont Rest Dent 1992;12:97-111.

13. Becker W, Becker BE, Caffesse R. A comparison of demineralized freeze-dried bone and autologous bone to induce bone formation in human extraction sockets. J Periodontol 1994;65(12):1128-33.

14. Becker W, Urist M, Becker BE, Jackson W, Parry DA, Bartold M, et al. Clinical and histologic observations of sites implanted with intraoral autologous bone grafts or allografts. 15 human case reports. J Periodontol 1996;67(10):1025-33.

15. Wang H, Kiyonobu K, Neiva R. Socket Augmentation: Rationale & Technique. Int J Periodontics Restorative Dent 2004(August):00-00.

16. Bragger U, Pasquali L, Kornman KS. Remodelling of interdental alveolar bone after periodontal flap procedures assessed by means of computer-assisted densitometric image analysis (CADIA). J Clin Periodontol 1988;15(9):558-64.

17. Dove SB, McDavid WD, Wilcox D. C. A. R. E. TM (Computer Assisted Radiographic Evaluation). A computer program for longitudinal radiographic assessment with subtraction radiography and quantitative radiography. San Antonio: University of Texas Health Science Center at San Antonio; 1991.

18. Park CH, Abramson ZR, Taba M, Jr., Jin Q, Chang J, Kreider JM, et al. Three-dimensional micro-computed tomographic imaging of alveolar bone in experimental bone loss or repair. J Periodontol 2007;78(2):273-81.

19. Bays R. The pathophysiology and anatomy of edentulous bone loss. Reconstructive Preprosthetic Oral and Maxillofacial Surgery 1986;1st ed:1-17.

20. Mecall RA, Rosenfeld AL. Influence of residual ridge resorption patterns on fixture placement and tooth position, Part III: Presurgical assessment of ridge augmentation requirements. Int J Periodontics Restorative Dent 1996;16(4):322-37.

21. Mecall RA, Rosenfeld AL. The influence of residual ridge resorption patterns on implant fixture placement and tooth position. 2. Presurgical determination of prosthesis type and design. Int J Periodontics Restorative Dent 1992;12(1):32-51.

22. Mecall RA, Rosenfeld AL. Influence of residual ridge resorption patterns on implant fixture placement and tooth position. 1. Int J Periodontics Restorative Dent 1991;11(1):8-23.

23. Sevor JJ, Meffert R. Placement of implants into fresh extraction sites using a resorbable collagen membrane: case reports. Pract Periodontics Aesthet Dent 1992;4(3):35-41.

24. Polizzi G, Grunder U, Goene R, Hatano N, Henry P, Jackson WJ, et al. Immediate and delayed implant placement into extraction sockets: a 5-year report. Clin Implant Dent Relat Res 2000;2(2):93-9.

25. Grunder U, Polizzi G, Goene R, Hatano N, Henry P, Jackson WJ, et al. A 3-year prospective multicenter follow-up report on the immediate and delayed-immediate placement of implants. Int J Oral Maxillofac Implants 1999;14(2):210-6.

26. Werbitt MJ, Goldberg PV. The immediate implant: bone preservation and bone regeneration. Int J Periodontics Restorative Dent 1992;12(3):206-17.

27. Werbitt MJ, Goldberg PV. [Immediate implantation. Preservation of bone volume and osseous regeneration]. J Parodontol 1991;10(2):157-66.

28. Nemcovsky CE, Serfaty V. Alveolar ridge preservation following extraction of maxillary anterior teeth. Report on 23 consecutive cases. J Periodontol 1996;67(4):390-5.

29. Howell TH, Fiorellini J, Jones A, Alder M, Nummikoski P, Lazaro M, et al. A feasibility study evaluating rhBMP-2/absorbable collagen sponge device for local alveolar ridge preservation or augmentation. Int J Periodontics Restorative Dent 1997;17(2):124-39.

30. Bartee BK. Extraction site reconstruction for alveolar ridge preservation. Part 1: rationale and materials selection. J Oral Implantol 2001;27(4):187-93.

31. Becker W, Hujoel P, Becker BE. Effect of barrier membranes and autologous bone grafts on ridge width preservation around implants. Clin Implant Dent Relat Res 2002;4(3):143-9.

32. Fowler EB, Breault LG, Rebitski G. Ridge preservation utilizing an acellular dermal allograft and demineralized freeze-dried bone allograft: Part I. A report of 2 cases. J Periodontol 2000;71(8):1353-9.

33. Cohen ES. Ridge enhancement and socket preservation utilizing the subepithelial connective tissue graft: a case report. Pract Periodontics Aesthet Dent 1995;7(2):53-8; quiz 60.

34. Tal H. Autogenous masticatory mucosal grafts in extraction socket seal procedures: a comparison between sockets grafted with demineralized freeze-dried bone and deproteinized bovine bone mineral. Clin Oral Implants Res 1999;10(4):289-96.

35. Zitzmann NU, Scharer P, Marinello CP. Factors influencing the success of GBR. Smoking, timing of implant placement, implant location, bone quality and provisional restoration. J Clin Periodontol 1999;26(10):673-82.

36. Zubillaga G, Von Hagen S, Simon BI, Deasy MJ. Changes in alveolar bone height and width following post-extraction ridge augmentation using a fixed bioabsorbable membrane and demineralized freeze-dried bone osteoinductive graft. J Periodontol 2003;74(7):965-75.

37. Lekovic V, Camargo PM, Klokkevold PR, Weinlaender M, Kenney EB, Dimitrijevic B, et al. Preservation of alveolar bone in extraction sockets using bioabsorbable membranes. J Periodontol 1998;69(9):1044-9.

38. Wang HL, Kimble K, Eber R. Use of bone grafts for the enhancement of a GTR-based root coverage procedure: a pilot case study. Int J Periodontics Restorative Dent 2002;22(2):119- 27.

39. Wang HL, Bunyaratavej P, Labadie M, Shyr Y, MacNeil RL. Comparison of 2 clinical techniques for treatment of gingival recession. J Periodontol 2001;72(10):1301-11.

40. Wang HL, Carroll MJ. Guided bone regeneration using bone grafts and collagen membranes. Quintessence Int 2001;32(7):504-15.

41. Bartee BK. Extraction site reconstruction for alveolar ridge preservation. Part 2: membraneassisted surgical technique. J Oral Implantol 2001;27(4):194-7.

42. Yang J, Lee HM, Vernino A. Ridge preservation of dentition with severe periodontitis. Compend Contin Educ Dent 2000;21(7):579-83; quiz 84.

43. Ashman A. Postextraction ridge preservation using a synthetic alloplast. Implant Dent 2000;9(2):168-76.

44. Nevins M, Mellonig JT. Enhancement of the damaged edentulous ridge to receive dental implants: a combination of allograft and the GORE-TEX membrane. Int J Periodontics Restorative Dent 1992;12(2):96-111.

45. Nevins M, Mellonig JT. The advantages of localized ridge augmentation prior to implant placement: a staged event. Int J Periodontics Restorative Dent 1994;14(2):96-111.

46. Mellonig JT, Nevins M. Guided bone regeneration of bone defects associated with implants: an evidence-based outcome assessment. Int J Periodontics Restorative Dent 1995;15(2):168- 85.

47. Mellonig JT, Nevins M, Sanchez R. Evaluation of a bioabsorbable physical barrier for guided bone regeneration. Part I. Material alone. Int J Periodontics Restorative Dent 1998;18(2):139-49.

48. Oikarinen KS, Sandor GK, Kainulainen VT, Salonen-Kemppi M. Augmentation of the narrow traumatized anterior alveolar ridge to facilitate dental implant placement. Dent Traumatol 2003;19(1):19-29.

49. Wiesen M, Kitzis R. Preservation of the alveolar ridge at implant sites. Periodontal Clin Investig 1998;20(2):17-20.

50. Sableman E. Biology, Biotechnology, and Biocompatibility of Collagen. Biocompatibility of Tissue Analogs. CRC Press 1985;First edition(Boca Raton, FL):27.

51. Postlethwaite AE, Seyer JM, Kang AH. Chemotactic attraction of human fibroblasts to type I, II, and III collagens and collagen-derived peptides. Proc Natl Acad Sci U S A 1978;75(2):871-5.

52. Zubery Y, Nir E, Goldlust A. Ossification of a collagen membrane cross-linked by sugar: a human case series. J Periodontol 2008;79(6):1101-7.

53. Zubery Y, Goldlust A, Alves A, Nir E. Ossification of a novel cross-linked porcine collagen barrier in guided bone regeneration in dogs. J Periodontol 2007;78(1):112-21.

54. Kerr EN, Mealey BL, Noujeim ME, Lasho DJ, Nummikoski PV, Mellonig JT. The effect of ultrasound on bone dimensional changes following extraction: a pilot study. J Periodontol 2008;79(2):283-90.

55. Vance GS, Greenwell H, Miller RL, Hill M, Johnston H, Scheetz JP. Comparison of an allograft in an experimental putty carrier and a bovine-derived xenograft used in ridge preservation: a clinical and histologic study in humans. Int J Oral Maxillofac Implants 2004;19(4):491-7.

56. Luczyszyn SM, Papalexiou V, Novaes AB, Jr., Grisi MF, Souza SL, Taba M, Jr. Acellular dermal matrix and hydroxyapatite in prevention of ridge deformities after tooth extraction. Implant Dent 2005;14(2):176-84.

57. Fickl S, Zuhr O, Wachtel H, Stappert CF, Stein JM, Hurzeler MB. Dimensional changes of the alveolar ridge contour after different socket preservation techniques. J Clin Periodontol 2008;35(10):906-13.

58. Rothamel D, Schwarz F, Herten M, Engelhardt E, Donath K, Kuehn P, et al. Dimensional ridge alterations following socket preservation using a nanocrystalline hydroxyapatite paste: a histomorphometrical study in dogs. Int J Oral Maxillofac Surg 2008;37(8):741-7.

59. Neiva RF, Tsao YP, Eber R, Shotwell J, Billy E, Wang HL. Effects of a putty-form hydroxyapatite matrix combined with the synthetic cell-binding peptide P-15 on alveolar ridge preservation. J Periodontol 2008;79(2):291-9.

CHAPTER SEVEN

ANGIOGENIC AND OSTEOGENIC POTENTIAL OF BONE REPAIR CELLS FOR CRANIOFACIAL REGENERATION

Kaigler D, Pagni G, **Park CH**, Tarle S, Bartel R, Giannobile WV.

Tissue Engineering Part A. **(Epub ahead of print, July 10th 2010)**

7.1. ABSTRACT

There has been increased interest in the therapeutic potential of bone marrow derived cells for tissue engineering applications. Bone repair cells (BRCs) represent a unique cell population generated via an ex vivo, closed-system, automated cell expansion process, to drive the propagation of highly osteogenic and angiogenic cells for bone engineering applications. The aims of this study were (1) to evaluate the in vitro osteogenic and angiogenic potential of BRCs, and (2) to evaluate the bone and vascular regenerative potential of BRCs in a craniofacial clinical application. BRCs were produced from bone marrow aspirates and their phenotypes and multipotent potential characterized. Flow cytometry demonstrated that BRCs were enriched for mesenchymal and vascular phenotypes. Alkaline phosphatase and von Kossa staining were performed to assess osteogenic differentiation, and reverse transcriptase-polymerase chain reaction was used

to determine the expression levels of bone specific factors. Angiogenic differentiation was determined through in vitro formation of tube-like structures and fluorescent labeling of endothelial cells. Finally, 6 weeks after BRC transplantation into a human jawbone defect, a biopsy of the regenerated site revealed highly vascularized, mineralized bone tissue formation. Taken together, these data provide evidence for the multilineage and clinical potential of BRCs for craniofacial regeneration.

7.2. INTRODUCTION

The demand for tissue replacements has led to the emergence and significant expansion of the field of tissue engineering [1]. Craniofacial regenerative medicine applications have demonstrated significant impacts for oral soft and hard tissue repair [2, 3]. In preclinical model systems, multipotent cells derived from bone marrow have become a popular source of cells for regenerating bone, ligament, tendon, and cartilage [4-8]. More recently, autologous grafts utilizing various formulations of bone marrow or bone-marrow-derived cells have been investigated in clinical studies for skeletal bone repair [9, 10] and craniofacial regeneration [11-14]. Although there has been modest success achieved in these approaches, major limitations still include crude isolation techniques and poorly defined cell preparations appropriate for grafting, inability to produce sufficient cell numbers for transplantation without multiple passages in traditional open tissue culture systems, and a lack of identification of an ideal cell type or cell population for transplantation. Despite the specific limitations of currently defined cell isolation and preparation protocols, an overarching challenge common to all cell and tissue transplantation strategies is the inability to produce a supportive vasculature for graft incorporation and cell survival.

It has been well-established that key to the development of bone tissue is not only the formation of bone but also the coordinated development of a supportive blood supply [15]. Thus, when employing cell transplantation strategies, not only does the osteoprogenitor cell type need to be considered, but formation of a functional vasculature to support cell viability and maturation of the tissue warrants serious consideration as

well. As a result, some strategies used to engineer and regenerate bone tissue employ cotransplantation of osteoprogenitor cells with either hematopoietic or endothelial cells to help establish a supportive blood supply to the transplanted cells [16- 19]. Although these approaches all hold great promise, it would be more desirable to transplant a cell population that contains cells capable of establishing both a blood supply and regenerating bone.

An automated cell-manufacturing process has been developed that utilizes a single-pass perfusion (SPP) process; this enables a clinical-scale expansion of autologous, primary, human bone repair cells (BRCs) derived from bone marrow. In SPP, the culture medium is continuously replaced with a fresh medium at a slow, controlled rate without the disturbance, removal, or passaging of cells. This technology results in significant expansion of primary human cells [20, 21] and has previously demonstrated clinical success in the expansion of bone marrow and blood cells for replenishment of hematopoietic cells after treatment of various blood dyscrasias [22-25]. Additionally, results of recent *in vitro* and *in vivo* studies have generated interest in using this process to produce cells for bone tissue regeneration [26].

The hypothesis underlying the current study is that BRCs have osteogenic and angiogenic potential that could manifest in their ability to regenerate bone and vascular tissue in a clinical craniofacial application. To address this hypothesis, we aimed to first examine the multipotency of BRCs *in vitro*, with particular emphasis on elucidation of their angiogenic and osteogenic capacities. Second, we sought to determine if BRCs could

form bone and accelerate osteogenesis clinically when implanted within an osseous defect in the jaw.

7.3. MATERIALS AND METHODS

4-B.3.1. Bone marrow harvest and BRC production

The production of BRCs has been previously described [26]. Briefly, after U.S. Food and Drug Administration (FDA) and University of Michigan Institutional Review Board approval, 10 healthy subjects giving informed consent underwent a bone marrow aspiration of the posterior ilium under conscious sedation and local anesthetic. Of these 10 subjects, where indicated, subsets of them (marrow) were used for phenotypic characterization of cells. Collected marrow was transferred to a sterile blood bag and bone marrow mononuclear cells (BMMNCs) were purified by Ficoll density gradient centrifugation. BMMNCs were then inoculated into a bioreactor, which is a proprietary computer-controlled, automated cell-processing unit, the Aastrom Replicell® System (Aastrom Biosciences). The Cell Cassette within this system provides a functionally closed, sterile environment in which cell production occurs. The fluid pathway in the Cell Cassette includes the cell growth chamber, a medium supply container, a mechanism for medium delivery, a waste medium collection container, and a container for the collection of harvested cells. All components are interconnected with sterile barrier elements throughout to protect the culture from contamination during use. The culture medium consists of Iscove's modified Dulbecco's medium, 10% fetal bovine serum, 10% horse serum, and 5 μM hydrocortisone. This system incorporates SPP in which a fresh medium flows slowly over cells without retention of waste metabolites or differentiating cytokines [20]. In-process safety test (absence of bacterial and fungal contaminants and endotoxins) was conducted on an sampled effluent medium at 48 h before harvest. After cultivation for 12 days at 37°C and 5% CO_2, the BRC product was harvested by trypsinization, washed in a physiologic buffer, and collected into a sterile bag and resuspended in Isolyte

and 0.5% human serum albumin, where it was stored until the time of transplantation Fig. 4-B.1). Sterility, endotoxin, and mycoplasma testing were all conducted on the BRCs.

The Replicell System is an automated one-cycle system that requires the input to be derived from fresh bone marrow aspirates; as a result, once BRCs are removed from the system, it is not possible to regrow or resume culture of cells within this same system. Thus, further culture of BRCs for *in vitro* assays required conventional tissue culturing techniques in both experimental and control conditions. Excess BRC product not utilized for transplantation was cultured in a medium consistent with culture of bone-marrow-derived stem cells [27], consisting of minimum essential alpha medium (αMEM) (Gibco–Invitrogen #12571) with 15% fetal bovine serum (Gibco-Invitrogen-16000), 100 μM ascorbic acid 2 phosphate (Sigma A-8960), and 5 μg/mL Gentamicin (Invitrogen #15750060), and grown in a 37°C humidified tissue culture incubator under 5% CO_2. This medium was used for control conditions (without incorporation of differentiation/inductive factors) in the *in vitro* assays and it should also be noted that this open culture system and media used were distinctly different from those used to produce the BRC product. Cell culture media were changed every 2 or 3 days. Cells were grown in T-150 flasks to ~80% confluence, followed by cell washing with phosphate-buffered saline (PBS) and trypsinization before being split into 12-well plates or 60 mm tissue culture dishes for differentiation assays.

7.3.2. Flow cytometry

Phenotypic comparison of cell surface marker expression was made between the starting BMMNCs and the final BRC product from a subset of four subjects who had marrow

harvested for generation of BRCs. Flow cytometry was performed on the same day of isolation of the BMMNCs and immediately after production of BRCs (i.e., neither BMMNCs nor BRCs were cultured, as described in the Cell Culture section, before performance of the flow cytometry). BMMNCs or BRCs were washed and resuspended in 1× Dulbecco's PBS (Gibco) containing 1% bovine serum albumin. Samples were F_c receptor blocked with normal mouse IgG for approximately 10 min. Tubes containing 0.5 $\times 10^6$ cells in approximately 0.1 mL were then stained at 2°C–8°C with phycoerythrin (PE) or PE cyanin 5-conjugated anti-CD90 (Thy1) antibodies, PE-conjugated anti-CD11b, anti-Gly-A, anti-CD34, anti-AC133, anti-CD19, anti-vascular endothelial growth factor (VEGF)R1, anti-Tie2, anti-CD145, fluourescein isothyocyanate-conjugated anti-CD66b, anti-CD14, anti-CD45, anti-CD3, anti-CD144 antibodies, and PE cyanin 5-conjugated anti-CXCR4 (CD184) (Beckman Coulter). After 15 min, cells were washed and resuspended in 0.5 mL PBS/bovine serum albumin for analysis on the Epics XL-MCL (Beckman Coulter) or FC500 flow cytometer.

7.3.3. In vitro multilineage differentiation

Multipotency of BRC cultures was determined by *in vitro* differentiation assays of osteogenesis, chondrogenesis, and adipogenesis. BRCs were plated at a density of 30,000 cells per well in 12-well plates. At >90% confluency, cells were induced, according to previously described protocols [28], with osteogenic (BRC medium including 5 mM β-glycerol phosphate, 100 nM dexamethasone, and 50 μM ascorbic acid 2-phosphate), chondrogenic (BRC medium including 50 μM ascorbic acid 2-phosphate, 100 nM dexamethasone, 5 μg/mL human insulin, 1 ng/mL transforming growth factor-β, 400 μM

proline, and 1× Nonessential amino acids), or adipogenic (BRC medium including 0.5 mM isobutylmethylxanthine, 1 μM dexamethasone, 10 μg/mL human insulin, and 200 μM indomethacin) medium. BRCs were grown at 37°C in a humidified 5% CO_2 incubator. The medium was changed every 2–3 days. After 2 weeks, the cells were fixed and stained as outlined below.

7.3.4. Mesenchymal differentiation staining

To detect chondrogenic differentiation, induced BRCs were fixed in cold 100% methanol for 30 min and then exposed to 1% Alcian blue in 0.1 N HCl for 30 min. Cells were washed twice with 0.1 N HCl. Cells in PBS were viewed or stored at 4°C.

To detect mineralized matrix formation indicative of osteogenic differentiation, induced BRCs were fixed in 4% paraformaldehyde for 30 min, immersed in fresh 5% silver nitrate, and incubated in the dark for 30 min. After washing in water, the BRCs were exposed to ultraviolet light for 30 min followed by a 4-min incubation in 1% sodium thiosulfate to neutralize the silver nitrate. Cells were washed and stored in PBS at 4°C.

To detect adipogenic differentiation by identifying lipid vesicles, induced BRCs were fixed in 4% paraformaldehyde for 30 min and then immersed in 0.3% Oil Red O solution (in isopropanol) for 30 min. Cells were washed and stored in PBS at 4°C.

7.3.5. Alkaline phosphatase activity and detection

Early osteogenic differentiation was detected and quantified by alkaline phosphatase (ALP) staining and ALP enzyme assays. ALP activity was confirmed with reverse

transcriptase–polymerase chain reaction (PCR). Cells were plated at a density of 30,000 cells per well in 12-well plates. At 80% confluence, cells were induced with the osteogenic medium as described above. The medium was changed every 2–3 days and after 1 week, and ALP activity was measured.

To detect ALP activity, the BRCs were fixed in 70% ethanol for 30 min. They were then incubated with freshly made substrate containing naphthol AS-TR phosphate (Sigma) and Fast blue for 30 min. Cells were washed twice with PBS and then viewed or stored at 4°C.

To quantify the ALP activity and normalize the results, BRCs were lysed in Passive Lysis Buffer (Promega) according to manufacturer's instructions. Cell lysates were then sonicated, and centrifuged (10,000 rpm for 10 min at 4°C). The supernatant was recovered for the quantitative colormetric ALP assay [29], and the cell pellet was used for DNA isolation and the determination of the DNA concentration using the Quant-iT™ dsDNA BR Assay (Invitrogen) per the manufacturer's instructions.

7.3.6. Reverse transcriptase–PCR

To further confirm osteogenic differentiation, after 1 week of osteogenic induction total BRC cellular RNA was extracted, reverse transcribed, and amplified using osteoblast-specific gene primers: *Runx2*, osteocalcin (*OCN*), and bone sialoprotein (*BSP*). Media from the wells of induced BRCs were aspirated. Cells were immediately resuspended in 1 mL of Trizol (Invitrogen) and RNA was isolated according to the manufacturer's instructions. cDNA was synthesized using Invitrogen's SuperScriptII kit and oligo dT. PCR reaction components and concentrations were as described in the Invitrogen

Platinum Taq polymerase instructions using the primer sets below. An MJ themorcycler (MJ Resarch Model PTC-200) was used for the two PCR reaction conditions (Table 7.1).

7.3.7. Angiogenic potential

The angiogenic potential of BRCs was investigated through the fluorescent labeling of endothelial cells and capillary tube formation in culture. Collagen culture dishes were prepared by dispensing 2.5 mL of an ice-cold collagen solution, containing 2.4 mg/mL PureCol® bovine collagen (Advanced BioMatrix) in PBS at pH 7.4 into 60 mm plates. Collagen plates were solidified at 37°C for 90 min and then equilibrated in the growth medium for 2 h. BRC cultures were plated with 200,000 BRCs and incubated overnight at 37°C. One day after plating the cells, the medium was changed with a medium containing 50 ng/mL VEGF (R&D #293-VE). The medium was changed every 2–3 days. After 1 week, cells were fed the medium containing 10 μg/mL fluorescently labeled lipoprotein (DiI-Ac-LDL; Biomedical Technologies) for 4 h at 37°C to specifically label the endothelial cells. The medium was aspirated and the cells were washed three times with PBS before being fixed in 4% paraformaldehyde for 60 min. After fixing, the cells were washed three times with water before 3 mL of PBS was added to each plate, and then viewed or stored at 4°C.

To measure angiogenic cytokine production, BRCs from a subset of eight subjects were centrifuged to pellet the cells, and resuspended in X-Vivo 15 (Lonza) medium. X-Vivo 15 is a serum-free medium that was used in these assays to eliminate potential serum interference and nonspecific binding with some of the reagents (i.e., lack of human specific antibodies) used in the assays. All fractions were quantified and diluted to 1×10^6

mL^{-1} in X-VIVO 15 medium. The cells (100 µL) were added to the wells of a 96-well round-bottom plate in triplicate. The culture medium alone or supplemented with 300 ng/mL endotoxin lipopolysaccharide was added in a volume of 50 µL to all wells. Twent-four hours later, 100 µL of supernatant from each well was collected and stored at −70°C until analysis. Human Cytokine/Chemokine LINCOplex kits (Millipore Corporation) were used for multiplex analysis of VEGF and IL-8 concentrations in BRC supernatant fluids. The kits were used for cytokine determination as defined by the manufacturer's protocol (HCYTO-60K-Rev. 12/07/05) located at the following link:

www.millipore.com/userguides.nsf/a73664f9f981af8c852569b9005b4eee/09dc59783f6430ab85257259004f0203/$FILE/hcyto-60k.pdf.

ELISA kits (R&D Systems) were used to quantify the individual analytes Tie-1 and Tie-2 according to the manufacturer's protocol.

7.3.8. Surgical transplantation of BRCs to a localized craniofacial osseous defect

A nonrestorable tooth was extracted under local anesthesia from a patient in need of tooth extraction due to dental decay and periodontal disease associated with the tooth. Due to the preexisting condition of the tooth, its removal resulted in an area of a localized bone defect. According to a protocol approved by the U.S. FDA and the University of Michigan's Institutional Review Board, a full-thickness mucoperiosteal flap was elevated for access and hemostasis of the surgical defect achieved. One milliliter of the BRC cell suspension (approximately 1.5×10^7 cells/mL) was absorbed onto a gelatin sponge (Gelfoam; Pfizer) sized to a dimension of ≈2 cm^3. The sponge was then transplanted into

the extraction site to the level of the interproximal bone. The flap was then coronally repositioned, and a bioabsorbable collagen barrier membrane (Biomend®; Zimmer Dental) was placed over the sponge to contain the cell construct. The tissues were approximated and closed with a 4-0 bioabsorbable suture material. The subject was prescribed 500 mg amoxicillin, three times a day (t.i.d.) for 7 days, decreasing doses of dexamethasone (8, 4, 2, 2 mg) for 4 days, and 600 mg Ibuprofen four times a day (q.i.d.) for 3 days. Surgical reentry of the treated osseous defect was performed 6 weeks postsurgery, and a bone core of 2×7 mm was harvested with a trephine drill (Ace Surgical Supply Co., Inc.). To ensure harvesting of bone from the area where the BRCs were grafted, pre- and postsurgical measurement templates were used to identify the area corresponding to the center of the previous extraction socket. The core was prepared for microcomputed tomography (μCT) imaging and descriptive histological evaluation.

7.3.9. μCT and histology

The nondecalcified core was captured with the scanning direction parallel to the longitudinal axis of the core specimen. High-resolution scanning with an in-plane pixel size and slice thickness of 24 μm was performed. To cover the entire thickness of the bone core biopsy, the number of slices was set at 400. GEMS MicroView® software was used to make three-dimensional (3D) reconstructions from the set of scans as previously described [30].

After scanning, the core was decalcified for 2 weeks in 10% ethylenediaminetetraacetic acid. After decalcification, the core was transferred to 70% ethanol stored at 4°C until

ready for embedding in paraffin. Standard hematoxylin and eosin staining was performed to assess bone morphology and blood vessel formation.

7.3.10. Statistical analysis

Statistical analysis was performed with the use of Instat software (GraphPad Software). All data were plotted as mean ± standard error of the mean, unless otherwise noted. Statistically significant differences were determined by two-tailed Student's *t*-tests, and statistical significance was defined as $p < 0.05$.

7.4. RESULTS

7.4.1. Phenotypic characterization of BRC population

For all BRC formulations produced after cell processing, flow cytometry was performed to characterize the phenotype of the BRCs, and in some instances, the initial BMMNCs were also assessed before production of BRCs. For 10 subjects from whom BRCs were produced, including the subject treated with BRCs in this study, cell surface marker expression of the final BRC product is shown (Table 7.2). There are high percentages of CD31+, CD90+ (Thy1), and CD105+ cells. When compared to cell surface marker expression from typical BMMNC fractions used to produce these cells (unpublished proprietary data), CD90+ (Thy1) and CD105+ are highly enriched in the BRC product.

7.4.2. Mesenchymal potential of BRCs

BRCs were assessed for their capacity to differentiate toward different cellular lineages after culture under adipogenic, chondrogenic, and osteogenic conditions. After 2 weeks of culture, BRCs were subjected to Oil Red O, Alcian blue, and von Kossa staining. In control culture conditions, Oil Red O, Alcian blue, and von Kossa staining were all negative. In adipogenic conditions, Oil Red O staining was used to detect intracellular lipid-rich vacuoles and morphological changes in cell shape. The results confirmed that cells were differentiated toward an adipogenic lineage (Fig. 7.2a). Similarly, in cells grown under chondrogenic conditions, the presence of chondrogenic proteoglycans was indicated by positive Alcian blue staining (Fig. 7.2a), confirming chondrogenic differentiation. Under osteogenic culture conditions, deposition of mineralized matrix indicative of osteoblasts was evident through positive von Kossa staining (Fig. 7.2a). To

further evaluate osteogenic differentiation, alkaline phophatase activity was also analyzed qualitatively and quantitatively after 1 week of culture in osteogenic conditions (Fig. 7.2b). With ALP staining, there was a significantly more robust and widespread degree of staining in the osteogenic conditions relative to the control culture conditions. When this difference was measured quantitatively, there was a significant threefold increase ($p < 0.05$) in ALP activity in osteogenic relative to control conditions. Commitment toward an osteogenic lineage was further confirmed through gene expression of *Runx2*, *OCN*, and *BSP* (Fig. 7.2c), and although *Runx2* was expressed at a lower level in the control condition (data not shown), *OCN* and *BSP* were not detectable in control conditions at this timepoint.

7.4.3. Angiogenic potential of BRCs

In addition to standard phenotypic marker characterization of the final BRC product (shown from 10 patients treated with BRCs in Table 7.2), further analysis was performed on BRC products produced from smaller subsets of healthy volunteer subjects who provided donor marrow specifically to evaluate marker expression of angiogenic phenotypes. First, phenotypic comparison of cell surface marker expression was made between the starting BMMNCs and the final BRC product from a subset of four subjects. After expansion of the BMMNCs using the BRC process, the enrichment of vascular phenotypes in BRCs is shown in Table 7.3. Cell surface expression of vascular phenotypes associated with endothelial cells (Angiopoietin and flt1) and pericytes (Thy1+ and MUC-18) are all highly enriched. Next, when BRCs from a subset of eight volunteer donors (from the 10) were cultured in a medium (X-VIVO) without addition of

VEGF, cells were shown to produce appreciable levels of potent angiogenic cytokines VEGF, and angiopoietin (Ang)-1 and -2 (Fig. 7.3a). It should be noted that none of these cytokines were detected in the supernatant from the initial BMMNCs used to produce BRCs. Another angiogenic cytokine, interleukin-8 (Il-8), was produced by BRCs at a concentration (7.5 ng/mL/100,000 cells) significantly higher than that in the initial BMMNCs (4.6 ng/mL/100,000).

To examine the differentiation of BRCs into endothelial and vascular cells, BRCs were cultured in 3D collagen gels in the presence of VEGF. In these assays, VEGF is typically incorporated to induce endothelial cell differentiation [31-33]. Over the course of 1 week, cells elongated and formed spindle-like interconnecting structures resembling those seen by endothelial cells forming capillary tubes when grown under similar culture conditions (i.e., 3D extracellular matrices) (Fig. 7.3b). To further confirm the differentiation of BRCs into endothelial cells, a fluorescently labeled lipoprotein (DiI-Ac-LDL) that is metabolized specifically by endothelial cells was added to BRC 3D cultures. After 4 h of incubation with DiI-Ac-LDL, cells were examined under fluorescence microscopy and demonstrated uptake of the fluorescently labeled dye (Fig. 7.3c and 3d), characteristically seen by endothelial cells [34]. Taken together, these data demonstrate that BRCs have the capacity to differentiate into endothelial cells in 3D extracellular matrices and produce soluble angiogenic factors.

7.4.4. Clinical osteogenic and vascular regenerative potential of BRCs

The ultimate test of the osteogenic and angiogenic potential of BRCs is their ability to regenerate bone and vascular structures in a clinical model. To address this clinical

situation, we grafted BRCs into an osseous defect of the jawbone. After tooth extraction, a bone defect resulted in the area that the tooth previously occupied. The BRCs (in liquid suspension) were carefully placed (Fig. 7.4a) onto a resorbable material matrix (gelatin sponge) to the point of saturation (Fig. 7.4b). Cells were allowed 15 min to adhere to the gelatin sponge before their placement into the recipient graft site. After the extent of the bone defect (created as a result of tooth removal) was assessed (Fig. 7.4c), the sponge matrix containing the BRCs was grafted into the bone defect (Fig. 7.4d), a collagen membrane was placed for containment of the graft (Fig. 7.4e and 4f), and the area then closed with sutures and allowed to heal for 6 weeks.

After 6 weeks of healing, the grafted defect site was reentered for examination of regenerated tissue and dental implant placement. Clinical examination revealed the appearance of bone tissue, with no evidence of the previous bone defect (Fig. 7.5a), and a core biopsy was harvested from the center of the area in which the BRCs were grafted. Upon retrieval of the specimen with the trephine drill, it was found that the tissue was very dense, indicative of mature bone tissue (Fig. 7.5b). The clinical appearance of the biopsy specimen clearly showed a highly vascular tissue that, consistent with retrieval of viable bone tissue, produced bleeding after harvest (Fig. 7.5c). μCT analysis was performed on the biopsied tissue, and 3D reconstruction of the specimen showed highly mineralized tissue throughout the entire length of the core (Fig. 7.5d). After this analysis, histology was performed on the specimen and hematoxylin and eosin staining clearly showed widespread distribution of mature bone tissue with an abundance of blood vessels distributed throughout (Fig. 7.5e). These results provide preliminary evidence that BRCs,

produced from BMMNCs, have the regenerative capacity to produce highly vascular bone tissue in a human craniofacial bone defect.

7.5. DISCUSSION

Cell transplantation of stem cells has tremendous potential for craniofacial regenerative applications; yet, identification of the appropriate cell types and cell processing protocols are two of the most critical determinants in producing successful outcomes. In the present study, our aim was to assess the capacity of a cell production process, which utilizes an automated closed-system bioreactor, to produce clinical-scale numbers of autologous cells (BRCs) capable of regenerating clinically viable bone. Through cell surface marker characterization of BRCs, it was determined that the SPP *ex vivo* cell expansion processing of bone marrow aspirate was capable of producing cell populations highly enriched for mesenchymal and vascular progenitor cells. This was confirmed through cell characterization of BRCs, where cells within this heterogeneous population demonstrated the capacity to be induced to differentiate down chondrogenic, adipogenic, osteogenic, and angiogenic lineages. Finally, the test of the clinical regenerative capacity of BRCs demonstrated their ability to regenerate highly vascular bone in a human jawbone defect.

The cell-processing system employed to produce these cells utilizes an SPP protocol [20, 22, 25, 35]. Gastens *et al*. [35] examined this system and its ability to expand bone-marrow-derived cells to produce clinical-scale cell numbers. These initial studies compared cell phenotypes of cells produced with this closed SPP system to phenotypes of cells cultured with an open system utilizing conventional tissue culture parameters. Although mesenchymal cell numbers were observed to be higher in cells cultured with the SPP closed system, the limitation of the study was that the initial BMMNC fractions tested in the two different systems came from different donors; thus, differences observed

between the final cell products could have been, at least in part, attributed to donor–donor variability. In the present study, although we did not compare cell populations from closed and open culture systems, we did compare BRCs directly to the phenotypes of the BMMNCs from which they were produced. The final BRC population showed marked enrichment for mesenchymal and vascular cell phenotypes, suggesting that for therapeutic regenerative strategies, the SPP process supports the production of a more favorable cell population for transplantation than protocols using transplants comprised of unfractioned, whole bone marrow. Although there is often a wide degree of variability in the phenotypic expression of these markers from donor to donor, the relative differences in cell phenotype before and after cell processing is consistent in that the final product is enriched in expression of mesenchymal and angiogenic phenotypes after cell processing with the SPP system. Additional studies need to be performed comparing cell phenotypes and differentiation potential of cells derived from the same donor, when processed with either this closed system or a traditional tissue culture open system technique. It is also important to note that although the objectives of the differentiation assays were to examine the osteogenic and angiogenic potential of the BRCs, it is not possible to regrow or resume culture of cells in the Replicell system once they have been removed from the system. As such, further culture of BRCs required conventional tissue culturing techniques. However, it is recognized that this additional culture step could have potentially resulted in a cell population not identical to the population produced from the Replicell system; yet, because the Replicell system is a closed system, there is not a viable alternative to performing or adapting the aforementioned assays to cells cultured while in the Replicell system.

The ability of the SPP process to form bone-forming cells has also been recently studied *in vitro* and in ectopic animal models [26]. In these studies, the levels of bone formation seen *in vivo* followed the same trends of the osteogenic differentiation observed *in vitro*. Additionally, cell surface markers, including CD90+ (Thy1) and CD105+ (endoglin), were positively correlated with ectopic bone formation in mice. CD105, originally identified as a marker of mesenchymal stem cells [36], has more recently been associated with vascular endothelium in angiogenic tissues [37] and expression of CD90 has been linked to bone marrow subpopulations of colony-forming mesenchymal stem cells (CFU-F, colony-forming unit–fibroblasts) [38]. In our study, cell surface marker expression of BRCs from the subject who underwent cell transplantation in the bone defect showed 65-fold and 5-fold increases in CD90+ and CD105+, respectively (data not shown). This served as an indication that the BRC product was highly enriched with cells possessing mesenchymal and angiogenic potential and is in accordance with previous reports demonstrating enrichment of theses cell types with this cell-processing protocol [26, 35].

Although the cell product is highly enriched for vascular and mesenchymal cells as indicated by cell surface marker expression and *in vitro* differentiation capacity, it is clear that *in vitro* osteogenic differentiation of cell populations does not guarantee bone-forming capacity *in vivo*. Meijer *et al*. performed a clinical study evaluating the repair of jawbone defects in six subjects treated with autologous cells expanded using an open system [39], similar to the protocol used in traditional tissue culture of mesencyhmal stem cells [40, 41]. In this study, cells were cultured anywhere from 12 to 25 days before

implantation and the last 7 days in culture cells were grown on a mineral substrate, hydroxyapatite (HA) particles, in the presence of the osteoinductive agent dexamethasone. When cells grown under these osteogenic conditions were analyzed for their osteogenic capacity, all six bone marrow specimens produced cells capable of osteogenic differentiation *in vitro* (as determined by ALP expression) and bone formation *in vivo* (subcutaneous implants of HA/cell constructs in athymic mice). However, after implantation of these HA/cell constructs into various human jawbone defects of the six patients, biopsy specimens taken at 4 months showed that bone formation by implanted cells was able to regenerate bone in only one of the six patients treated. The authors made the important observation that *in vitro* osteogenic assays and bone formation in preclinical mouse models may not necessarily correlate to successful bone regeneration in the more challenging clinical applications. They concluded further that inadequate vascularity could have resulted in the reported disappointing outcome of the study [39]. In accordance with the authors' conclusion from this study, it is our belief that not only is vascularization from the host environment essential to clinical bone regeneration, but even further, that the angiogenic potential of the transplanted cells themselves should play an active role in this vascularization process.

The BRCs used to treat the human jawbone defect in our study were not produced in the presence of any osteogenic factors, and a gelatin sponge (with no known osteoinductive or osteoconductive properties) was used as a carrier matrix to transplant the cells, as opposed to a mineralized matrix such as HA. Additionally, the biopsy specimen harvested at 6 weeks showed significant new bone formation containing abundant blood

vessels. Although no direct evidence (i.e., labeling) is provided relative to the source of cells that produced the regenerated tissue, we make the assumption that the transplanted cells at least partly contributed to the regeneration because the bone core specimen analyzed was harvested from the central region of the defect and graft site. We were able to identify this exact region through the use of surgical measurement templates/guides. Yet, even still, despite these promising clinical results, the fact that they were obtained in a single patient can be viewed as a study limitation and minimizes the general conclusions that can be drawn. An additional note is that this case presentation is part of a larger, U.S. FDA-regulated, randomized, controlled Phase I/II trial where a larger number of patients are to be treated with BRCs. This larger study is still ongoing as it includes a 1-year patient follow-up; however, upon study completion, all the clinical data will be analyzed and the results outlined in a future report. While it is realized that the feasibility of this process for routine tooth extraction surgeries is most likely not practical, this study was conducted as an FDA Phase I/II study to examine safety and efficacy of this therapy for regeneration of craniofacial bone. If results are favorable, this type of therapy may certainly be feasible for larger, more challenging craniofacial reconstructions.

7.6. CONCLUSIONS

There is a growing interest in cell therapy strategies to regenerate craniofacial tissues, particularly bone. However, key questions to be considered in utilizing these strategies are the following: What is the source of cells used in these approaches? How will the cells be processed and expanded to reach appropriate cell numbers for clinical applications? What is the phenotype and regenerative capacity of the cells produced? Through the current investigation, we report a novel approach to craniofacial regeneration with the utilization of an automated, closed-system, cell expansion process for the clinical-scale production of autologous cells, enriched in mesenchymal and vascular cell phenotypes. Additionally, it was demonstrated clinically that these cells possess the capacity to give rise to highly vascular bone, 6 weeks after transplantation into a jawbone defect. Although the findings presented herein cannot fully elucidate the answers to the aforementioned questions, they provide important insight toward that end.

7.7. FIGURES

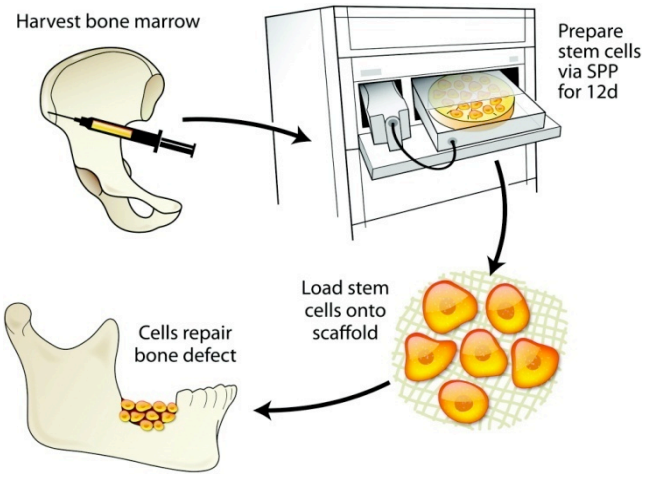

Figure 7.1. Bone repair cell (BRC) production. After harvest of bone marrow aspirates, cells are cultured using an automated, closed-system, single-pass perfusion (SPP) process. After 12 days of cell expansion in this bioreactor system, cells are packaged and delivered to the bone regenerative site on a biodegradable sponge.

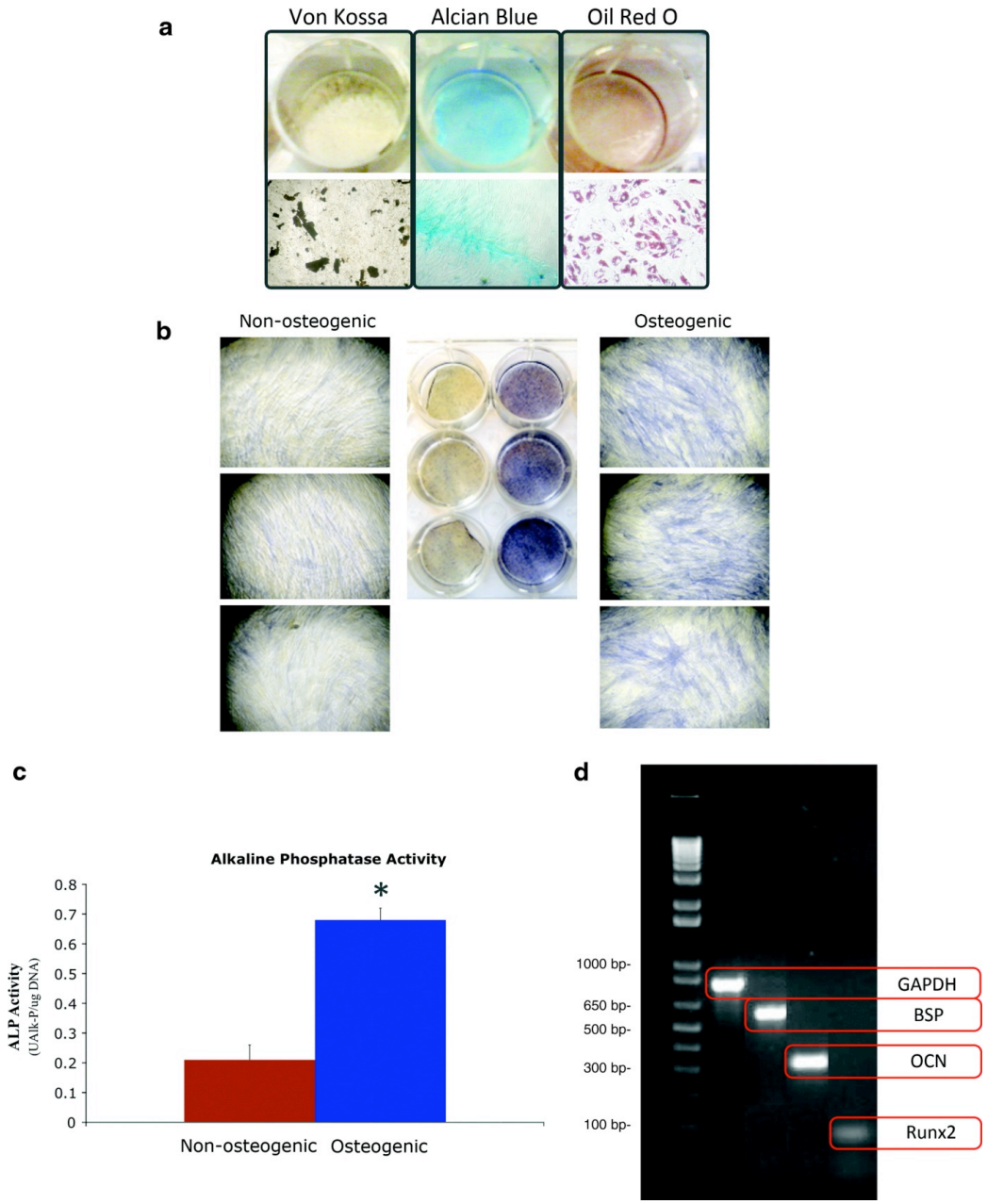

Figure 7.2. Multipotent and osteogenic potential of BRCs. (**a**) After induction of BRCs in osteogenic, chondrogenic, and adipogenic media, photographs and corresponding photomicrographs show multipotent mesenchymal differentiation as measured by phenotypic expression of osteogenic mineralized matrix (von Kossa), chondrogenic proteoglycans (Alcian blue), and adipogenic lipid vacuoles (Oil Red O);

low magnification images were taken at 40×; high magnification images are shown at 200×. (**b**) Osteogenic induction potential of BRCs is further evaluated qualitatively (staining) and (**c**) Quantitatively through measurement of alkaline phosphatase (ALP) activity of cells grown in the control medium versus cells grown in the osteogenic medium (*$p < 0.05$; alkaline phosphatase assays were performed in triplicate, and high-magnification nonosteogenic and osteogenic panels shown on the ends represent the same wells shown at lower magnification in middle panel); low magnification images were taken at 40×; high magnification images are shown at 200×. (**d**) BRC expression of bone-specific transcripts (*Runx2*, osteocalcin [*OCN*], and bone sialoprotein [*BSP*]) was also measured with reverse transcriptase–polymerase chain reaction.

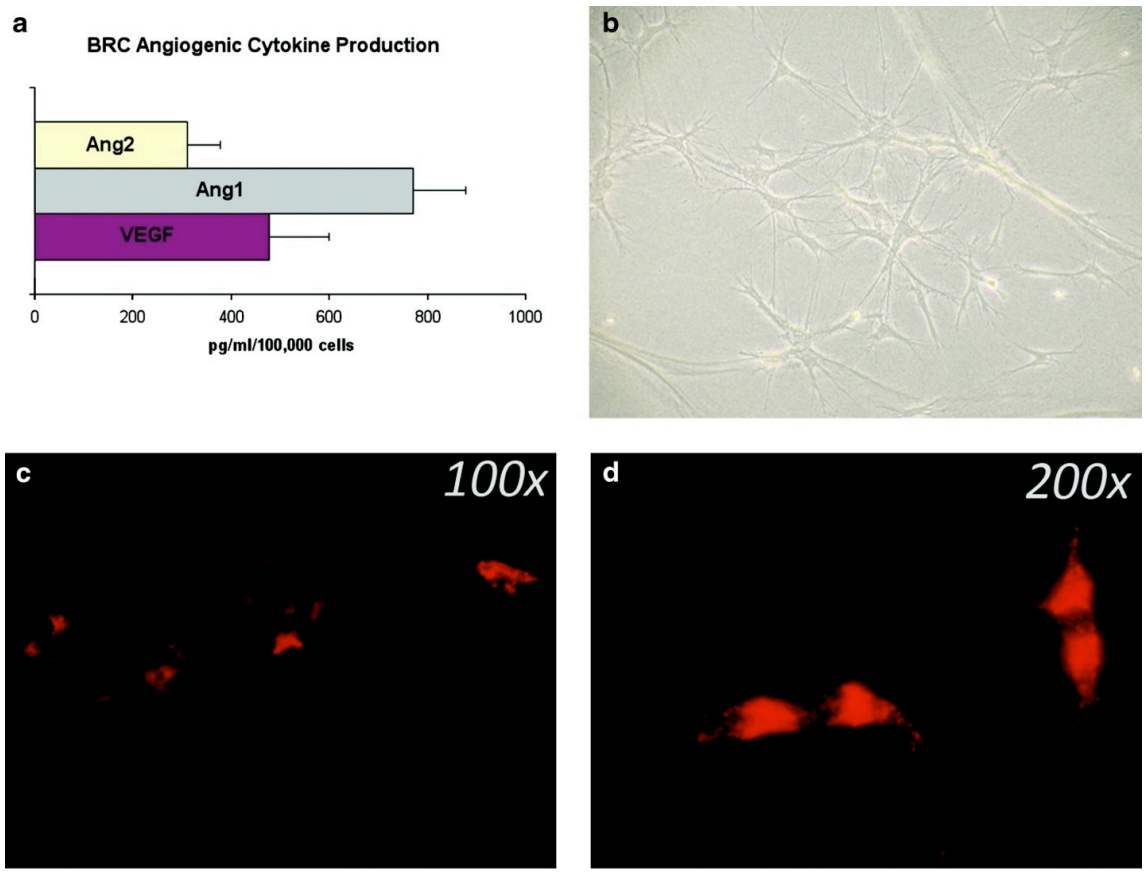

Figure 7.3. *In vitro* angiogenic phenotype of BRCs. (**a**) BRCs ($n = 8$) were shown to produce clinically appreciable levels of potent angiogenic cytokines, vascular endothelial growth factor (VEGF), and angiopoietin (Ang)-1 and -2. (**b**) After BRCs were cultured over 5 days in the presence of 50 ng/mL VEGF within three-dimensional collagen extracellular matrices, photomicrographs were taken and show sprouting structures indicative of endothelial cell capillary tube formation (100× magnification). (**c**) 100× and (**d**) 200× photomicrographs of fluorescently labeled BRCs after 4-h incubation with a (w/a) fluorescent-labeled lipoprotein (DiI-Ac-LDL) metabolized specifically by endothelial cells.

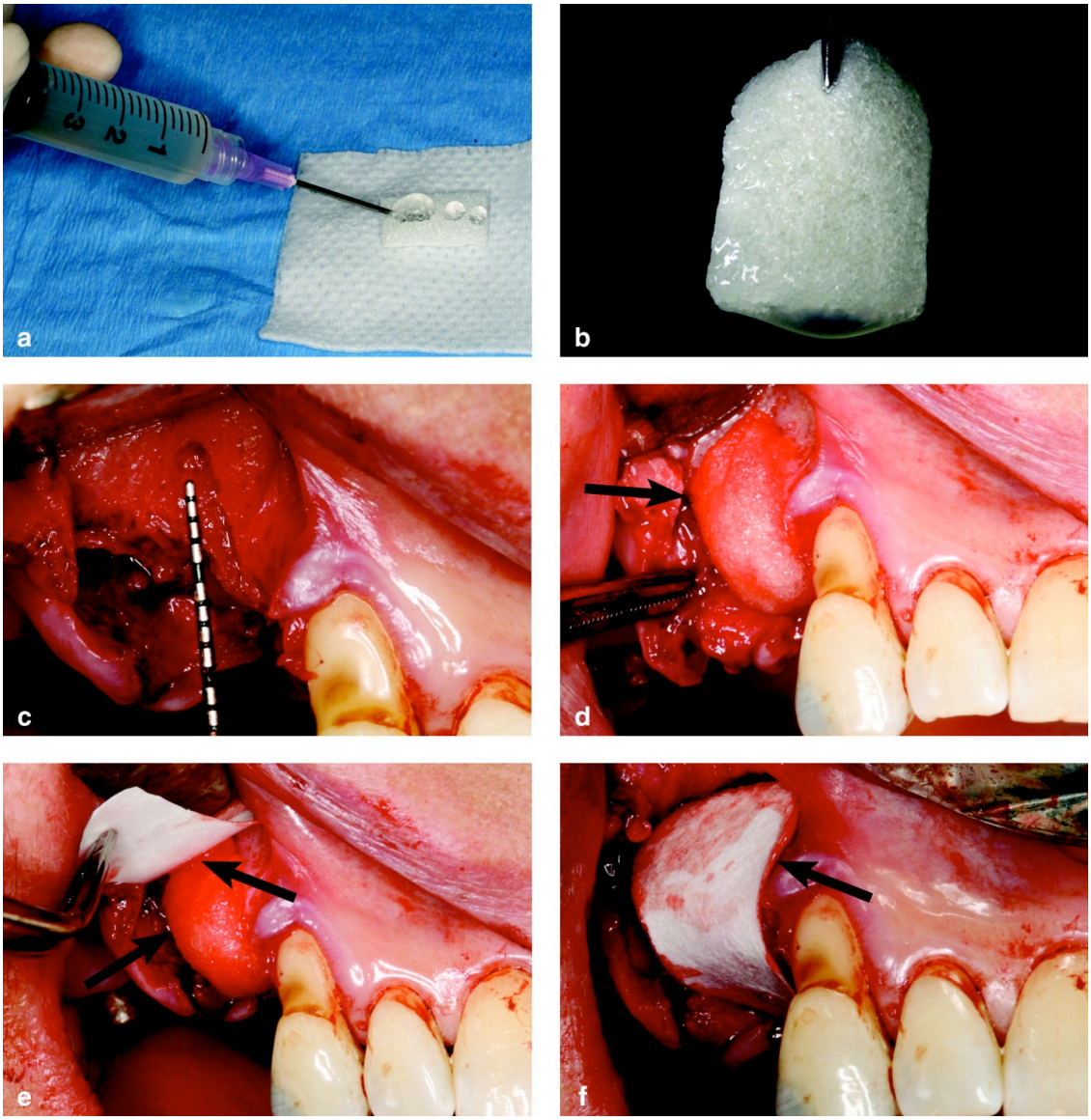

Figure 7. 4. Grafting of BRCs into localized jawbone defects. (**a**) Initial placement of BRCs onto gelatin sponge and (**b**) saturation of sponge with BRCs just before implantation into jawbone defect. Photographs of (**c**) jawbone defect after tooth removal, (**d**) placement of BRC-loaded gelatin into jawbone defect (arrows point to cell loaded gelatin), and (**e, f**) placement of a protective collagen membrane (arrows) for graft containment.

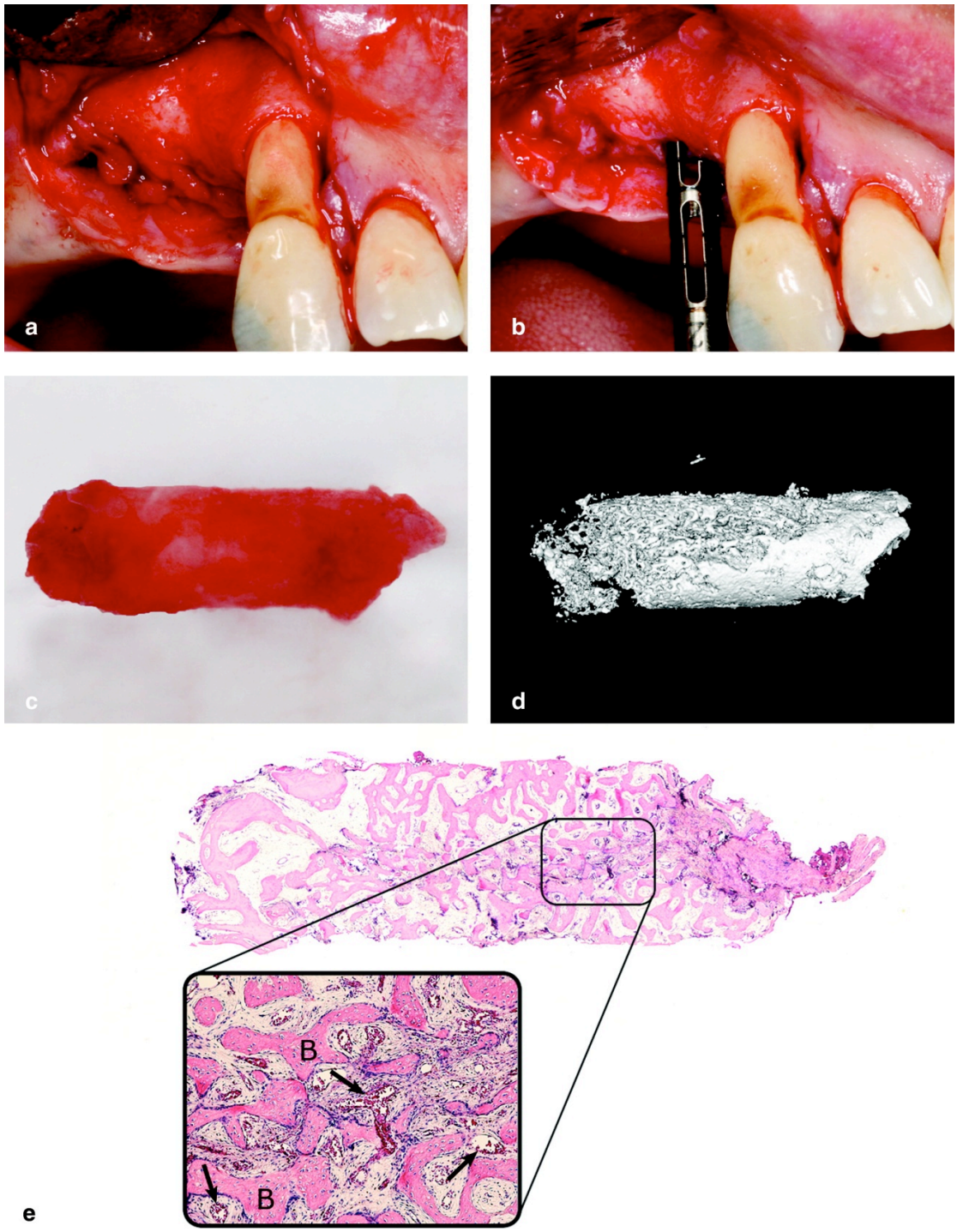

Figure 7. 5. BRC regeneration of highly vascular bone in jawbone defect. Photomicrographs of (**a**) regenerated jawbone defect 6 weeks after grafting of BRCs, (**b**) harvesting of bone core biopsy using trephine bur (just before placement of dental implant), and (**c**) bone core biopsy. (**d**) Microcomputed tomography three-dimensional

reconstruction of bone core biopsy from BRC-regenerated bone demonstrating mineralized tissue formation throughout specimen. (**e**) Histological evaluation (hematoxylin and eosin staining) of bone formation showing areas of mature cortical bone (B) with high vascularity, as indicated by abundance of blood vessels (arrows; low magnification at 4 × and high magnification at 200 ×).

7.8. TABLES

Primer name	*Primer sequence*	*Product size (bp)*	*Accession number*
BSP BSP FWD[b]	CTATGGAGAGGACGCCACGCCTGG	586	NM_004967
BSP REV[b]	CATAGCCATCGTAGCCTTGTCCT		
GAPDH FWD[a]	AGCCGCATCTTCTTTTGCGTC	815	NM_002046
GAPDH REV[a]	TCATATTTGGCAGGTTTTTCT		
OCN FWD[a]	CATGAGAGCCCTCACA	314	NM_199173
OCN REV[a]	AGAGCGACACCCTAGAC		
Runx2 FWD[b]	CCCGTGGCCTTCAAGGT	76	NM_004348
Runx2 REV[b]	CGTTACCCGCCATGACAGTA		

[a]94°C 2 min [94°C 45″ 56°C 45″ 72°C 1′] ×35 cycles 72°C 15′.
[b]94°C 2 min [94°C 45″ 67°C 45″ 72°C 1′] ×35 cycles 72°C 15′.

Table 7.1. Polymerase chain reaction primer pairs.

Phenotype	*BRC*	*SD*
% Viable (% 7AAD−)	92.69	2.16
% CD11b+	61.17	5.70
% CD66b+	28.20	7.50
% Lin-CD34+	0.61	0.35
% CD133+	0.38	0.13
% VEGFR2	6.15	2.39
% CD14 + Auto−	10.57	2.57
% CD14 + Auto+	16.81	6.89
% CD45+	79.24	3.39
% CD3+	14.24	5.41
% CD19+	0.81	0.47
% CD31+	65.61	5.69
% CD90 (Thy-1)+	17.00	2.85
% CD105+	20.20	1.85
% CD105 + CD90+	15.79	2.98
% CD90 + s that are 105+	94.44	3.05

BRC, bone repair cell; SD, standard deviation; VEGF, vascular endothelial growth factor.

Table 7. 2. Frequency of cell phenotypes in bone repair cells (n=10) produced by single-pass perfusion (Mean±Standard Deviation).

Phenotype	*Common name*	*Cell type recognized*	*BMMNC (mean ± SD)*	*BRC (mean ± SD)*	*Fold enrichment*
CD34+	—	HSCs/ECs progenitors	3.5 + 1.2	0.6 + 0.3	<1
CD133+	AC133	HSCs/ECs progenitors	1.2 + 0.2	0.5 + 0.2	<1
CD90+	Thy1	SSCs/pericytes	0.3 + 0.2	28.2 + 10.7	107.5
CD202b+	Tie2/Angiopoietin receptor	HSCs/ECs	7.3 + 4.8	35.7 + 6.3	4.9
—	VEGFR1/flt 1	Hematopoietic	6.5 + 2.0	38.9 + 4.7	6.0
CD144+	VE-Cadherin	Vascular ECs	2.5 + 2.4	0.9 + 0.6	<1
CD146+	MUC18, S-endo	ECs/pericytes	1.2 + 0.5	27.1 + 8.5	23.4

Values represent means taken from four different subjects. BMMNC, bone marrow mononuclear cell; HSCs, hematopoietic stem cells; ECs, endothelial cells; SSCs, skeletal (mesenchymal) stem cells.

Table 7.3. Presense and enrichment of vascular phenotypes in bone marrow mononuclear fraction and bone repair cell product.

7.9. REFERENCES

1. Langer, R., and Vacanti, J.P. Tissue engineering. Science **260,** 920, 1993.

2. Alsberg, E., Hill, E.E., and Mooney, D.J. Craniofacial tissue engineering. Crit Rev Oral Biol Med **12,** 64, 2001.

3. Kaigler, D., Cirelli, J.A., and Giannobile, W.V. Growth factor delivery for oral and periodontal tissue engineering. Expert Opin Drug Deliv **3,** 647, 2006.

4. Shi, S., Bartold, P.M., Miura, M., Seo, B.M., Robey, P.G., and Gronthos, S. The efficacy of mesenchymal stem cells to regenerate and repair dental structures. Orthod Craniofac Res **8,** 191, 2005.

5. Krebsbach, P.H., Kuznetsov, S.A., Satomura, K., Emmons, R.V., Rowe, D.W., and Robey, P.G. Bone formation *in vivo*: comparison of osteogenesis by transplanted mouse and human marrow stromal fibroblasts. Transplantation **63,** 1059, 1997.

6. Friedenstein, A.J., Ivanov-Smolenski, A.A., Chajlakjan, R.K., Gorskaya, U.F., Kuralesova, A.I., Latzinik, N.W., and Gerasimow, U.W. Origin of bone marrow stromal mechanocytes in radiochimeras and heterotopic transplants. Exp Hematol **6,** 440, 1978.

7. Ishaug-Riley, S.L., Okun, L.E., Prado, G., Applegate, M.A., and Ratcliffe, A. Human articular chondrocyte adhesion and proliferation on synthetic biodegradable polymer films. Biomaterials **20,** 2245, 1999.

8. Chang, F., Ishii, T., Yanai, T., Mishima, H., Akaogi, H., Ogawa, T., and Ochiai, N. Repair of large full-thickness articular cartilage defects by transplantation of autologous uncultured bone-marrow-derived mononuclear cells. J Orthop Res **26,** 18, 2008.

9. Marcacci, M., Kon, E., Moukhachev, V., Lavroukov, A., Kutepov, S., Quarto, R., Mastrogiacomo, M., and Cancedda, R. Stem cells associated with macroporous

bioceramics for long bone repair: 6- to 7-year outcome of a pilot clinical study. Tissue Eng **13,** 947, 2007.

10. Faundez, A.A., Taylor, S., and Kaelin, A.J. Instrumented fusion of thoracolumbar fracture with type I mineralized collagen matrix combined with autogenous bone marrow as a bone graft substitute: a four-case report. Eur Spine J **15 Suppl 5,** 630, 2006.

11. Gimbel, M., Ashley, R.K., Sisodia, M., Gabbay, J.S., Wasson, K.L., Heller, J., Wilson, L., Kawamoto, H.K., and Bradley, J.P. Repair of alveolar cleft defects: reduced morbidity with bone marrow stem cells in a resorbable matrix. J Craniofac Surg **18,** 895, 2007.

12. Ueda, M., Yamada, Y., Kagami, H., and Hibi, H. Injectable bone applied for ridge augmentation and dental implant placement: human progress study. Implant Dent **17,** 82, 2008.

13. Velardi, F., Amante, P.R., Caniglia, M., De Rossi, G., Gaglini, P., Isacchi, G., Palma, P., Procaccini, E., and Zinno, F. Osteogenesis induced by autologous bone marrow cells transplant in the pediatric skull. Childs Nerv Syst **22,** 1158, 2006.

14. Soltan, M., Smiler, D., and Choi, J.H. Bone marrow: orchestrated cells, cytokines, and growth factors for bone regeneration. Implant Dent **18,** 132, 2009.

15. Gerber, H.P., Vu, T.H., Ryan, A.M., Kowalski, J., Werb, Z., and Ferrara, N. VEGF couples hypertrophic cartilage remodeling, ossification and angiogenesis during endochondral bone formation. Nat Med **5,** 623, 1999.

16. Kaigler, D., Krebsbach, P.H., Wang, Z., West, E.R., Horger, K., and Mooney, D.J. Transplanted endothelial cells enhance orthotopic bone regeneration. J Dent Res **85,** 633, 2006.

17. Grellier, M., Granja, P.L., Fricain, J.C., Bidarra, S.J., Renard, M., Bareille, R., Bourget, C., Amedee, J., and Barbosa, M.A. The effect of the co-immobilization of human osteoprogenitors and endothelial cells within alginate microspheres on mineralization in a bone defect. Biomaterials **30,** 3271, 2009.

18. Kim, S.S., Park, M.S., Cho, S.W., Kang, S.W., Ahn, K.M., Lee, J.H., and Kim, B.S. Enhanced bone formation by marrow-derived endothelial and osteogenic cell transplantation. J Biomed Mater Res A **92,** 246, 2010.

19. Moioli, E.K., Clark, P.A., Chen, M., Dennis, J.E., Erickson, H.P., Gerson, S.L., and Mao, J.J. Synergistic actions of hematopoietic and mesenchymal stem/progenitor cells in vascularizing bioengineered tissues. PLoS ONE **3,** e3922, 2008.

20. Schwartz, R.M., Palsson, B.O., and Emerson, S.G. Rapid medium perfusion rate significantly increases the productivity and longevity of human bone marrow cultures. Proc Natl Acad Sci USA **88,** 6760, 1991.

21. Caldwell, J., Palsson, B.O., Locey, B., and Emerson, S.G. Culture perfusion schedules influence the metabolic activity and granulocyte-macrophage colony-stimulating factor production rates of human bone marrow stromal cells. J Cell Physiol **147,** 344, 1991.

22. Stiff, P., Chen, B., Franklin, W., Oldenberg, D., Hsi, E., Bayer, R., Shpall, E., Douville, J., Mandalam, R., Malhotra, D., Muller, T., Armstrong, R.D., and Smith, A. Autologous transplantation of *ex vivo* expanded bone marrow cells grown from small aliquots after high-dose chemotherapy for breast cancer. Blood **95,** 2169, 2000.

23. Pecora, A.L., Stiff, P., LeMaistre, C.F., Bayer, R., Bachier, C., Goldberg, S.L., Parthasarathy, M., Jennis, A.A., Smith, A.K., Douville, J., Chen, B., Armstrong, R.D.,

Mandalam, R.K., and Preti, R. A phase II trial evaluating the safety and effectiveness of the AastromReplicell system for augmentation of low-dose blood stem cell transplantation. Bone Marrow Transplant **28,** 295, 2001.

24. Whyte, M.P., Kurtzberg, J., McAlister, W.H., Mumm, S., Podgornik, M.N., Coburn, S.P., Ryan, L.M., Miller, C.R., Gottesman, G.S., Smith, A.K., Douville, J., Waters-Pick, B., Armstrong, R.D., and Martin, P.L. Marrow cell transplantation for infantile hypophosphatasia. J Bone Miner Res **18,** 624, 2003.

25. Jaroscak, J., Goltry, K., Smith, A., Waters-Pick, B., Martin, P.L., Driscoll, T.A., Howrey, R., Chao, N., Douville, J., Burhop, S., Fu, P., and Kurtzberg, J. Augmentation of umbilical cord blood (UCB) transplantation with *ex vivo*-expanded UCB cells: results of a phase 1 trial using the AastromReplicell System. Blood **101,** 5061, 2003.

26. Dennis, J.E., Esterly, K., Awadallah, A., Parrish, C.R., Poynter, G.M., and Goltry, K.L. Clinical-scale expansion of a mixed population of bone-marrow-derived stem and progenitor cells for potential use in bone-tissue regeneration. Stem Cells **25,** 2575, 2007.

27. Krebsbach, P.H., and Robey, P.G. Dental and skeletal stem cells: potential cellular therapeutics for craniofacial regeneration. J Dent Educ **66,** 766, 2002.

28. Pittenger, M.F., Mackay, A.M., Beck, S.C., Jaiswal, R.K., Douglas, R., Mosca, J.D., Moorman, M.A., Simonetti, D.W., Craig, S., and Marshak, D.R. Multilineage potential of adult human mesenchymal stem cells. Science **284,** 143, 1999.

29. Manolagas, S.C., Burton, D.W., and Deftos, L.J. 1,25-Dihydroxyvitamin D3 stimulates the alkaline phosphatase activity of osteoblast-like cells. J Biol Chem **256,** 7115, 1981.

30. Park, C.H., Abramson, Z.R., Taba, M., Jr., Jin, Q., Chang, J., Kreider, J.M., Goldstein, S.A., and Giannobile, W.V. Three-dimensional micro-computed tomographic imaging of alveolar bone in experimental bone loss or repair. J Periodontol **78,** 273, 2007.

31. Kaigler, D., Krebsbach, P.H., Polverini, P.J., and Mooney, D.J. Role of vascular endothelial growth factor in bone marrow stromal cell modulation of endothelial cells. Tissue Eng **9,** 95, 2003.

32. Nor, J.E., Christensen, J., Mooney, D.J., and Polverini, P.J. Vascular endothelial growth factor (VEGF)-mediated angiogenesis is associated with enhanced endothelial cell survival and induction of Bcl-2 expression. Am J Pathol **154,** 375, 1999.

33. Folkman, J., and Haudenschild, C. Angiogenesis *in vitro*. Nature **288,** 551, 1980.

34. Voyta, J.C., Via, D.P., Butterfield, C.E., and Zetter, B.R. Identification and isolation of endothelial cells based on their increased uptake of acetylated-low density lipoprotein. J Cell Biol **99,** 2034, 1984.

35. Gastens, M.H., Goltry, K., Prohaska, W., Tschope, D., Stratmann, B., Lammers, D., Kirana, S., Gotting, C., and Kleesiek, K. Good manufacturing practice-compliant expansion of marrow-derived stem and progenitor cells for cell therapy. Cell Transplant **16,** 685, 2007.

36. Haynesworth, S.E., Baber, M.A., and Caplan, A.I. Cell surface antigens on human marrow-derived mesenchymal cells are detected by monoclonal antibodies. Bone **13,** 69, 1992.

37. Fonsatti, E., and Maio, M. Highlights on endoglin (CD105): from basic findings towards clinical applications in human cancer. J Transl Med **2,** 18, 2004.

38. Boiret, N., Rapatel, C., Boisgard, S., Charrier, S., Tchirkov, A., Bresson, C., Camilleri, L., Berger, J., Guillouard, L., Guerin, J.J., Pigeon, P., Chassagne, J., and Berger, M.G. CD34+CDw90(Thy-1)+ subset colocated with mesenchymal progenitors in human normal bone marrow hematon units is enriched in colony-forming unit megakaryocytes and long-term culture-initiating cells. Exp Hematol **31,** 1275, 2003.

39. Meijer, G.J., de Bruijn, J.D., Koole, R., and van Blitterswijk, C.A. Cell based bone tissue engineering in jaw defects. Biomaterials **29,** 3053, 2008.

40. Caplan, A.I. Mesenchymal stem cells. J Orthop Res **9,** 641, 1991.

41. Goshima, J., Goldberg, V.M., and Caplan, A.I. The osteogenic potential of culture expanded rat marrow mesenchymal cells assayed *in vivo* in calcium phosphate ceramic blocks. Clin Orthop Relat Res **262,** 298, 1991.

CHAPTER EIGHT

BIOMIMETIC HYBRID SCAFFOLDS FOR ENGINEERING HUMAN TOOTH-LIGAMENT INTERFACES

Park CH, Rios HF, Jin Q, Bland ME, Flanagan CL, Hollister SJ, Giannobile WV.

Biomaterials, **2010** 31(23): 5945-5952

8.1. ABSTRACT

A major clinical challenge in the reconstruction of large oral and craniofacial defects is the neogenesis of osseous and ligamentous interfacial structures. Currently, oral regenerative medicine strategies are unpredictable for repair of tooth-supporting tissues destroyed as a consequence of trauma, chronic infection or surgical resection. Here, we demonstrate multiscale computational design and fabrication of composite hybrid polymeric scaffolds for targeted cell transplantation of genetically modified human cells for the formation of human tooth dentin-ligament-bone complexes *in vivo*. The newly-formed tissues demonstrate the interfacial generation of parallel- and obliquely-oriented fibers that grow and traverse within the polycaprolactone (PCL)-poly(glycolic acid) (PGA) designed constructs forming tooth cementum-like tissue, ligament, and bone structures. This approach offers potential for the clinical implementation of customized

periodontal scaffolds that may enable regeneration of multi-tissue interfaces required for oral and periodontal engineering applications.

8.2. INTRODUCTION

Collectively, periodontal disease afflicts over 80% of adults worldwide and nearly 15% display severe disease concomitant with early tooth loss [1]. In periodontitis, the detrimental changes that the tooth-supporting tissues undergo are primarily the result of specific microbial challenges [2]. These challenges in a susceptible host disrupt the functional and structural integrity of the tooth supporting apparatus and may progress to affect a number of systemic conditions [3]. Therefore, the periodontium represents a critical barrier that if breached by invasive pathogens, triggers local and systemic inflammatory responses that characterize oral infection.

Structurally, regeneration of the lost periodontium involves the formation of new cementum, periodontal ligament (PDL) and alveolar bone. However, the proper interfacial connection of this multi-tissue complex is what determines its function and stability in health. Its strength and mechanical integrity is the result of adequate PDL-fiber orientation and its incorporation to the newly formed bone and cementum. This interconnection allows the periodontal system to dissipate and translate the mechanical stimuli that are generated from the tooth to the surrounding structures [4]. Biologically, this arrangement facilitates crucial cell-matrix interactions, which within a mechanically dynamic environment, determines normal dental-alveolar adaptive responses [5]. Current available regenerative therapeutic approaches show promising results [6-8]. However, complete regeneration and adequate fiber organization in large defects remains a challenging and unpredictable clinical dilemma [9].

In regenerative medicine, many different factors have been reported to promote multiple tissue integration and cell/tissue directionality [10-16]. Novel approaches, such as the use of multi-phasic scaffold designs as well as stem cell therapies represent a significant step forward in tissue engineering [13, 14, 17, 18]. Today, the ability to establish a 3-dimensional polarity and patterning within a predetermined inherent scaffold geometry to guide and establish cell/tissue directionality is a feasible concept [15, 19-21]. Cell-based research has started to focus on designing and developing various physical and geometric approaches using biomaterials [22, 23]. However, the orchestration of multiple tissue formation, spatial fibrous tissue organization, and endpoint functional restoration using a single *in vivo* scaffold system remains a significant challenge. To address these limitations, a computational topology design and a solid free-form fabrication technique was used to create a hybrid periodontal-inspired model system containing PDL-specific and bone-specific polymer compartments [24, 25]

8.3. MATERIALS & METHODS

8.3.1. Hybrid scaffold design and fabrication

Periodontal ligament and bone architectures for the hybrid scaffold were designed and modeled with Unigraphics NX 5.0 (Siemens PLM software, Plano, TX USA). The designed structures were exported to the 3-D wax-printing system (ModelMaker II, Solidscape, Inc., Merrimack, NH USA) and manufactured using different wax molds (fig 1B). After dissolving the Protobuild (Solidscape, Inc.) of PDL mold by 70% ethanol, two different biopolymers poly(glycolic acid) (PGA; MW>100KDa, Polysciences Inc. Warrington, PA USA) and poly-ε-caprolactone (PCL; MW 43-50KDa, Polysciences Inc.). 25w/v% PGA was dissolved in 1,1,1,3,3,3-Hexafluoro-2-propanol (HFIP, Sigma-Aldrich®, St. Louis, MO USA) solvent and the solution was cast for PDL interface architecture. 25 w/v% PCL solution in acetone (Sigma-Aldrich®) was cast in the bone architecture mold. These 2 different manufactured and fabricated architectures were assembled with PCL thin film membrane and BioAct® VSO (Petroferm Inc. Gurnee, IL USA) was used to remove Protosupport (Solidscape Inc.) for 2 days. The rest of Protosupport and BioAct VSO were dissolved in 100% ethanol overnight and hybrid scaffolds were stored in 70% ethanol.

8.3.2. Human tooth dentin slice preparation

Healthy human teeth were extracted from patients as previously described by the University of Michigan-Institutional Review Board (UM-IRB)-approved protocol. Approximately 3.0 x 4.0 x 0.8 mm^3 dimensioned dentin blocks, which were fit into the PDL interface of the hybrid scaffold, were sliced and surface-treated by 37%

orthophosphoric acid to expose dentinal tubule topology and promote fibrous tissue attachment.

8.3.3. Cell cultures and gene delivery

Primary human gingival fibroblast (hGF) cells were provided as a kind gift from professor Martha Somerman (University of Washington, Seattle, WA USA). Passages 4-6 hGF cells were cultured in Dulbecco's Modified Eagle Medium (DMEM; Gibco BRL Life Technologies Inc., Grand Island, NY USA) supplemented with 10% fetal bovine serum (FBS; Gemini Bio-Products, Woodland, CA USA), antibiotics (100 units/ml penicillin and 100μg/ml streptomycin) and 2mM glutamine. During culturing in a humidified atmosphere of 5% CO_2 in air at 37°C, the hGF cells were transduced with AdCMV-BMP-7, recombinant adenovirus-encoding murine bone morphogenetic protein-7 (BMP-7), at a multiplicity of infection (MOI) of 500 and incubated for 1 day before cell seeding into the bone portion of hybrid scaffolds. Passages 4-6 human periodontal ligament cells (hPDL) were derived from tooth biopsy samples from 3 healthy human patients and cultured in media.

8.3.4. Cell seeding in the hybrid scaffolds

Bovine plasma fibrinogen (Sigma-Aldrich®) was dissolved in DMEM to make 5 mg/ml concentration and sterilized with a 0.2μm syringe filter (Nalgene®, Rochester, N.Y. U.S.A.). Bovine plasma thrombin (Sigma-Aldrich®) was dissolved in Hanks' Balanced Salt Solution (HBSS, Invitrogen™) at 100 U/ml concentration. For the bone region, $2.4x10^5$ BMP-7-hGF modified cells in the bone region and $1.4x10^5$ hPDL cells in the

PDL interface of hybrid scaffolds were suspended within fibrinogen solution. 1.6μl thrombin was pipetted on the PDL interface and 8.0μl hPDL-fibrinogen solution was dropped. After the gelation of the PDL interface, the treated tooth dentin slice was immediately positioned on the PDL scaffold. For BMP-7-hGF cell seeding, 3.0μl thrombin solution was pipetted inside of the bone architecture and 15.0μl hGF + fibrinogen solution was drop-wise added for fibrin gelation.

8.3.5. In vivo experimental design

Two different surgical pockets on the dorsa of immunodeficient 6 week-old NIH III nude mice (approximately 50-55g from Charles River Laboratories International Inc., Wilmington MA USA) were created. Four different groups were designed with 3 and 6 week time-points in order to implant surgically created subcutaneous pockets of the nude mouse with sample n-values=8-9/group for each time point. The experimental groups consisted of 1) no cell seeding, 2) hPDL cell-seeded in PDL interface, 3) Ad-BMP-7-hGF cell seeded in bone region, and 4) hPDL and Ad-BMP-7-hGF cell seeded in PDL interface and bone region of hybrid scaffolds, respectively. Ad-BMP-7-hGF was the adenovirus encoding BMP-7 transduced human gingival fibroblast cells. Under isofluorane anesthesia, dentin-associated hybrid scaffold complex was implanted subcutaneously into a surgically-created pocket and the incisions were approximated using surgical staples. All animals were euthanized with carbon dioxide (CO_2) prior to specimen harvest. All animal surgeries were performed under a protocol approved by the University of Michigan-University Committee on Use and Care of Animals (UM-UCUCA).

8.3.6. Quantitative micro-computed tomography (Micro-CT)

The harvested specimens were fixed in 10% buffered formalin phosphate solution for 1-2 days and transferred in 70% ethanol. The tissue-fixed specimens were scanned by micro-CT (GE Healthcare Inc., London, ON Canada) with 18 x 18 x 18 μm^3 voxel size. Based on the Hounsfield unit (HU) scale, mineralized tissue regeneration was quantified around the hybrid scaffold, bone region and PDL interface below the treated human tooth dentin slice by MicroView Analysis+ 2.1.2 (GE Healthcare Inc.). The region of interests (ROIs) for PDL interface and bone region were 3.5 x 4.5 x 0.8mm^3 and 5.0 x 6.0 x 3.0mm^3, respectively to assess quantification of mineralized tissue formation.

8.3.7. Histomorphometry for cementum-like tissue and tissue orientation formation

After the micro-CT scanning, harvested specimens were decalcified with 10% EDTA (Ethylenediaminetetraacetic acid, Sigma-Aldrich®) for 2 weeks and then paraffin-embedded for histology sections for hematoxylin and eosin (H&E) staining. Image-Pro plus software (Media Cybernetics Inc., Bethesda MD USA) was utilized to calculate length percentage of cementum-like layer on the human tooth dentin slice. The % length of cementum-like tissue formation ($l_{cementum}$) was determined by comparing the newly-deposited cementum length and the total dentin surface (l_{dentin}), which contacted to PDL interface of the hybrid scaffold.

$$\%\ of\ l_{cementum} = \left[\frac{l_{cementum}}{l_{dentin}}\right] \times 100$$

The orientation of fibrous cells and connective tissues in PDL interface was analyzed with four different indices, percentile of cellularity and orientation score (Fig. 4b). The best orientation was the perpendicular alignment to the dentin surface.

8.3.8. Scanning electron microscopy (SEM)

The scaffold constructs and dentin slices were washed, sonicated, dehydrated and the surface prepared for evaluation using the Environmental Scanning Electron Microscope (Philips XL30E SEM FEI Company, Hillsboro, OR USA). Briefly, after dehydration, the specimens were attached to a stub and sputtered with gold/palladium. The gold/palladium-coated specimens were examined by use of a FEI/Philips XL30 field emission environmental scanning electron microscope (SEM).

8.3.9. Immunofluorescence and immunohistochemical stainings

Tubulin and 4',6-diamidino-2-phenylindole (DAPI) staining were performed. Briefly, the samples were dissected and fixed in 4% paraformaldehyde at 4°C overnight, demineralized in 10% EDTA solution over 3 weeks, dehydrated, embedded in paraffin and processed for sectioning (6μm thickness). Fluorescence staining to tubulin (1:100 dilution; Abcam, Inc. Cambridge, MA) was performed on paraffin sections using an affinity purified rat monoclonal antibody. Immunological reaction was visualized by using a rabbit polyclonal secondary antibody to rat conjugated to Fluorescein isothiocyanate (FITC) (1:200 dilution; Abcam, Inc. Cambridge, MA). The Sections were then treated with an antifade agent containing DAPI (ProLong Gold antifade reagent with DAPI; Invitrogen Corporation; Eugene, OR) and covered with glass coverslip. The

stained slides were imaged using an OLYMPUS Fluroview 500 confocal microscope (Olympus America Inc; Center Valley, PA).

Immunostaining of Human Leukocyte Antigen (HLA) (1:200 dilution; Santa Cruz Biotechnology, Inc. Santa Cruz, CA) was performed on paraffin sections using an affinity purified goat polyclonal antibody. Immunological reactions were visualized by use of the goat ABC kit staining system and a peroxidase-diaminobenzidine reaction (Santa Cruz Biotechnology, Inc. Santa Cruz, CA). Sections were counterstained with hematoxylin and mounted on glass slides. Negative controls were obtained by substituting the primary antibody with serum.

8.3.10. Customized, reversed-engineered scaffold design

After iCAT-CT (Xoran Technologies® Inc.; Ann Arbor MI USA) scanning of a porcine periodontal defect site with the 200μm voxel-size resolution, the DICOM file was transferred to a STL file format to import CAD-based Unigraphics NX 5.0. Based on the tooth root-surface, micro-channels perpendicularly oriented to the root surface were designed and booleaned with STL-formatted in order to generate a similar surface-morphology. Approximately, the dimension of PDL interface was 300μm-thick (Fig. 8; red-colorized architecture) to cover from the apical side of periodontal defect to cemento-enamel junction (CEJ). After the hybrid scaffold, rapid prototyping technology was utilized to manufacture the molds to cast polymer. 25wt/v% PCL solution was casted into to printed wax molds and fabricated polymeric scaffold was placed to the periodontal defect to scan micro-CT to evaluate adaptation of defect geometry.

8.3.11. Adaptation evaluation of Hybrid scaffold-tooth root surface using the contrast agent and micro-CT

After the customized hybrid scaffold was designed and manufactured, 35% barium sulfate ($BaSO_4$) in distilled water was used to coat the 25% PCL hybrid scaffold to obtain the higher intensity and grayscale Hounsfield Unit. Surgically created periodontal defect region was harvested and scanned with/without the scaffold using micro-CT, which set up for 25 x 25 x 25μm^3-voxel size resolution. On the 2-D coronal cross-sectioned view, 3.00mm distance from the interface between the dental pulp and tooth dentin was selected to generate the grayscale-based histogram. This region covered from the tooth root, PDL interface, and middle of bone region. Adaptation ratio was linearly calculated using the entire length of PDL interface (d^{total}) and the gap distance (d^{gap}) between tooth dentin surface and the surface of PDL interface architecture in the hybrid scaffold.

$$Adaptation\ Ratio = \left[\frac{d_{l}^{total} - d^{gap}}{d^{total}}\right]$$

The scaffold had six different layers and each layer had three PDL channel-like structures (n=3 per layer).

8.3.12. Statistical analysis

The PASW Statistics 17.0 (SPSS Inc. Chicago, IL USA) was used for statistical analysis. Nonparametric two-tailed Kruskal-Wallis one-way ANOVA for unequal variance (Table 8.1). After the overall determination of statistical results from the Kruskal-Wallis test,

pair-wise Mann-Whitney U-test were utilized to define the statistical differences among groups. We demonstrated the results were significantly different with the α value set at 0.05 level of significance.

8.4. RESULTS

A 0.8mm thickness PDL interfacial structure was designed with multiple perpendicularly oriented channels, devised for the guidance of fibrous connective tissue formation and alignment of fibroblast-like cells (Fig. 8.1a). The structure was fabricated in 25% poly(glycolic acid) (PGA), a hydrophilic and rapid degradable biomaterial. For the bone compartment, a global porous geometry with approximately 0.75 x 0.50 x 0.05 mm^3 dimensions using 25% poly-ε-caprolactone (PCL) was designed (Fig. 8.1a). The PDL and bone components were then fused with a 15% PCL thin layer to form one single hybrid scaffold structure.

The new scaffold design was evaluated using an *in vivo* model system. For this model, acid-treated human tooth dentin slices were sectioned to fit the PDL dimension and provide an avascular tooth surface with close proximity to the PDL microchannel-grooved scaffold design (Fig. 8.1b). The four different hybrid scaffold-dentin complexes were subcutaneously implanted in the dorsa of immunodeficient mice. The bone and PDL regeneration capacity was evaluated and the feasibility to adapt the model hybrid scaffold designed to the irregular periodontal defect topography was also determined.

Micro-computed tomography (micro-CT) and serial histological sections were utilized for the qualitative and quantitative assessment of the mineralized tissue formed and to evaluate potential invasion of bone within the PDL region (Fig. 8.2; [26]. The 3-D reconstructed images provided qualitative information regarding the patterning and spatial distribution of the newly formed bone in relation to the scaffold geometry (Fig.

8.2; colorized micro-CT images). Bone volume fraction (BVF) and bone mineral density (BMD) were quantified using grayscale Hounsfield Units (HU). Specified regions of interest (ROIs) for PDL interface and bone region were created in 3.5 x 4.5 x 0.8mm^3 and 5.0 x 6.0 x 3.0mm^3 dimensions, respectively. A robust mineralized tissue formation was observed in the groups containing the transduced osteogenic factor. These groups within the bone region demonstrated statistically significant higher values for BVF and BMD (*$p<0.05$ and **p-value<0.01; Fig. 8.3a and b). On the other hand, the only bone formed outside the bone region, was localized to the peripheral surface of the scaffold and dentin construct. No bone was found to be invading the PDL at either of the two time points for non BMP-treated constructs (Table 8.1). Histological evaluation of the PDL and bone regions provided further evidence of the lack of osteogenesis within the PDL region while corroborating the presence of bone within the other compartment (Fig. 8.2).

Hematoxylin and eosin (H&E) serial images of the PDL-dentin interface were histomorphometrically evaluated to determine the length of new cementum formation (Fig. 8.3). At 3 weeks, limited evidence of cementum-like tissue deposition was observed. However, at 6 weeks the length of cellular cementum in the groups transduced by with BMP-7 were significantly greater compared to the other groups. (Fig. 8.3c and d, *$p=0.024$ and **$p=0.007$). The histomorphometric analysis showed that new cementum-like tissue formed in 20.62% of the hPDL/BMP-7-hGF cell-seeded group and 17.70% of BMP-7-hGF cell-seeded group, compared with 0% and 1.2% of the no cell and hPDL-seeded groups, respectively (Fig. 8.3c). Interestingly, the newly formed cementum was observed in association with vascular structures and fibrous connective tissue (Fig. 8.3d).

The associated fibrous tissue is speculated to represent a transition cue of the cementogenesis process on the dentin surface and the initial integration of fibrous bundles to the dentin slice [27].

These findings are particularly important as they emphasize the potential biological effect of the hybrid scaffold system. The designed PDL interface architecture was initially conceived to increase angiogenic development and enhance biological molecule diffusivity. This theoretical concept is supported by the *in vivo* findings, which reflect an increased number of vascular structures and mature fibers oriented along the patterned surface scaffold architecture (Figs. 8.2 & 8.4). This was especially observed in the two different hPDL cell-seeded groups. At 3 weeks, these observations were primarily reflected in the BMP-7 transduced groups (Fig. 8.4). However, by the 6^{th} week, a more generalized increased level of tissue orientation was observed in different proportions for all groups (Fig. 8.4).

To evaluate the viability of the human-seeded cells within the scaffold complex, the harvested constructs were immunostained for human leukocyte antigen-A (HLA-A). Distinct membrane staining was noted in the PDL and bone regions of the groups where human cells were transplanted. These groups of cells within the PDL were preferentially localized along the polymer architecture and at the center of more mature fibrillar structures. Within the bone scaffold region, the HLA-A positive cells were clearly localized primarily around the new bone surface and presented an osteoblast-like phenotype. Multiple osteocyte like cells were also positive for HLA-A (Fig. 8.6).

5.5. DISCUSSION

The current system still has limitations compared to the highly complex native multi-tissue formation [12-14], especially bone-PDL-tooth complex [9, 28, 29]. One of the most important variables is the lack of a mechanically-modulated environment as well as a symmetric design which does not completely reflect the irregular and complex morphology of typical periodontal defects [4]. Therefore, supported by the biological advantages demonstrated in this novel hybrid scaffold, a more periodontally relevant design was constructed using surgically created defects in porcine mandibulae to determine the ability to conform to the anatomical specifications of the periodontium (Fig. 8.5). The customized scaffold displayed perpendicularly oriented internal channel-structures within the PDL portion and a similar bone topology in the open-box format to follow and coalesce with the adjacent residual bone. The inter-root defect scaffold was designed to possess two separate components with a key (buccal)–lock(lingual) system to make easier the assembling and adaptation through the defect region (Fig. 8.5a). The adaptability/fitting of the fabricated scaffold was evaluated using 3-D and cross-sectional analysis to establish the approximation of the scaffold construct in relation to the periodontal tissues and defects (Fig. 8.5b-d). This possibility of customization and, therefore, guidance of each tissue represents an additional advantage with a significant clinical relevance.

Together, these observations support the added value of designing a compartmentalized hybrid scaffold with biomimetic architecture to influence cell behavior and tissue orientation. The combined hPDL cells and Ad-BMP-7-hGF cells not only surpassed

most of the measured variables when compared to the other test groups, but also produced a more predictable formation of tissue similar to healthy periodontium. Therefore, our principal finding was that a combinational system of hPDL fibroblast-like cells and osteogenic stimulation can enhance the regeneration of the multi-layered periodontal complex. This approach offers strong potential for an "off-the-shelf scaffold construct for repair of oral and craniofacial defects.

8.6. CONCLUSIONS

We demonstrate the consistent generation of newly-formed tissues possessing interfacial neogenesis of parallel- and obliquely-oriented ligamentous fibers that sprout and traverse through the polymer designed constructs forming tooth cementum-like tissue, ligament, and bone structures. This approach offers potential for the clinical implementation of customized periodontal scaffolds that may enable regeneration of multi-tissue interfaces required for oral, craniofacial, and periodontal engineering applications.

8.7. FIGURES

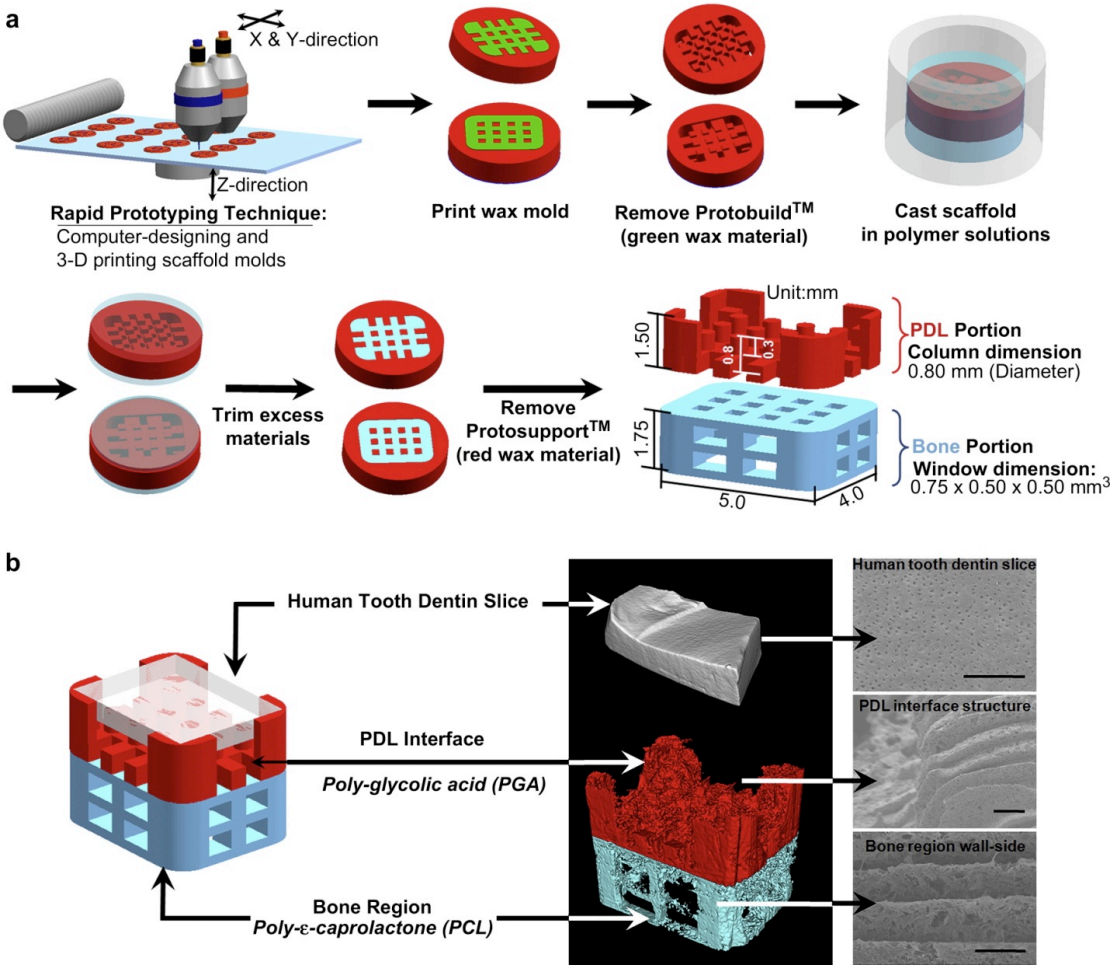

Figure 8.1. a) Schematic illustration of the 3-D wax printing system and dimension of hybrid scaffold shows polymeric architecture manufacturing. For the PDL interface, column-like structures were 0.8 mm diameter and 0.3 mm exposed heights and casted using PGA-HFIP solution. For the bone region of the hybrid scaffold, PCL-acetone solution was used for casting. PCL-acetone, pasted on the PCL-casted mold and PDL interface architectures were placed on it. b) After the acid-treatment of human tooth dentin slices, the complex with a polymer-casted hybrid scaffold and a dentin slice was assembled using fibrin gel with or without cells. The left is the 3-D designed hybrid

scaffold and the right panel is the micro-CT scanned and 3-D reconstructed hybrid scaffold and a dentin slice. The scale bar: 50 μm.

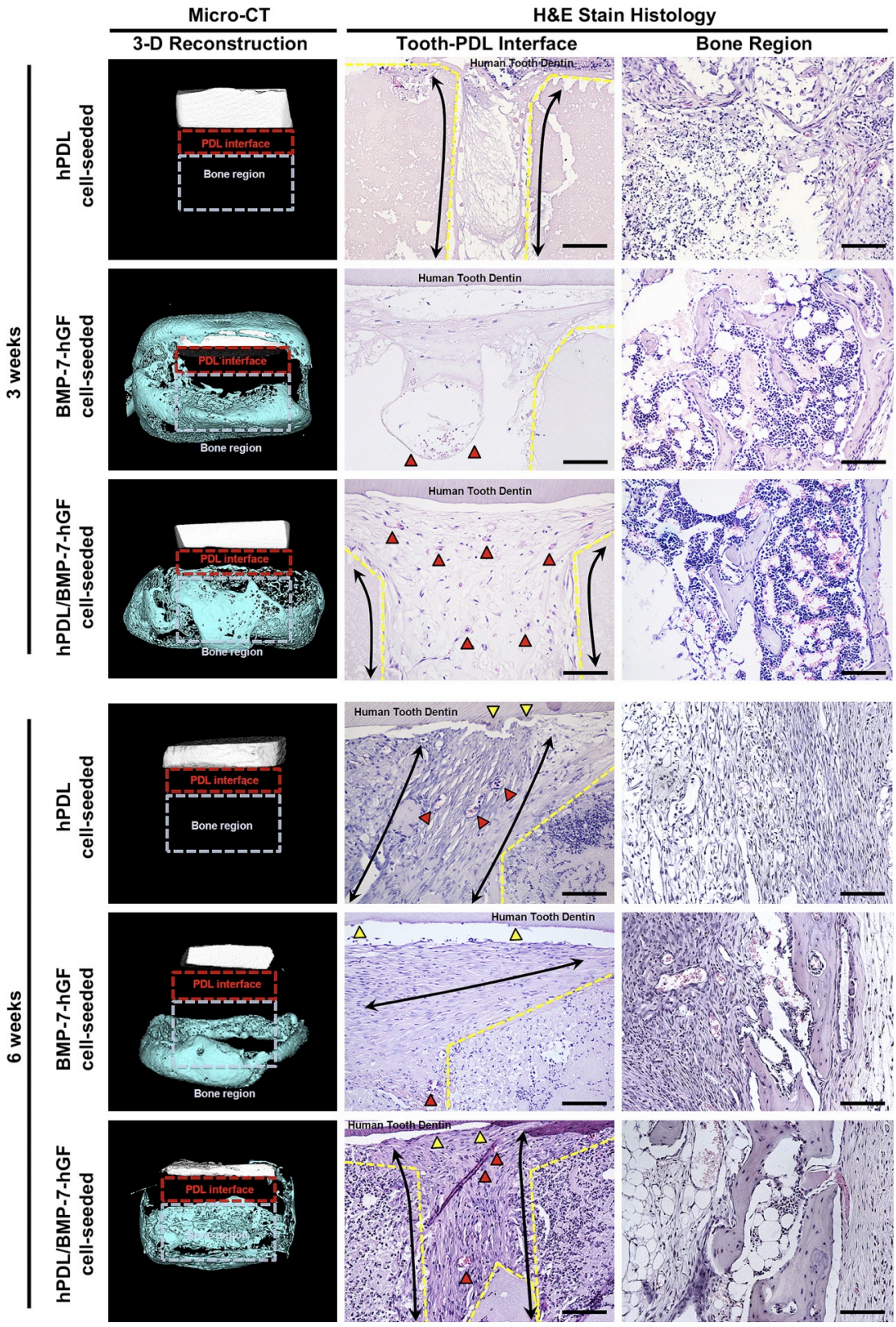
Micro-CT
H&E Stain Histology
3-D Reconstruction
Tooth-PDL Interface
Bone Region
3 weeks
6 weeks
hPDL cell-seeded
BMP-7-hGF cell-seeded
hPDL/BMP-7-hGF cell-seeded
PDL interface
Bone region
Human Tooth Dentin

Figure 8.2. 3-D reconstructed colorized micro-CT images and hematoxylin and eosin (H&E) stained histology. The mineralized tissue (blue-colorized) was formed around the hybrid scaffolds and there was no ankylosis, bone fusion to the dentin surface (white-colorized). Red and blue dashed lined-boxes represent the PDL interface and bone regions, respectively. H&E stained histology slices showed PDL interfaces and bone region tissues to evaluate fibrous tissue orientation along the column-like structures in PDL interface, which were designed with perpendicular direction to the dentin surface. At 6 weeks, hPDL cell seeded specimens demonstrated perpendicular orientation to the dentin slices and along the column-like structures with limited evidence of cementum-like cells on the dentin surface. Yellow dash-line is the borderline of channel-type PDL architecture and black arrowed lines represent the fibrous cell/tissue directionality following the wall of PDL interface structure. Red triangles indicate the blood vessels and yellow triangles point cementum-like tissue layer or cell deposition for cementogenesis on the dentin surface. The scale bar: 50 μm.

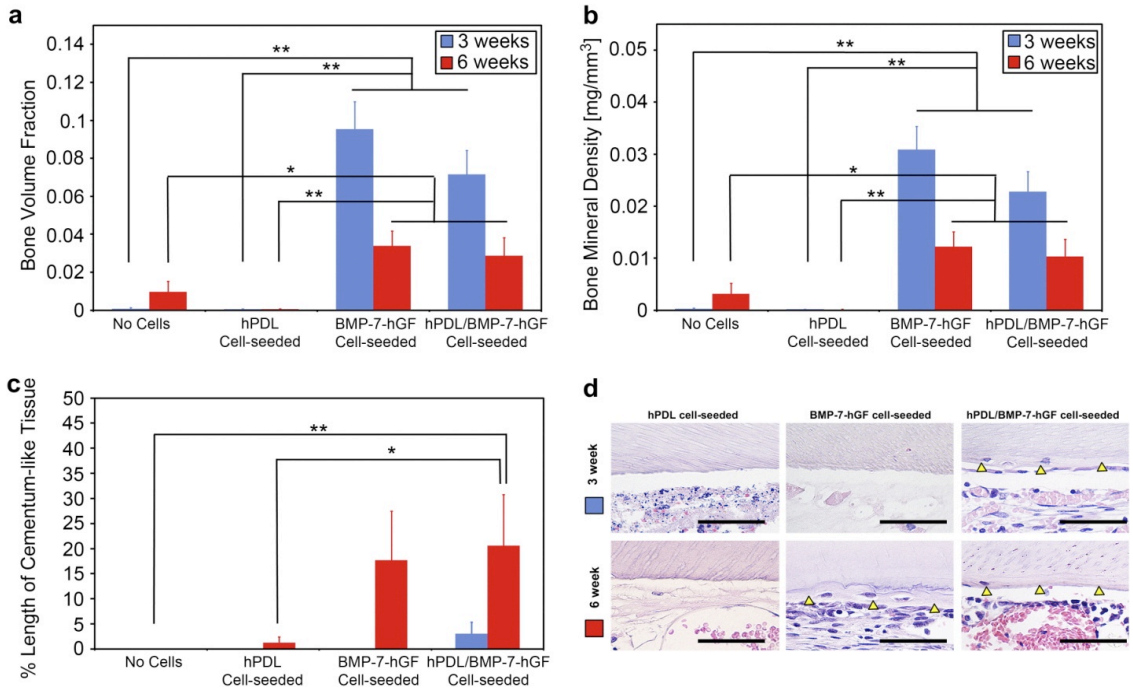

Figure 8.3. Quantitative analysis of micro-CT and histomorphometry for cementum-like tissue length. At 3 week time point, a) bone volume fraction (BVF) and b) bone mineral density (BMD) at 3 and 6 weeks were measured and analyzed statistically for bone regions of the hybrid scaffolds. a and b) In the aspects of BVF and BMD, there were statistically significant differences between the osteogenic factor and non-osteogenic factor groups in bone regions at 3 weeks (**$p < 0.01$) and 6 weeks (*$p < 0.05$ and **$p < 0.001$). c) The cementum-like tissue length percentage represented of mineralized layer deposition on the dentin surface at 3 and 6 weeks. Full surface length of dentin slice, which faced to the PDL interface was measured and divided the measured the cementum-like tissue length (%). At 6 weeks, hPDL/BMP-7-hGF cell seeded group had statistically significant differences with no cell and hPDL cell seeded groups (*$p = 0.02433$ and **$p = 0.00722$). d) Qualitative results using H&E staining for the cementum-like tissue formation on the dentin surface. In 3 weeks, there was limited

evidence of the mineralized layer formation but, in 6 weeks, significantly increased mineral deposition can be determined with the cementocyte-like cell embedded indicated by yellow triangles. For all statistical data analysis, two-tailed Kruskal–Wallis one-way ANOVA test and Mann–Whitney U-Test were utilized and data were mean ± standard error of mean (S.E.M.). Scale bar: 50 μm.

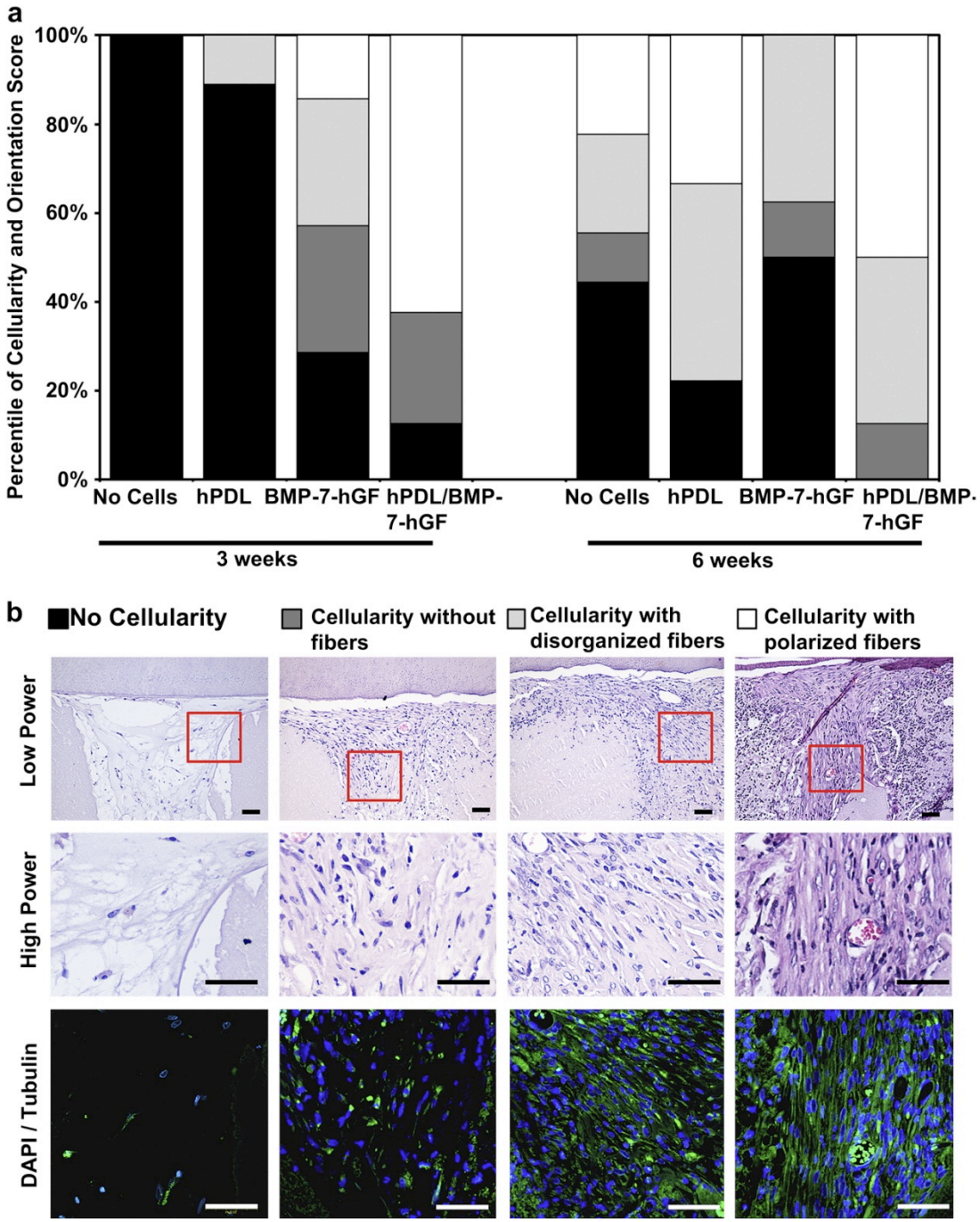

Figure 8.4. Cellularity and cell/tissue orientation in PDL interface using H&E staining and Immunofluorescence images. The fibrous tissue orientation was measured by semi-quantitative analysis with four different indexes; no cellularity, cellularity without fiber formation, cellularity with disorganized fiber, and cellularity with perpendicularly oriented fiber formation to the dentin surface. The H&E staining pictures

are the representatives for these four indices. The percent number of the semi-quantitative analysis was calculated with total number of samples in each group/time point and the number of each observation index. Immunofluorescent images represent four typical examples of indexes with DAPI (blue) and tubulin (green) staining in cytoplasm. Scale bar: 50 μm.

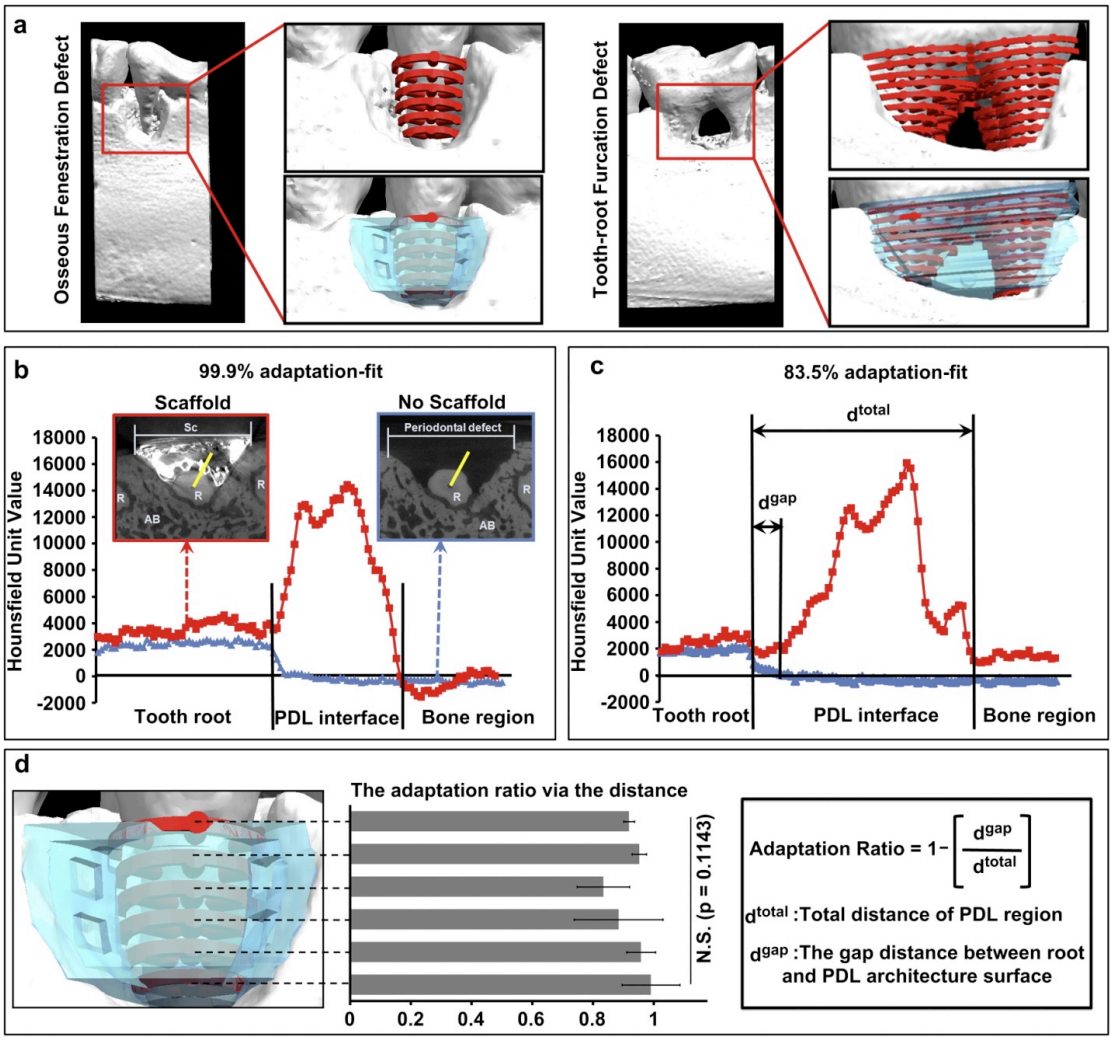

Figure 8.5. The reverse-engineered periodontal defect-fit scaffold modeling and the adaptation of customized designed scaffold on the root surface. a) The computer-aided design (CAD)-based software, NX5 was utilized to create PDL (red-colorized) and bone (blue-colorized) interfaces of the hybrid scaffold. The anatomical defect-fit scaffold had the perpendicular oriented PDL internal channel-structures and topological similarities of the periodontal defects. The Furcation defect design had separated two different parts with key (buccal)–lock (lingual) system to make easier assembling and implanting through the buccal-lingual penetration defect region. b–c) The red line was porcine mandible image with the customized scaffold and the blue line was the exposed periodontal defect site. b) The histogram represented the 99.9% adaptable scaffold to the root surface. The measured length was 3.00 mm and scaffold was coated by 35% $BaSO_4$

solution. The yellow lines on the 2-dimensionally digitized slices represented the measured regions with 3.00 mm length from the dentin (dental pulp side) to the middle of defect site. The abbreviations were that AB: alveolar bone, R: tooth root, and Sc: hybrid scaffold. c) The histogram was from 83.5% adaptable scaffold image. The concaved region of the red line can represent the gap distance (d^{gap}) between tooth root surface and PDL interface scaffold. d) Based on the method in Figure 5.5-C and d, total PDL interface length (d^{total}) and d^{gap} were linearly measured and the adaptation ratio was calculated in each layer, which had 3 different channel-type structures. There was no statistically significant difference (N.S.) among 6 different layers ($p = 0.1143$) and the rage of adaptation was 83.3%<mean value of adaptation ratio < 99.0% and data were mean ± standard deviation (S.D.). For the statistical analysis, the nonparametric Kruskal–Wallis one-way ANOVA test was used.

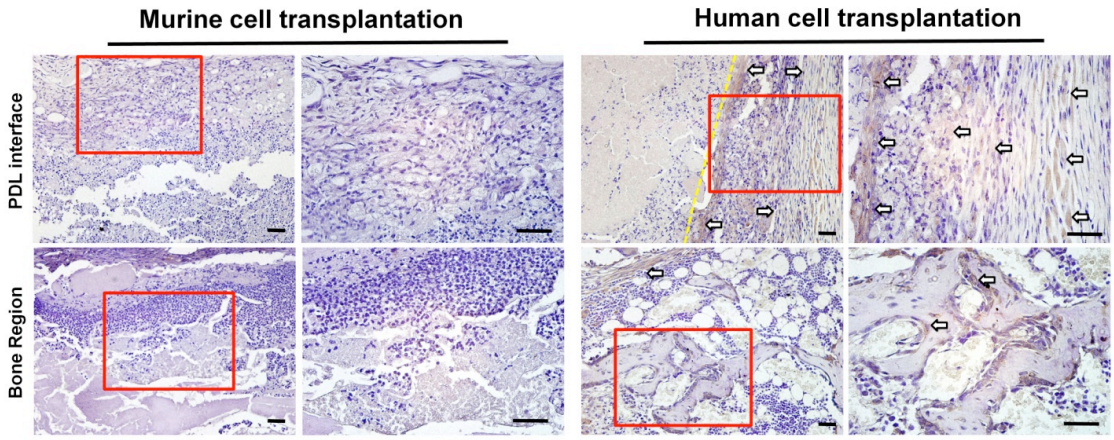

Figure 8.6. Immunohistochemical staining to probe transplanted human cells. Using human leukocyte antigen (HLA-A) molecules and the Avidin-Biotin Complex (ABC) staining kit, the difference of cell-types was determined and characterized between transplanted human cells (hPDL and BMP-7-hGF cells) and host NIH-III nude mouse cells. The panel, titled no human cell transplanted demonstrated hematoxylin staining of cell nucleus enabled to host cell infiltration into the hybrid scaffold as a negative control. However, the panel, titled human cell transplanted (hPDL and BMP-7-hGF cell transplantation) showed the white arrow-indicated, brow-colored regions were represented as staining of human cell membrane with ABC kit. The yellow dash line represented scaffold-tissue interface. Scale bar: 50μm.

8.8. TABLE

Compartment of Hybrid Scaffold	Volumetric Parameters	*p*-value (3 weeks)	*p*-value (6 weeks)
PDL Interface	Bone Volume Fraction	0.9381	0.5123
	Bone Mineral Density	0.8248	0.4234
Bone Region	Bone Volume Fraction	< 0.001	< 0.001
	Bone Mineral Density	< 0.001	< 0.001

Table 8.1. Statistical analysis for mineralized tissue formations in PDL interface and bone region of the hybrid scaffold. In PDL interface, the result of the analysis indicated that overall examination demonstrated that it was not significantly different using the two-tailed Kruskal-Wallis one-way ANOVA method ($p>0.05$)[1]. The significant differences ($p<0.001$) show in bone volume fraction and bone mineral density. Because these overall examinations were significant using Kruskal-Wallis test, the pair-wise comparisons, Mann-Whitney U-test[1] among four different groups per time point should be completed (see Fig. 3-a,b).

8.9. REFERENCES

1. B.L. Pihlstrom, B.S. Michalowicz and N.W. Johnson, Periodontal diseases, *Lancet* **366** (9499) (2005), pp. 1809–1820.

2. S.S. Socransky, A.D. Haffajee, M.A. Cugini, C. Smith and R.L. Kent Jr., Microbial complexes in subgingival plaque, *J Clin Periodontol* **25** (2) (1998), pp. 134–144.

3. M. Tobita and H. Mizuno, Periodontal disease and periodontal tissue regeneration, *Curr Stem Cell Res Ther* (2009) Epub ahead of print [PMID: 19941449].

4. T. Popowics, K. Yeh, K. Rafferty and S. Herring, Functional cues in the development of osseous tooth support in the pig, Sus scrofa, *J Biomech* **42** (12) (2009), pp. 1961–1966.

5. E. Reichenberger, S. Baur, C. Sukotjo, B.R. Olsen, N.Y. Karimbux and I. Nishimura, Collagen XII mutation disrupts matrix structure of periodontal ligament and skin, *J Dent Res* **79** (12) (2000), pp. 1962–1968.

6. K.L. Moffat, W.H. Sun, P.E. Pena, N.O. Chahine, S.B. Doty and G.A. Ateshian *et al.*, Characterization of the structure-function relationship at the ligament-to-bone interface, *Proc Natl Acad Sci U S A* **105** (23) (2008), pp. 7947–7952.

7. C.A. Ramseier, Z.R. Abramson, Q. Jin and W.V. Giannobile, Gene therapeutics for periodontal regenerative medicine, *Dent Clin North Am* **50** (2) (2006), pp. 245–263 ix.

8. G.T. Huang, S. Gronthos and S. Shi, Mesenchymal stem cells derived from dental tissues vs. those from other sources: their biology and role in regenerative medicine, *J Dent Res* **88** (9) (2009), pp. 792–806.

9. M. Nakashima and A.H. Reddi, The application of bone morphogenetic proteins to dental tissue engineering, *Nat Biotechnol* **21** (9) (2003), pp. 1025–1032.

10. R. Langer and J.P. Vacanti, Tissue engineering, *Science* **260** (5110) (1993), pp. 920–926.

11. J.P. Vacanti and R. Langer, Tissue engineering: the design and fabrication of living replacement devices for surgical reconstruction and transplantation, *Lancet* **354** (Suppl. 1) (1999), pp. SI32–SI34.

12. R.E. Guldberg, Spatiotemporal delivery strategies for promoting musculoskeletal tissue regeneration, *J Bone Miner Res* **24** (9) (2009), pp. 1507–1511.

13. J.P. Spalazzi, E. Dagher, S.B. Doty, X.E. Guo, S.A. Rodeo and H.H. Lu, In vivo evaluation of a multiphased scaffold designed for orthopaedic interface tissue engineering and soft tissue-to-bone integration, *J Biomed Mater Res A* **86** (1) (2008), pp. 1–12.

14. L. Hong and J.J. Mao, Tissue-engineered rabbit cranial suture from autologous fibroblasts and BMP2, *J Dent Res* **83** (10) (2004), pp. 751–756.

15. R.J. Petrie, A.D. Doyle and K.M. Yamada, Random versus directionally persistent cell migration, *Nat Rev Mol Cell Biol* **10** (8) (2009), pp. 538–549.

16. A.D. Doyle, F.W. Wang, K. Matsumoto and K.M. Yamada, One-dimensional topography underlies three-dimensional fibrillar cell migration, *J Cell Biol* **184** (4) (2009), pp. 481–490.

17. J.M. Taboas, R.D. Maddox, P.H. Krebsbach and S.J. Hollister, Indirect solid free form fabrication of local and global porous, biomimetic and composite 3D polymer-ceramic scaffolds, *Biomaterials* **24** (1) (2003), pp. 181–194.

18. D.E. Discher, D.J. Mooney and P.W. Zandstra, Growth factors, matrices, and forces combine and control stem cells, *Science* **324** (5935) (2009), pp. 1673–1677.

19. K.M. Yamada and E. Cukierman, Modeling tissue morphogenesis and cancer in 3D, *Cell* **130** (4) (2007), pp. 601–610.

20. D.E. Discher, P. Janmey and Y.L. Wang, Tissue cells feel and respond to the stiffness of their substrate, *Science* **310** (5751) (2005), pp. 1139–1143.

21. R.J. Pelham Jr. and Y. Wang, Cell locomotion and focal adhesions are regulated by substrate flexibility, *Proc Natl Acad Sci U S A* **94** (25) (1997), pp. 13661–13665.

22. E.S. Place, N.D. Evans and M.M. Stevens, Complexity in biomaterials for tissue engineering, *Nat Mater* **8** (6) (2009), pp. 457–470.

23. S. Mitragotri and J. Lahann, Physical approaches to biomaterial design, *Nat Mater* **8** (1) (2009), pp. 15–23.

24. S.J. Hollister, Porous scaffold design for tissue engineering, *Nat Mater* **4** (7) (2005), pp. 518–524.

25. S.J. Hollister, Scaffold design and manufacturing: from concept to clinic, *Adv Mater* **21** (32) (2009), pp. 3330–3342.

26. J.A. Meganck, K.M. Kozloff, M.M. Thornton, S.M. Broski and S.A. Goldstein, Beam hardening artifacts in micro-computed tomography scanning can be reduced by X-ray beam filtration and the resulting images can be used to accurately measure BMD, *Bone* **45** (6) (2009), pp. 1104–1116.

27. H. Miyaji, T. Sugaya, K. Kato, N. Kawamura, H. Tsuji and M. Kawanami, Dentin resorption and cementum-like tissue formation by bone morphogenetic protein application, *J Periodontal Res* **41** (4) (2006), pp. 311–315.

28. F.M. Chen, R.M. Shelton, Y. Jin and I.L. Chapple, Localized delivery of growth factors for periodontal tissue regeneration: role, strategies, and perspectives, *Med Res Rev* **29** (3) (2009), pp. 472–513.

29. A. Nanci and D.D. Bosshardt, Structure of periodontal tissues in health and disease, *Periodontol* **2000** (40) (2006), pp. 11–28.

CHAPTER NINE

SUMMARY AND DISCUSSION

There are four main themes, which have been demonstrated in this dissertation: 1) development of the micro-computed tomography (micro-CT) methodology to assess the alveolar bone structure to quantify the periodontal disease, regeneration, and orthodontic tooth movement; 2) development of methodology for applications in pre-clinical and clinical studies; 3) computer-aided design (CAD)-based hybrid scaffold evaluation to induce ectopic periodontal tissue regeneration.

In **Chapter Two**, we developed a novel and accurate methodology to analyze alveolar bone volumetric parameters for the quantitative assessment of periodontal hard tissue regeneration. This methodology allows highly accurate and precise quantification assessment of alveolar bone regeneration rather than using conventional two-dimensional dental x-ray radiographic techniques. For validation of this methodology, we have found that following training of evaluators, a typical agreement of approximately 1% between examiners can be achieved. Of the statistical analysis methods, Coefficient of Variation (CV) demonstrated precise error for reproducibility of developed volumetric

measurements. CV was less than 1.5% in inter- and intra-examiner calibrations demonstrating that this methodology has very high reproducibility and reliability of measurement. Moreover, micro-CT scanning showed to be highly reproducible and repeatable with very low precision errors. Bone volume fraction (BVF) and bone mineral density (BMD) had 0.84% and 2.1% precision errors, respectively. Bone loss by experimentally induced disease was found to be significantly different between healthy and diseased groups.

In **Chapter Three**, we have addressed different pre-clinical applications for periodontal disease quantification and orthodontic tooth movement. AAV2/1-TNFR:Fc gene delivery method can play a role in the blockade of TNF-α inflammation in animal models and inhibit osteoclastogenesis-related bone resorption. A periodontal disease induction model in rats was designed and evaluated with systemic AAV2/1TNFR:Fc administration. The experimental design was follows: 1) control (vehicle), 2) AAV-TNFR:Fc, 3) AAV-TNFR:Fc + *Pg*-LPS, and 4) *Pg*-LPS only. For micro-CT analysis, the ROI was selected from the roof of furcation (ROF) to root apex (RA) of the 1st molar (on the sagittal view) with measurements made around the 1st molar, from the mesial 1st molar to the mesial 2nd molar within the interproximal area (on the coronal view). The qualitative and quantitative data from this study resulted in a significant prevention of periodontal disease with (Fig. 3.2).

In **Chapter Four**, osteoprotegerin (OPG) is an inhibitor of osteoclastogenesis and bone resorption. The periodontitis induction model was designed with the 3/0 cotton ligatures

around the first molar tooth. Human recombinant OPG fusion protein (rhOPG-Fc) was delivered to the region of tooth ligatures at 3 and 6 week time-points. Using the same ROI criteria as the AAV2/1-TNFR:Fc study, the periodontal alveolar bone structure was quantified by micro-CT. Linear bone loss analysis showed OPG +disease induction yielded no significant difference between the no treatment animals and OPG injection only animals at 3 and 6 weeks. Results from volumetric measurements (parameters: BVF and BMD) showed no significant difference between the no treatment healthy group and the OPG+periodontitis induction group at both time-points.

In **Chapter Five**, a Sprague-Dawley rat tooth movement model was designed and established by placing nickel-titanium springs between incisors and the 1st molar. The spring provided forces and induced the 1st molar movement toward the incisor within rat mandibulae. In this experiment, external forces from spring placement induced tooth movement and the movement had been a cause of alveolar bone deformation. The experimental groups were as follows: 1) control, or baseline, 2) vehicle with spring placement, 3) low dose OPG injection (0.5 mg/kg), and 4) high dose OPG injection (5.0 mg/kg) in order to analyze OPG efficacy. Biomechanical tooth movement was dependent on osteoclastogenesis. The high dose OPG injection group showed less bone resorption (via bone volume fraction) and the 1st molar-movement distance was different for each group depending on degree of bone resorption. The degree of tooth movement due to bone resorption (or lack of) was more accurately prognosed with micro-CT imaging technique and three-dimensional volumetric measurements. The results demonstrated an

inhibition of osteoclastogenesis with high dose OPG injection, significantly blocking tooth movement.

In **Chapter Six**, we have demonstrated the clinical applications for evaluating alveolar bone healing and mineralized tissue formation within tooth-extraction sockets. Collagen membrane, which covered the tooth-extraction socket, was evaluated for prevention of soft fibrous tissue invasion into the socket site and for accelerated induction of natural bone healing. Following membrane treatments of 10 patients at 12 weeks, re-entry surgery was performed and bone core biopsies were collected to analyze bone quality for dental prosthetic implantation. Based on the resultant micro-CT analysis, there was statistical significance and down-growth of epithelium was prevented into the dental socket-site, without any mineralization on the collagen membrane barrier surface.

In **Chapter Seven**, bone repair cells (BRCs; produced from bone marrow aspirates) were harvested and cultured in an automated, closed system, single-pass perfusion (SPP) process. After cultivation for 12 days in the SPP system, BRCs were surgically transplanted with a gelatin sponge into the dental extraction socket. Surgical re-entry was performed after 6 weeks and bone core biopsies were harvested and histomorphometric analysis was utilized for evaluation of BRC angiogenic and osteogenic differentiation. Micro-CT was analyzed qualitatively with 3-D reconstruction to observe the bone growth patterns. Highly mineralized tissue formation was visualized and angiogenic blood vessel formation was observed following analysis of hematoxyline and eosin (H&E) staining.

In **Chapter Eight**, the computer design-based hybrid scaffolding system was evaluated for ectopic periodontal tissue regeneration. An acid-treated human tooth dentin slice was placed on the PDL interface of the designed hybrid scaffold and seeded as follows with different cell types to induce multiple tissue formation: 1) no cells control; 2) human PDL cells seeded within the PDF interface only; 3) BMP-7 transduced human gingival fibroblast cells (BMP-7-hGF) seeded within the bone region only; 4) human PDL cells within the PDL interface and BMP-7-hGF transplanted within the bone region of the hybrid scaffold. Results were evaluated using histomorphometric analysis, micro-CT quantification and qualification, and immunohistochemistry. In the results, the computer-designed, multi-layered hybrid scaffolding system successfully compartmentalized to regenerate different tissues and the periodontal ligament tissue orientation was in a perpendicular direction to the dentin surface. Furthermore, the CT, image-based scaffold system had high adaptability to the periodontal defect topology. Therefore, the CT image-based, customized defect-fit scaffold has significant clinical relevance.

Collectively, the micro-CT methodology has been shown to quantify alveolar bone structure during periodontal disease progression. This novel methodological approach using micro-CT image analysis can accurately and reproducibly measure tooth-supporting alveolar bone loss or regeneration. The methodology has demonstrated strong agreement between examiners with significant reliability and reproducibility. Therefore, these methods can serve as a standard for assessing both periodontal disease progression and bone regeneration. The use of micro-CT and its associated software can provide effective 3-D visualization and image analysis of the bone-tooth interface to compliment

craniofacial and orthopedic studies. The complicated topology can provide optimal, nondestructive natural landmarks to create regions of interest for volumetric assessments. In addition to reproducibility and reliability, this methodology has wide applications within dental science and tissue engineering, showing more feasibility for indirect analysis and prediction of orthodontic tooth movement as well as predicting periodontal disease progression and periodontal tissue regeneration.

The tissue-guidable scaffolding architectures were designed and manufactured by the rapid prototyping technique. Biomimetic hybrid scaffold was comprised of PDL interface with vertically oriented architectures for perpendicular orientation of fibrous tissue and bone region with high porosity. This multi-layered complex with untreated human PDL cells and BMP-7 transduced human gingival fibroblast-like cells was transplanted subcutaneously in the ectopic model system. In spite of conditions with no biomechanical loading, the physical and topographical design approach provided periodontal tissue organization. The newly formed PDL cells/tissues were correctly guided along the designed, perpendicularly-oriented architecture to the human tooth dentin slice. The mineralized tissues were not formed into the PDL interface of the hybrid scaffold thus the hybrid scaffolding system can demonstrate multiple tissue regeneration can be compartmentalized in each region of the hybrid scaffold at 3 and 6 weeks.

CHAPTER TEN

FUTURE DIRECTIONS

As this dissertation has demonstrated, a novel computer-designed scaffolding system has achieved multiple periodontal tissue regeneration. In this study we found that we could use CAD-based, periodontal-inspired hybrid scaffolds to realize multi-periodontal tissue regeneration and early-stage periodontal integration in a single system. Based upon the results in this dissertation we will attempt to perform a clinically-relevant study using computer-/medical image-based scaffold design and manufacturing methodology with micro-architecture geometry within a large animal model. Using the periodontitis-induction model system, unpredictable topological destruction and regeneration will be evaluated with the medical image-based scaffolding approach instead of surgically created periodontal defects.

Within the aspects of periodontal stem cell bioengineering approaches, the micro-scale hybrid scaffolding system showed somewhat unpredictable anchorage of PDL connective tissue with premature mineralized tissue. A robust anchorage of fibrous connective tissue to mineralized tissue surface is crucial for tissue re-functionalization. PDL stem cells can potentially differentiate to cementum and bone to induce this periodontal connective

tissue anchorage. Unfortunately, the differentiation mechanism of PDL stem cells is not well understood and thus its use is difficult to optimize for formation of osteogenic tissue layers to support anchorage. Although a tissue-guidable scaffolding system can help to regenerate and organize multiple periodontal tissues, micron-scale interface integration remains a critical need for functional restoration of newly formed tissue. Therefore, the surface-topography scaffold design approach is necessary to help understand the PDL stem cell role in stimulating osteogenic differentiation of human PDL stem cells. This study will provide a more optimized design concept for periodontal tissue integration and periodontal tissue functional restoration following the proliferation, differentiation, and mechano-transductive responses of periodontal ligament stem cells.

Physico-mechanical properties of the scaffolding system will also contribute to cell/tissue infiltration into the extracellular matrices and mechano-transduction of periodontal ligament stem cells. Periodontal *in-vivo* environments, where various mechanical stimulations are generated, may have more complicated stem cell response mechanisms. Although many investigators have achieved and demonstrated the control of bone marrow stem cell differentiation with different stiffness and elasticity of substrate, physico-mechanical properties may contribute to different periodontal ligament stem cell behaviors *in-vivo,* unlike simplified homogeneous geometric approaches or *in-vitro* conditions. So different concentrations of extracellular matrix materials can provide further controllable tissue regeneration with the cellular differentiations.